

A NORMALIZED SET OF FORCE AND PERMEANCE DATA FOR DOUBLY-  
SALIENT MAGNETIC GEOMETRIES

A THESIS SUBMITTED TO  
THE GRADUATE SCHOOL OF NATURAL AND APPLIED SCIENCES  
OF  
MIDDLE EAST TECHNICAL UNIVERSITY

BY

IBRAHIM MAHARIQ

IN PARTIAL FULFILLMENT OF THE REQUIREMENTS  
FOR  
THE DEGREE OF MASTER OF SCIENCE  
IN  
ELECTRICAL AND ELECTRONICS ENGINEERING

APRIL 2009

Approval of the thesis:

**A NORMALIZED SET OF FORCE AND PERMEANCE DATA FOR DOUBLY-SALIENT  
MAGNETIC GEOMETRIES**

submitted by **IBRAHIM MAHARIQ** in partial fulfillment of the requirements for the degree of  
**Master of Science in Electrical and Electronics Engineering Department, Middle East Technical  
University** by,

Prof. Dr. Canan Özgen

Dean, Graduate School of **Natural and Applied Sciences**

\_\_\_\_\_

Prof. Dr. İsmet Erkmen

Head of the Department, **Electrical and Electronics Engineering**

\_\_\_\_\_

Prof. Dr. H. Bülent Ertan

Supervisor, **Electrical and Electronics Engineering Dept., METU**

\_\_\_\_\_

**Examining Committee Members:**

Prof. Dr. M. Kemal Leblebicioğlu

Electrical and Electronics Engineering Dept., METU

\_\_\_\_\_

Prof. Dr. H. Bülent Ertan

Supervisor, Electrical and Electronics Engineering Dept., METU

\_\_\_\_\_

Prof. Dr. Muammer Ermiş

Electrical and Electronics Engineering Dept., METU

\_\_\_\_\_

Prof. Dr. Timur Aydemir

Electrical and Electronics Engineering Dept., Gazi University

\_\_\_\_\_

Assoc. Prof. Dr. Erbil Nağacı

Electrical and Electronics Engineering Dept., METU

\_\_\_\_\_

Date: 30 April 2009

**I hereby declare that all information in this document has been obtained and presented in accordance with academic rules and ethical conduct. I also declare that, as required by these rules and conduct, I have fully cited and referenced all material and results that are not original to this work.**

Name, Last Name: Ibrahim MAHARIQ

Signature :

# ABSTRACT

## A NORMALIZED SET OF FORCE AND PERMEANCE DATA FOR DOUBLY-SALIENT MAGNETIC GEOMETRIES

MAHARIQ, Ibrahim

M.Sc., Department of Electrical and Electronics Engineering

Supervisor: Prof. Dr. H. Bülent Ertan

April 2009, 171 pages

In this study, a model is developed to represent doubly-salient magnetic circuits and to fit finite element analysis for the aim of obtaining a set of normalized normal force, tangential force, and permeance variation data. To obtain the desired data FE field solution method is used. The reliability of finite element results have been verified by three steps; first, comparing the numerical results with analytically calculated permeance, second, by solving two switch reluctance motors and comparing the results with the measurements of static torque and flux linkage. The third step is by using the normalized data obtained by solving the model with the aid of an available software that is capable to predict the behavior of switched reluctance motors. Once the reliability of the data is assured, the desired data set is produced and presented in tables.

**Keywords:** Finite Element Analysis, Switched Reluctance Motor, doubly-Salient Magnetic Circuits, Normalized Data.

# ÖZ

## ÇİFT TARAFLI ÇIKIK KUTUPLU YAPILAR İÇİN NORMALİZE EDİLMİŞ MOMENT VE PERMEANS VERİ TABANI

MAHARIQ, Ibrahim

Yüksek Lisans, Elektrik ve Elektronik Mühendisliği Bölümü

Tez Yöneticisi: Prof. Dr. H. Bülent Ertan

Nisan 2009, 171 sayfa

Bu çalışmada, çift çıkıklı manyetik devreleri temsil etmesi için normalize edilmiş dik kuvvet, teğet kuvvet ve manyetik iletkenlik değişimi verisi elde etmek üzere sonlu eleman analizleri uyumlu bir model geliştirilmiştir. Gerekli veriyi elde etmek için Sonlu Eleman alan çözüm metodu kullanılmıştır. Sonlu eleman sonuçlarının güvenilirliği üç adımda doğrulanmıştır; ilk adımda sayısal sonuçlar ile analitik olarak hesaplanan manyetik iletkenlik karşılaştırılmış, ikinci adımda iki tane anahtarlamalı relüktans motoru çözülmüş ve statik moment ve akı çözümleri ölçüm sonuçları ile karşılaştırılmıştır. Üçüncü adımda modelin çözümü ile elde edilen normalize edilmiş veri, anahtarlamalı relüktans motorların davranışlarını kestirebilecek bir bilgisayar programda kullanılmıştır. Verilerin güvenilirliği sağlandığında, veri kümeleri üretilmiş ve tablolarda gösterilmiştir.

**Anahtar kelimeler:** Sonlu Eleman Analizi, Anahtarlamalı Relüktans Motoru, Çift-çıkıklı Manyetik Devreler, Normalize Edilmiş Veri

To My Family

To Azhar Almahariq

## **ACKNOWLEDGEMENTS**

The author wishes to express his sincere appreciation to Prof. Dr. H. Bülent Ertan for, not only his precious time spent for advice, encouragements and insight throughout the research, but also for the financial support through enrolling the author to learn Finite Element Analysis. The author also thanks the teachers from whom he learned a lot not only in the academic field, but also from the distinctive ways of teaching that they have. Finally, the author appreciates the good behavior of Turkish people towards him, the people who will stay in the mind of the author forever.

# TABLE OF CONTENTS

<b>ABSTRACT</b> .....	<b>IV</b>
<b>ÖZ</b> .....	<b>V</b>
<b>ACKNOWLEDGEMENTS</b> .....	<b>VII</b>
<b>TABLE OF CONTENTS</b> .....	<b>VIII</b>
<b>LIST OF TABLES</b> .....	<b>XI</b>
<b>LIST OF FIGURES</b> .....	<b>XIII</b>
<b>CHAPTER</b>	
<b>INTRODUCTION</b> .....	<b>1</b>
1.1 General.....	1
1.2 Importance of Flux Linkage Characteristics .....	3
1.2.1 Analytical Estimation of Flux-Linkage-Current Curve .....	3
1.2.2 Field Solution for Obtaining Flux Linkage Curves .....	5
1.3 Ertan’s Model .....	6
1.4 Purpose of the Study .....	8
<b>FINITE ELEMENT ANALYSIS</b> .....	<b>10</b>
2.1 A Brief History .....	10
2.2 What is Finite Element Analysis? .....	10
2.3 Basic Principle .....	12
2.4 Maxwell’s Equations .....	13
2.5 Mesh Formation.....	16
2.6 Matrix Equations of Elements.....	21
2.7 Boundary Conditions .....	23
2.8 Methods of Solving System Equations .....	24
2.9 Iterative Method for Nonlinear Problems .....	27
2.10 Representation of Nonlinear BH curve for FEM Computation .....	31
2.11 Force Computations .....	33
2.12 Conclusion .....	35
<b>DEVELOPING A MODEL FOR PERMEANCE AND FORCE CALCULATION</b> .....	<b>36</b>
3.1 Outline.....	36
3.2 Introduction.....	36
3.3 Model of Normalized Data .....	38
3.4 Model Definition in Flux2D .....	39



3.4.1 Definition of Geometry in Flux2D8.1 .....	41
3.4.2 Meshing the Model .....	44
3.4.2.1 Description of the Automatic/Mapped Mesh Generator in FLUX.....	44
3.4.2.2 Meshing the Model in Flux2D .....	46
3.4.3 Definition of Materials .....	51
3.4.4 Creating the Physical Problem (Prophy in Flux2D) .....	53
3.4.4.1 Definitions of Regions .....	55
3.4.4.2 Boundary Condition .....	55
3.4.5 Solving the Problem (SOLVER_2D) .....	57
3.5 Model Investigation .....	58
3.5.1 Studying the Mesh.....	58
3.5.2 Solution Criteria .....	61
3.5.3 MMF Drop.....	62
3.5.4 Contour Plots of Potential.....	64
3.5.5 Using Another FEA-based Software (ANSYS): .....	67
3.6 Computations .....	69
3.6.1 Tooth Flux Density.....	69
3.6.2 Permeance Computations .....	74
3.6.3 Force Computations.....	75
3.6.4 Torque Calculations:.....	80
3.6.5 Flux Linkage Calculations:.....	82
3.7 Conclusion .....	87
<b>FEA VERIFICATION.....</b>	<b>88</b>
4.1 Outline.....	88
4.2 Comparison of Analytically Calculated Permeance with Numerical Computations: .....	88
4.3 Solutions of Test Motors.....	97
4.3.1 Test motor 2 (SR2) .....	97
4.3.1.1 Specification of SR2.....	97
4.3.1.2 Mesh of SR2 in ANSYS.....	101
4.3.1.3 Shifting the Rotor .....	105
4.3.1.4 Definition of Physical Problem .....	107
4.3.1.5 Solution Criteria in ANSYS:.....	109
4.3.1.6 Contour Plots.....	110
4.3.1.7 ANSYS Results Compared with Measurements of SR2.....	112

4.3.1.8 Flux2D Results compared ANSYS Results: .....	117
4.3.1.9 Flux linkage prediction including End leakage effect .....	121
4.3.2 SR1 Model.....	126
4.3.2.1 SR1 Geometry .....	126
4.3.2.2 Mesh of SR1 .....	128
4.3.2.3 Numerical Results of SR1: .....	130
4.4 Conclusion .....	137
<b>TABLE OF NORMALIZED DATA .....</b>	<b>138</b>
5.1 Introduction.....	138
5.2 Table of Normalized Data.....	139
5.3 Predictions Using Reference [21] for Test Motors .....	157
5.4 Comparison of Numerical Results and Analytical Predictions.....	166
<b>CONCLUSION .....</b>	<b>168</b>
<b>REFERENCES.....</b>	<b>170</b>

## LIST OF TABLES

TABLE 3. 1 B-H VALUES OF THE TEETH MATERIAL.....	52
TABLE 3. 2 MESH EFFECT ON TANGENTIAL FORCE.....	60
TABLE 3. 3 PRECISION (ACCURACY) EFFECT ON TANGENTIAL FORCE. ....	62
TABLE 3. 4 MMF DROP RESULTS.....	64
TABLE 3. 5 COMPARISON BETWEEN ANSYS 11.0 & FLUX2D.....	68
TABLE 4. 1 DATA POINTS CHOSEN FOR IN & OUT POSITIONS (G = 0.5MM).....	91
TABLE 4. 2 NORMALIZED PERMEANCE RESULTS (PN* FOR FLUX2D).....	96
TABLE 4. 3 DIMENSIONS OF SR2 .....	98
TABLE 4. 4 MESH INFORMATION .....	103
TABLE 4. 5 EXCITATION LEVELS .....	108
TABLE 4. 6 STATIC TORQUE NUMERICAL RESULTS OF SR2 (IN N.M).....	112
TABLE 4. 7 EXTRACTING STATIC TORQUE OF SR2 FROM MEASUREMENTS (IN N.M)...	113
TABLE 4.8 STATIC TORQUE MEASUREMENTS AND ANSYS RESULTS FOR SR2 AT 1A..	113
TABLE 4. 9 STATIC TORQUE MEASUREMENTS AND ANSYS RESULTS FOR SR2 AT 2A .	114
TABLE 4. 10 STATIC TORQUE MEASUREMENTS AND ANSYS RESULTS FOR SR2 AT 3A	114
TABLE 4. 11 MEASURED FLUX LINKAGE OF SR2 (IN WEB.TURN).....	114
TABLE 4. 12 FLUX LINKAGE MEASUREMENTS AND ANSYS RESULTS OF SR2 AT 1A....	115
TABLE 4. 13 FLUX LINKAGE MEASUREMENTS AND ANSYS RESULTS OF SR2 AT 2A....	115
TABLE 4. 14 FLUX LINKAGE MEASUREMENTS AND ANSYS RESULTS OF SR2 AT 3A....	115
TABLE 4. 15 ANSYS AND FLUX2D STATIC TORQUE RESULTS AT 1A.....	118
TABLE 4. 16 ANSYS AND FLUX2D STATIC TORQUE RESULTS AT 2A.....	118
TABLE 4. 17 ANSYS AND FLUX2D STATIC TORQUE RESULTS AT 3A.....	118
TABLE 4. 18 ANSYS AND FLUX2D FLUX LINKAGE RESULTS AT 1A.....	119
TABLE 4. 19 ANSYS AND FLUX2D FLUX LINKAGE RESULTS AT 2A.....	119
TABLE 4. 20 ANSYS AND FLUX2D FLUX LINKAGE RESULTS AT 3A.....	119
TABLE 4. 21 PREDICTION OF FLUX LINKAGE OF SR2 AT 1A INCLUDING ENDLEAKAGE CORRECTION.....	121
TABLE 4. 22 PREDICTION OF FLUX LINKAGE OF SR2 AT 2A INCLUDING ENDLEAKAGE CORRECTION.....	122
TABLE 4. 23 PREDICTION OF FLUX LINKAGE OF SR2 AT 3A INCLUDING ENDLEAKAGE CORRECTION.....	122
TABLE 4. 24 DIMENSIONS OF SR1[22].....	127
TABLE 4. 25 STATIC TORQUE MEASUREMENTS AND ANSYS RESULTS FOR SR1 AT 2A	131
TABLE 4. 26 STATIC TORQUE MEASUREMENTS AND ANSYS RESULTS FOR SR1 AT 3A	131

TABLE 4. 27 STATIC TORQUE MEASUREMENTS AND ANSYS RESULTS FOR SR1 AT 4A131

TABLE 4. 28 FLUX LINKAGE MEASUREMENTS AND ANSYS RESULTS OF SR1 AT 2A.... 133

TABLE 4. 29 FLUX LINKAGE MEASUREMENTS AND ANSYS RESULTS OF SR1 AT 3A.... 133

TABLE 4. 30 FLUX LINKAGE MEASUREMENTS AND ANSYS RESULTS OF SR1 AT 4A.... 133

TABLE 4. 31 PREDICTION OF FLUX LINKAGE OF SR1 INCLUDING ENDLEAKAGE  
CORRECTION..... 135

TABLE 5. 1 NORMALIZED DATA..... 140

TABLE 5. 2 MEASURED AND PREDICTED FLUX LINKAGE FOR SR2 WITH END-LEAKAGE  
CORRECTION (IN WB.T)..... 159

TABLE 5. 3 MEASURED AND PREDICTED STATIC TORQUE OF SR2 (IN N.M) ..... 160

TABLE 5. 4 MEASURED AND PREDICTED FLUX LINKAGE FOR SR1 WITH END-LEAKAGE  
CORRECTION (IN WB.T)..... 161

TABLE 5. 5 MEASURED AND PREDICTED STATIC TORQUE OF SR1 (IN N.M) ..... 162

TABLE 5. 6 PREDICTED-MEASURED TORQUES (N.M) AND PERCENTAGE ERRORS WITH  
END-LEAKAGE CORRECTION FOR SR2..... 165

TABLE 5. 7 COMPARISON OF FLUX LINKAGE FOR SR2 WITH END-LEAKAGE  
CORRECTION (IN WB.T)..... 166

TABLE 5. 8 COMPARISON OF FLUX LINKAGE FOR SR1 WITH END-LEAKAGE  
CORRECTION (IN WB.T)..... 167

## LIST OF FIGURES

FIGURE 1. 1 CROSS-SECTION OF A FOUR-PHASE SRM.....	2
FIGURE 1. 2 TYPICAL FLUX LINKAGE VS. POSITION CURVE OF AN SRM.....	5
FIGURE 1. 3 ERTAN'S MODEL .....	7
FIGURE 2. 1 ELECTROMAGNETIC FIELD DOMAIN .....	15
FIGURE 2. 2 SOME BASIC ELEMENTS USED FOR MESH FORMATION IN A FE STUDY, [15] .....	18
FIGURE 2. 3 THE MAGNETIC VECTOR POTENTIAL AT THE NODE OF A TYPICAL TRIANGULAR ELEMENT .....	19
FIGURE 2. 4 BH MODELS TO REPRESENT NONLINEAR CHARACTERISTIC.....	32
FIGURE 3. 1 ERTAN'S MODEL .....	37
FIGURE 3. 2 MODEL GEOMETRY FOR $X_N = 0.4$ , $T/\Lambda = 0.4$ .....	39
FIGURE 3. 3 LAYOUT OF FLUX2D SUPERVISOR .....	40
FIGURE 3. 4 TREE OF COMMANDS OF PREFLUX2D .....	41
FIGURE 3. 5 ADDING "ROTOR COORDINATES" MENU .....	42
FIGURE 3. 6 ADDING "NEW POINT" MENU.....	43
FIGURE 3. 7 ADDING "NEW LINE" MENU .....	43
FIGURE 3. 8 MAPPED MESH EXAMPLE .....	45
FIGURE 3. 9 ELEMENTS DISTRIBUTION IN THE MIDDLE TOOTH AND IN THE AIRGAP REGION( $\Lambda/G = 40$ , $T/\Lambda = 0.3$ , $X_N = 0$ ).....	48
FIGURE 3. 10 ELEMENTS DISTRIBUTION IN THE MIDDLE TOOTH AND IN THE AIRGAP REGION( $\Lambda/G = 40$ , $T/\Lambda = 0.3$ , $X_N = 0.2$ ).....	49
FIGURE 3. 11 ELEMENTS DISTRIBUTION IN THE STUDY DOMAIN( $\Lambda/G = 200$ , $T/\Lambda = 0.4$ , $X_N$ $= 0$ ) .....	50
FIGURE 3. 12 B-H CURVE OF TEETH MATERIAL.....	53
FIGURE 3. 13 GENERAL DIAGRAM OF CREATING A PHYSICAL PROBLEM IN PROPHY ...	54
FIGURE 3. 14 SECTION STUDIED IN PLANE AND AXISYMMETRIC PROBLEMS .....	54
FIGURE 3. 15 APPLICATION OF DIRICHLET CONDITION .....	56
FIGURE 3. 16 SOLVER CONFIGURATION .....	57
FIGURE 3. 17 TOOL BAR OF SOLVER_2D .....	58
FIGURE 3. 18 TANGENTIAL FORCE VS. NUMBER OF NODES IN TEETH AND AIRGAP.....	60
FIGURE 3. 19 TANGENTIAL FORCE VS. PRECISION (ACCURACY).....	62
FIGURE 3. 20 PLACES OF DRAWN PATH FOR $\Lambda/G = 70$ , $T/\Lambda = 0.3$ , $X_N = 0.0$ .....	63
FIGURE 3. 21 CONTOUR PLOT FOR $\Lambda/G = 70$ , $T/\Lambda = 0.3$ , $X_N = 0.2$ AND $MMF = 707$ A.T.....	66
FIGURE 3. 22 CONTOUR PLOT IN TEETH REGION FOR $\Lambda/G = 70$ , $T/\Lambda = 0.3$ , $X_N = 0.2$ AND $MMF = 220$ A.T .....	67

FIGURE 3. 23 TOOTH PITCH DEFINITION .....	69
FIGURE 3. 24 MAGNITUDE OF FLUX DENSITY FOR ( $\Lambda/G = 70$ , $T/\Lambda = 0.5$ , $XN = 0$ , $MMF = 470$ ) .....	70
FIGURE 3. 25 MAGNITUDE OF FLUX DENSITY FOR ( $\Lambda/G = 70$ , $T/\Lambda = 0.5$ , $XN = 0.8$ , $MMF = 470$ ).....	71
FIGURE 3. 26 COLOR SHADE RESULTS FOR $\Lambda/G = 70$ , $T/\Lambda = 0.5$ , $XN = 0.8$ , $MMF = 470$ .....	72
FIGURE 3. 27 COLOR SHADE DEFINITION .....	73
FIGURE 3. 28 COLOR SHADE FOR $\Lambda/G = 70$ , $T/\Lambda = 0.5$ , $XN = 0.8$ , $MMF = 470$ (MAGNIFIED). 73	
FIGURE 3. 29 FIELD INTENSITY COMPONENTS AT A POINT IN AN INTEGRATION PATH	76
FIGURE 3. 30 PATHS OF STRESS INTEGRATION TAKEN FOR A TOOTH PITCH.....	77
FIGURE 3. 31 NORMAL FIELD INTENSITY COMPONENT OF THE PATH BC AT $MMF = 707$ A.T, $\Lambda/G = 70$ , $T/\Lambda = 0.5$ , AND $XN = 0.4$ .....	79
FIGURE 3. 32 TANGENTIAL FIELD INTENSITY COMPONENT OF THE PATH BC AT $MMF = 707$ A.T, $\Lambda/G = 70$ , $T/\Lambda = 0.5$ , AND $XN = 0.4$ .....	80
FIGURE 3. 33 PATH OF INTEGRATION AROUND A RIGID BODY FOR TORQUE CALCULATION.....	82
FIGURE 3. 34 CALCULATION OF FLUX PER POLE .....	84
FIGURE 3. 35 NODES OF EXCITED COILS.....	86
FIGURE 4. 1 IN POSITION ALIGNMENT .....	89
FIGURE 4. 2 OUT POSITION ALIGNMENT .....	90
FIGURE 4. 3 DISTRIBUTION OF ELEMENTS IN AIRGAP AND IN HALF OF THE UPPER TOOTH DEPTH.....	92
FIGURE 4. 4 FLUX CONTOURS FOR IN POSITION ( $T/G = 8.8$ , $S/G = 8.0$ ) .....	93
FIGURE 4. 5 FLUX CONTOURS FOR OUT POSITION ( $T/G = 8.8$ , $S/G = 8.0$ ).....	94
FIGURE 4. 6 INVESTIGATING THE MMF DROP ON C-CORE.....	95
FIGURE 4. 7 SR2 GEOMETRY .....	99
FIGURE 4. 8 TAPERING ANGLE OF THE STATOR TOOTH.....	99
FIGURE 4. 9 HIGHER-ORDER ELEMENT PLANE53 .....	101
FIGURE 4. 10 MESH DISTRIBUTION OF SR2 AT 6 DEGREES (NORMALIZED POSITION = 0.2).....	102
FIGURE 4. 11 ELEMENT DISTRIBUTION IN THE AIRGAP REGION (THREE ROWS) AT ROTOR POSITION OF 6 DEG. ....	104
FIGURE 4. 12 NODES DISTRIBUTION IN THE AIRGAP REGION (FIVE ROWS OF NODES) AT ROTOR POSITION OF 6 DEG. ....	104
FIGURE 4. 13 NODES DISTRIBUTION AT TWO DIFFERENT ROTOR POSITIONS.....	106
FIGURE 4. 14 RIGHT COIL SET OF PHASE A .....	108
FIGURE 4. 15 SOLUTION CRITERIA. ....	110

FIGURE 4. 16 2D CONTOUR PLOTS FOR 3A EXCITATION AT XN = 0.6 .....	111
FIGURE 4. 17 FLUX DENSITY FOR 3A EXCITATION AT XN = 0.2 .....	111
FIGURE 4.18 STATIC TORQUE VS NORMALIZED POSITION OF SR2 .....	116
FIGURE 4.19 FLUX LINKAGE VS NORMALIZED POSITION OF SR2 .....	116
FIGURE 4. 20 STATIC TORQUE VS NORMALIZED POSITION OF SR2 (ANSYS & FLUX2D) .....	120
FIGURE 4. 21 FLUX LINKAGE VS NORMALIZED POSITION OF SR2 (ANSYS & FLUX2D)	120
FIGURE 4. 22 FLUX LINKAGE (WEB. TURN) AGAINST CURRENT FOR XN = 0. ....	123
FIGURE 4. 23 FLUX LINKAGE (WEB. TURN) AGAINST CURRENT FOR XN = 0.2. ....	123
FIGURE 4. 24 FLUX LINKAGE (WEB. TURN) AGAINST CURRENT FOR XN = 0.4. ....	124
FIGURE 4. 25 FLUX LINKAGE (WEB. TURN) AGAINST CURRENT FOR XN = 0.6. ....	124
FIGURE 4. 26 FLUX LINKAGE (WEB. TURN) AGAINST CURRENT FOR XN = 0.8. ....	125
FIGURE 4. 27 FLUX LINKAGE (WEB. TURN) AGAINST CURRENT FOR XN = 1. ....	125
FIGURE 4. 28 SR1 GEOMETRY AT 6DEGREES (NORMALIZED POSITION IS 0.2).....	127
FIGURE 4. 29 MESH OF SR1 AT 6DEGREES (NORMALIZED POSITION IS 0.2).....	129
FIGURE 4. 30 NODES DISTRIBUTION IN THE AIRGAP REGION OF SR1.....	130
FIGURE 4. 31 STATIC TORQUE VS NORMALIZED POSITION FOR SR1 (4A).....	132
FIGURE 4. 32 FLUX LINKAGE VS NORMALIZED POSITION OF SR1 .....	134
FIGURE 4. 33 FLUX LINKAGE VS NORMALIZED POSITION SR1 INCLUDING END EFFECT. .....	136
FIGURE 5. 1 TANGENTIAL FORCE VS TOOTH FLUX DENSITY FOR $\lambda/G = 40$ , XN = 0.2....	149
FIGURE 5. 2 TANGENTIAL FORCE VS TOOTH FLUX DENSITY FOR $\lambda/G = 40$ , XN = 0.4....	149
FIGURE 5. 3 TANGENTIAL FORCE VS TOOTH FLUX DENSITY FOR $\lambda/G = 40$ , XN = 0.6....	150
FIGURE 5. 4 TANGENTIAL FORCE VS TOOTH FLUX DENSITY FOR $\lambda/G = 40$ , XN = 0.8....	150
FIGURE 5. 5 NORMALIZED PERMEANCE VS TOOTH FLUX DENSITY FOR $\lambda/G = 40$ , XN = 0.0 .....	151
FIGURE 5. 6 NORMALIZED PERMEANCE VS TOOTH FLUX DENSITY FOR $\lambda/G = 40$ , XN = 0.2 .....	151
FIGURE 5. 7 NORMALIZED PERMEANCE VS TOOTH FLUX DENSITY FOR $\lambda/G = 40$ , XN = 0.4 .....	152
FIGURE 5. 8 NORMALIZED PERMEANCE VS TOOTH FLUX DENSITY FOR $\lambda/G = 40$ , XN = 0.6 .....	152
FIGURE 5. 9 NORMALIZED PERMEANCE VS TOOTH FLUX DENSITY FOR $\lambda/G = 40$ , XN = 0.8 .....	153
FIGURE 5. 10 NORMALIZED PERMEANCE VS TOOTH FLUX DENSITY FOR $\lambda/G = 40$ , XN = 1.0 .....	153
FIGURE 5. 11 NORMAL FORCE VS TOOTH FLUX DENSITY FOR $\lambda/G = 40$ , XN = 0.0.....	154

FIGURE 5. 12 NORMAL FORCE VS TOOTH FLUX DENSITY FOR  $\Lambda/G = 40$ ,  $XN = 0.2$ ..... 154

FIGURE 5. 13 NORMAL FORCE VS TOOTH FLUX DENSITY FOR  $\Lambda/G = 40$ ,  $XN = 0.4$ ..... 155

FIGURE 5. 14 NORMAL FORCE VS TOOTH FLUX DENSITY FOR  $\Lambda/G = 40$ ,  $XN = 0.6$ ..... 155

FIGURE 5. 15 NORMAL FORCE VS TOOTH FLUX DENSITY FOR  $\Lambda/G = 40$ ,  $XN = 0.8$ ..... 156

FIGURE 5. 16 NORMAL FORCE VS TOOTH FLUX DENSITY FOR  $\Lambda/G = 40$ ,  $XN = 1.0$ ..... 156

FIGURE 5. 17 CROSS SECTION OF A 8/6 SWITCHED RELUCTANCE MOTOR ..... 157

FIGURE 5. 18 OPERATING POINT DETERMINATION ..... 158

FIGURE 5. 19 FLUX LINKAGE PREDICTIONS WITH ENDLEAKAGE CORRECTION FOR SR2  
..... 159

FIGURE 5. 20 PREDICTIONS OF STATIC TORQUE CHARACTERISTIC FOR SR2 ..... 160

FIGURE 5. 21 FLUX LINKAGE PREDICTIONS WITH ENDLEAKAGE CORRECTION FOR SR1  
..... 161

FIGURE 5. 22 PREDICTIONS OF STATIC TORQUE CHARACTERISTIC FOR SR1 ..... 162

FIGURE 5. 23 TORQUE-SPEED CHARACTERISTIC AT  $0^\circ$  ADVANCED ANGLE ..... 163

FIGURE 5. 24 TORQUE-SPEED CHARACTERISTIC AT  $4^\circ$  ADVANCED ANGLE ..... 164

FIGURE 5. 25 TORQUE-SPEED CHARACTERISTIC AT  $7.5^\circ$  ADVANCED ANGLE ..... 164

FIGURE 5. 26 TORQUE-SPEED CHARACTERISTIC AT  $11^\circ$  ADVANCED ANGLE ..... 165



# CHAPTER 1

## INTRODUCTION

### 1.1 General

A Switched Reluctance motor (SRM) is an electromagnetic, rotary machine in which torque is produced by the tendency of its movable part to move to a position where the inductance of the excited winding is maximized. SRM, with its simple design where the coils are placed on the stator (figure-1.1), has gained attention of variable speed drive applications with significant industrial relevance. Its wide usage mainly appears in some washing machine designs, vacuum cleaners, fans, and in the control rod drive mechanism of nuclear reactors. Moreover, SR motors are now used in such military applications as generators for turbine engines and pump motors for jet fighters. The main factors that gave importance to SRM are:

- Low construction complexity (low cost, long life),
- High reliability (no brush wear),
- High torque-to-mass ratio (high start-up torque),
- High speed operation,
- Possibility of sensorless speed control,
- Fast step response,
- Bidirectional rotation, and
- Better thermal characteristics (windings are on the outside of the motor).

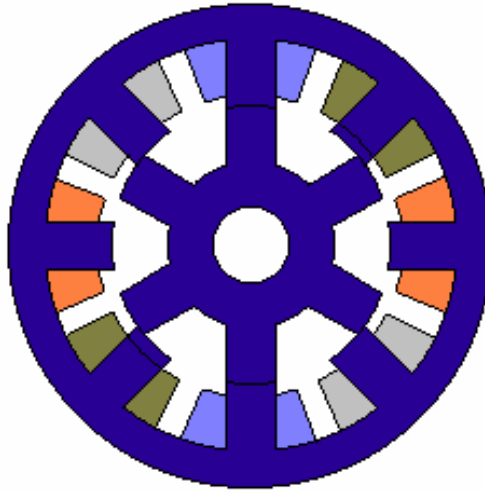


Figure 1. 1 Cross-section of a Four-phase SRM

In addition, the power stage of an SRM drive can be simpler and more reliable than that of induction motor drives under the absence of shoot-through problem that may be faced with ac or with brushless dc drives. Also the converter may have as many switches as the number of phases (or twice as much depending on the preference and expected characteristic) and therefore is cost effective [1].

However, SR motors have some drawbacks. First, they have no holding torque when windings are not excited. Second, oscillations and overshoot in step response exist. Finally, there are acoustic noise and speed ripples caused by high torque ripple.

Generating the relationships between the flux linkage versus rotor position as a function of the phase current has a great deal of importance for finding and predicting the performance characteristics of an SR motor.

## **1.2 Importance of Flux Linkage Characteristics**

In any design process, a designer has to be able to predict the performance of the product with acceptable accuracy. However, designing an SRM is a complicated and multi-step process with significant variations in approaches and algorithms because it is inherently a nonlinear machine.

Flux linkage of switch reluctance motor (SRM) is a nonlinear function of both rotor position and phase current. Establishing this nonlinear mapping is the basis of computing the mathematical equations of SRM accurately. Ertan [2] stated that measured flux linkage characteristic is used for analysis of SRM performance. For design purposes however, it is essential to predict the flux linkage-current-position curves. This is a very difficult task because of the highly nonlinear behavior of the motor.

So flux linkage-current-position curves are curves that plot the flux linkage of a pole as a function of current and position of rotor from the unaligned (OUT) to the aligned (IN) position. They are required when implementing design algorithms that integrate both the system magnetic and mechanical equations for analysis of a particular design. Usually such curves are obtained from experiments or from field solution.

The following subsections show, in brief, two methods for prediction of flux linkage characteristics.

### **1.2.1 Analytical Estimation of Flux-Linkage-Current Curve**

To predict minimum and maximum permeance of SRMs, Corda [3] has adopted an approach in which he assumed circular and linear flux path segments. Flux paths are defined for IN and OUT positions of the teeth. In the IN position the leakage flux is neglected and the saturation of teeth is accounted for, using B-H curve of the magnetic material and assuming a uniform flux distribution with the pole and the back iron. In the

OUT position, flux leakage along the pole is also accounted for, as well as the end winding leakage. To account for the end winding leakage a fictitious air gap with length equivalent to the average of the flux paths in the radial plane is considered. The model assumes repeating sections of iron with a width equal to core length and separated by an assumed distance  $2n$ . Carter's coefficient is used to find the effective core length. Flux linkage-current curve is found to match the measurements with an accuracy of 5%.

Miller [4] presented an approach for quick calculation of the flux linkage curve. The method of calculation of the IN and OUT magnetization curves is essentially the same as Corda's approach. However, in this case the flux paths are not forced to be parts of circles or straight lines, but calculated from dual energy method [5]. To account for the end winding flux an approximation is used. The author reports a comparison of calculations and measurements for 9 motors. The largest error is about -12% while the smallest is +2% in the OUT position.

As it is correctly pointed out in reference [4], the main issue in such a prediction is not only the accuracy for known motors but correctly predicting the trend as the dimensions change. The authors point out that dual energy method overcomes error sources due to inflexible flux paths adopted by Corda.

For the intermediate rotor positions, flux linkage-position curve is considered with current as a parameter (Fig-2). To determine the desired variation the curve is divided into 3 sections, where the mid section is assumed to be linear. The author then proceeds to make a shape of the curve in each section. SRM performance predictions using these curves are reported to be quite accurate. [1]

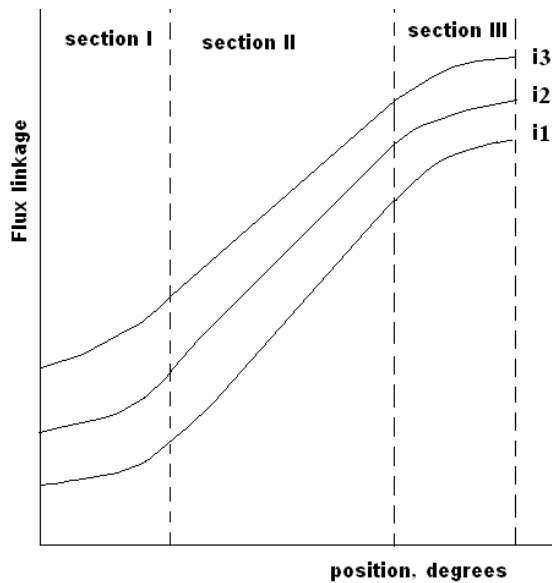


Figure 1. 2 Typical flux linkage vs. position curve of an SRM

### 1.2.2 Field Solution for Obtaining Flux Linkage Curves

An obvious solution to determine the flux linkage curves at the design stage is to use field solution techniques [6, 7, 8]. At present a number of professional programs exists for this purpose. Two-dimensional field solutions are quite straightforward to model. Solutions may take 10-20 minutes for a given position on a powerful processor, depending on the saturation level and the section of the motor modeled. However, using such programs requires considerable training. Although such programs may be used to calculate the flux linkage-position-current curves, they are not very handy for design optimization. Furthermore end effects are not included and this may lead to considerable error in prediction of the flux linkage curves. Therefore errors may be expected in prediction of the performance unless some means are used to account for the end field. A possibility in this respect is to use an approach similar to the one described in reference [3]. Three-dimensional field solutions on the other hand lead to accurate results; however, they are quite demanding as far as the solution platform

capability is concerned. Also modeling of three-dimensional problems is quite difficult and often is not practical.

However, the designer often requires a sufficiently accurate method of prediction, which shows general trends for parameter variation. With such a method it is possible to evaluate a sufficiently large number of alternatives. A method suitable for this purpose has been presented in reference [9]. This method is based on a set of normalized permeance-flux density ( $P_n$  vs.  $B_t$ ) force-flux density ( $F$  vs.  $B_t$ ) data. The data are obtained by solving the magnetic field of an identical doubly-salient model.[1]

### **1.3 Ertan's Model**

In deriving the model, Ertan [11] assumed that the windings are sufficiently far away from the airgap region so that a considerable proportion of the pole can be excluded from the model. He also assumed that it is possible to unroll the repetitive element without distorting the airgap field. In addition, the field is assumed to be two dimensional since the airgap is very small compared with the stack length. He also, for further simplifications of the model, neglected the tooth taper and slot curvature which don't affect the predictions more than a few percent. Consequently, as shown in figure-1.3, he obtained the final form of the teeth suitable for the preparation of good distribution for numerical solution of the problem. In figure-1.3,  $s$  is the slot width,  $t$  is the tooth width,  $g$  is the airgap length, and  $d$  is the slot depth.

According to boundary conditions, an equipotential line behind the stator teeth is assumed. While the rotor equipotential is assigned the value 0 and the side boundaries of the model is set to be vertical flux lines; that is, let  $\phi$  stands for the scalar potential, then the following assumptions for the boundary conditions are applied on the model boundaries:

$$\phi = \text{const. on AB}$$

$$\phi = 0 \text{ on CD}$$

$$\frac{\partial \phi}{\partial y} = \text{const. on AC and BD}$$

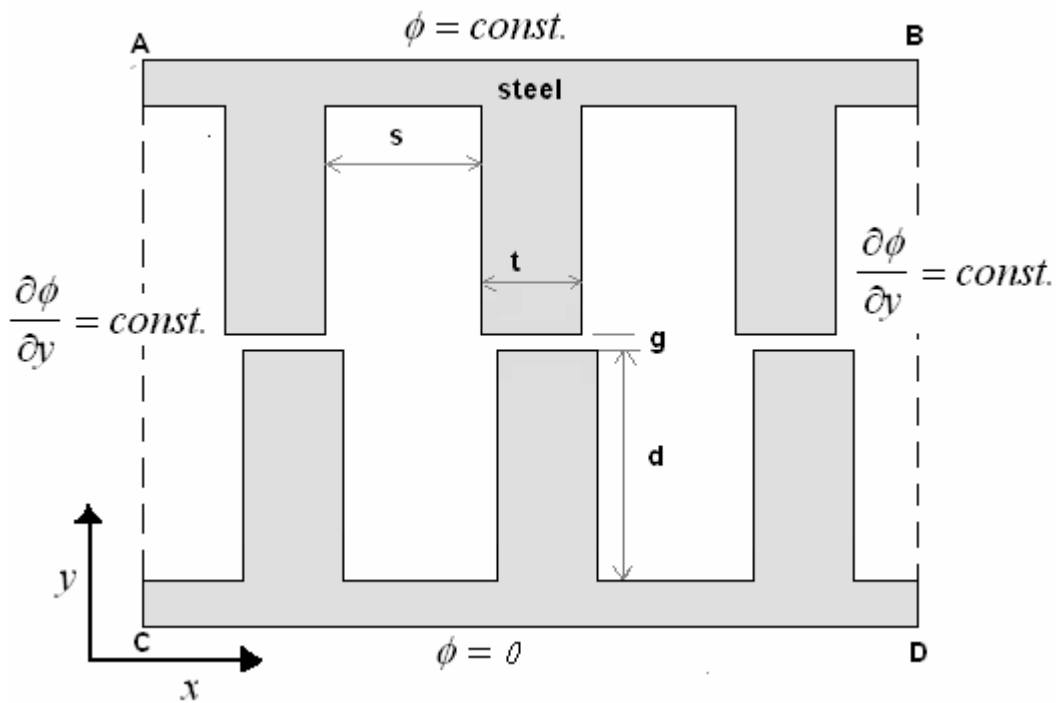


Figure 1. 3 Ertan's Model

In Ertan's model, the upper and lower halves of the model are symmetrical. Moreover, the model is very simple and universal; it can be adjusted to represent different structural parameters and relative positions of teeth. In figure-1.3, the slot depth  $d$  is assumed to be as much as 40 times of the the airgap length  $g$ . This assumption is to eliminate the slot effect and can be considered as sufficiently deep. Another important point is that Ertan developed this model to calculate permeance and force only in the centered tooth. The aside teeth are just to well define the boundary conditions.

#### 1.4 Purpose of the Study

In his thesis [11], Ertan developed a method and provided data for identical doubly-salient reluctance motor. This data is in the form of normalized permeance-flux density ( $P_n$  vs.  $B_t$ ) force-flux density ( $F$  vs.  $B_t$ ) data. The method is based on numerical calculation of permeance using a field solution software developed by the author. However, the purpose of this study is to improve the accuracy of the data obtained by Ertan by using professional software tools based on finite element analysis. In addition, Ertan didn't calculate data of normal force acting on a tooth. So, another purpose of the author from this work is to generate a set of normal force data for doubly salient motor structures. This set of data can be one of the bases for researches interested in minimization and prediction of the acoustic noise emitted from variable reluctance motors. Cameron, Lang and Umans [10] made several experiments in order to understand the main noise components of SRMs. They claimed that the most salient noise source is the radial deformation of the stator due to the radial (normal) force. It is reminded that normal force is much larger than tangential force. Therefore, generating the data of normal force is very important to be included in this work and may be utilized when studying the phenomenon of the acoustic noise, as done in a recent work by Erdal Bizkevelci [12].

To summarize, the author, firstly, is going to build a model similar to Ertan's and suitable to be solved in finite element softwares; ANSYS 11.0 and FLUX2D. The aim of solutions is to compute the following, for different relative positions and excitations:

- Tooth flux density
- Normalized permeance
- Tangential force
- Normal force



However, before proceeding with producing the data, the FE model is tested by comparing the permeance computed from the proposed model with Mukerji and Neville's analytical solutions for obtaining the permeance of doubly-salient structures. Further tests are carried out by comparing the FE model solution results (flux linkage and force-position curves) of two SR motors with measured results.

## **CHAPTER 2**

### **FINITE ELEMENT ANALYSIS**

#### **2.1 A Brief History**

Finite Element Analysis (FEA) was first developed in 1943 by R. Courant, who utilized the Ritz method of numerical analysis and minimization of variational calculus to obtain approximate solutions to vibration systems. After that, a paper published in 1956 by M. J. Turner, R. W. Clough, H. C. Martin, and L. J. Topp developed a broader definition of numerical analysis. By the early 70's, FEA was limited to expensive powerful computers generally owned by the aeronautics, defense and automotive industries. Since the price of computers has rapidly decreased with a significant increase in computing power, FEA has reached an incredible precision. Now computers can produce accurate results for all kinds of parameters.

#### **2.2 What is Finite Element Analysis?**

FEA consists of a computer model of a material or design that is stressed or excited and analyzed for specific results. It involves dividing a given geometry into a mesh of small elements, solving for certain variables at the nodes of these elements, and then interpolating the results for the whole region. The size, shape and distribution of the elements determine to a great degree the accuracy of the results.

“In general, the finite element method models a structure as an assemblage of small parts (elements). Each element is of simple geometry and therefore is much easier to analyze than the actual structure. In essence, a complicated solution is approximated by a model that consist of piecewise continuous simple solutions. Elements are called ‘finite’ to distinguish them from differential elements used in calculus. Discretization is

accomplished simply by sawing the continuum into pieces and then pinning the pieces together again at node points”. [13]

However, computing time depends on the number of nodes and elements, and the finer the mesh, the longer it takes to solve the problem. Hence, there is a trade off between accuracy and computing time. Generating an optimal mesh is a major topic and requires experience. The mesh should be fine enough for good detail with well-shaped elements where information is needed, but not too fine, or the analysis will require considerable time and space in the computer. This can require considerable user intervention, despite FEA software promotional claims of automatic good meshing.

There are generally two types of analysis that are used in industry: 2-D modeling, and 3-D modeling. While 2-D modeling conserves simplicity and allows the analysis to be run on a relatively normal computer, it tends to yield less accurate results. On the other hand, 3-D modeling produces more accurate results while sacrificing the ability to run on all but the fastest computers effectively. Within each of these modeling schemes, the programmer can insert numerous functions which may make the system behave linearly or non-linearly.

To summarize, in the finite element method, complexity of a problem is minimized by dividing the study domain into finite elements of simpler geometric shapes and then the partial differential equations related to these elements are solved by the numerical techniques. The finite element analysis of a physical event consists of following general steps:

- Representation of the physical event in mathematical model
- Construction of the geometry and its discretization to finite elements
- Assignment sources of excitation (if exist)
- Assignment of boundary conditions
- Derivation and assembling of the element matrix equations

- Solution of the equations for unknown variables
- Post processing or analysis of results obtained

### 2.3 Basic Principle

In the finite element method, unknown parameters are determined from minimization of energy functional of the system. The energy functional consists of various physical energies associated with a particular event. According to the law of conservation of energy, unless atomic energy is involved, the summation of total energies of a device or system is zero. On basis of this universal law, the energy functional of the finite element model can be minimized to zero. The minimum of energy functional is found by equating the derivative of the functional with respect to unknown grid potential to zero i.e if  $F$  is the functional and  $p$  is the unknown grid potential then the unknown potential  $p$  is found from the equation  $\frac{\partial F}{\partial p} = 0$ . The solutions of various differential equations of physical models including electro-magnetic system are obtained using this basic principle.

Since the model in this study has a steel material and is time invariant, the problem can be classified as nonlinear magnetostatic one. Thus, the energy functional in this case is given by:[14]

$$F = \int_v \left( \int_0^B H \cdot dB \right) dv - \int_v \left( \int_0^{Az} J \cdot dA \right) dv \quad (2.1)$$

where:

$v$  is the reluctivity (inverse of permeability) ,

$H$  is the field intensity vector,

$B$  is the flux density vector,

$\bar{J}$  is the current density vector,  
 $A$  is the magnetic vector potential, and  
 $A_z$  is the z-component of magnetic vector potential.

The first term in equation (2.1) is the energy stored in saturable linear or nonlinear materials, and the second term is the input electrical energy. If the permeability is not constant, then the stiffness matrix depends on the magnitude of  $B$  (and  $J$ ).

## 2.4 Maxwell's Equations

The governing laws of electromagnetic field problems can be expressed with well-known Maxwell's equations in differential form. These are given as,

$$\nabla \times \bar{H} = \bar{J} + \frac{\partial \bar{D}}{\partial t} \quad (2.2)$$

$$\nabla \cdot \bar{B} = 0 \quad (2.3)$$

where:

- $\nabla \times$  is curl operator
- $\nabla$  is gradient operator
- $\bar{H}$  is magnetic field intensity vector [A/m]
- $\bar{J}$  is current intensity vector [A/ m<sup>2</sup>]
- $\bar{D}$  is electric flux density vector [coulomb/m<sup>2</sup>]
- $\bar{B}$  = magnetic flux density vector [T].

Each of the above electromagnetic quantities can be a function of three space coordinates  $x$ ,  $y$ ,  $z$  and time  $t$  but in steady state condition  $\frac{\partial}{\partial t}$  part is zero and for such condition Maxwell's equation can simply be expressed as,

$$\nabla \times \bar{H} = \bar{J} \quad (2.4)$$

A field problem is greatly simplified when solved for the field potentials rather than the field itself [15]. In order to take the advantage of this simplification, the magnetic potential  $A$  is introduced from the vector identity of equation (2.5) in electromagnetics.

$$\nabla \cdot \nabla \times \bar{A} = 0 \quad (2.5)$$

It is true for any vector  $A$  and ascertains that equation (2.3) will always be satisfied when flux density  $\bar{B}$  is expressed in terms of vector potential  $A$  as,

$$\bar{B} = \nabla \times \bar{A} \quad (2.6)$$

The magnetic materials can be represented as a function of  $\bar{B}$  and  $\bar{H}$ ,

$$\begin{aligned} \bar{B} &= \mu \bar{H} \\ \text{or,} & \\ \bar{H} &= \nu \bar{B} \end{aligned} \quad (2.7)$$

where  $\mu$  and  $\nu$  are permeability and reluctivity of magnetic materials respectively. In case of ferromagnetic material, the  $B$ - $H$  relationship is nonlinear whereas for rare earth permanent magnet material, the relationship is linear and the author will not discuss it in this study since there are no magnets in the model.

Substituting equations (2.6) and (2.7) to (2.4), Maxwell's curl equation can be obtained as,

$$\nabla \times [\nu_0 \nu_r (\nabla \times \bar{A})] = \bar{J} \quad (2.8)$$

where,  $\nu_0$  and  $\nu_r$  are inverse of  $\mu_0$  (permeability of free space) and  $\mu_r$  (relative permeability) respectively.

The three components of vector  $B$  in Cartesian coordinate system from equation (2.6) are,

$$\begin{aligned} B_x &= \frac{\partial A_z}{\partial y} - \frac{\partial A_y}{\partial z} \\ B_y &= \frac{\partial A_x}{\partial z} - \frac{\partial A_z}{\partial x} \\ B_z &= \frac{\partial A_y}{\partial x} - \frac{\partial A_x}{\partial y} \end{aligned} \quad (2.9)$$

In the electric machine, the air gap between stator and rotor is very small over the entire axial length except at the end-turn region. In other words, the magnetic field is virtually two-dimensional at the study domain (figure-2.1,[16]) provided the effect of end-turn region is negligible. Therefore, use of 2D finite element analysis for most of the electric machines is justifiable. Additionally, 2D FEA requires less computing memory, power and time compared to 3D FEA.

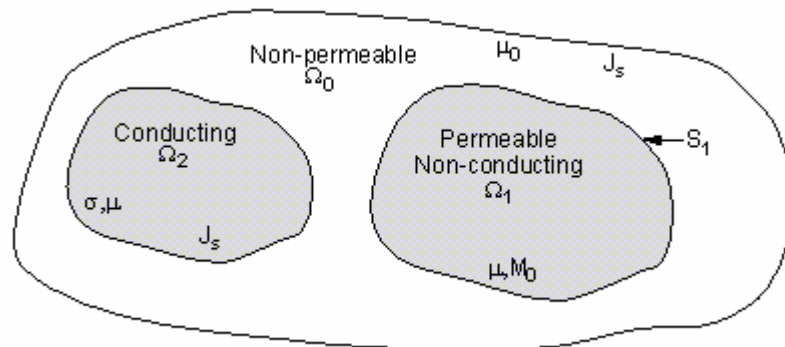


Figure 2. 1 Electromagnetic Field Domain

In tow-dimensional problems the magnetic vector potential  $\bar{A}$  is normal to the studied plane; hence, z component is non-zero. Consequently, components of magnetic flux density  $\bar{B}$  in 2D plane are given as,

$$B_x = \frac{\partial A_z}{\partial y}; B_y = -\frac{\partial A_z}{\partial x}; B_z = 0 \quad (2.10)$$

Therefore, the equation (2.8) can be simplified as,

$$\frac{\partial}{\partial x} \left( \nu \frac{\partial A_z}{\partial x} \right) + \frac{\partial}{\partial y} \left( \nu \frac{\partial A_z}{\partial y} \right) = -J_z \quad (2.11)$$

where  $J_z$  is the density of the excitation current source.

## 2.5 Mesh Formation

After the mathematical formulation of a physical model, the second important step in the FEM is to discretize the study domain. The process of discretization of the study domain is known as mesh formation. The accuracy of the solution greatly depends on the fitness of mesh. On the other hand, finer mesh requires larger computing time and memory of the computer. Therefore, better understanding of the domain regions and their fields is necessary to distribute the mesh in the most optimum way. The thumb rule of mesh distribution is that mesh should be as fine as possible where field changes rapidly.

A basic requirement of the discretization is that there should be neither overlap nor gaps between elements. Further, the elements should be connected via their vertices, or in other words, a vertex of an element can only be at the vertices of its neighboring



elements; it cannot be at the side of another element. In addition to these basic requirements, a good discretization should also address the following two points:

First, it should avoid the generation of narrow elements, or elements having a small inner angle. Although these elements are admissible, they can, nevertheless, increase the solution error since the error of the finite element solution is inversely proportional to the sine of the smallest inner angle. Therefore, all elements should be made close to equilateral. Second, one should note that the smaller the elements, the better the numerical solution. Since smaller elements will result in more unknowns, thus increasing the memory demand and computing time, it is necessary to keep the number of elements to the minimum for desired accuracy. A good practice is to use small elements where the solution is anticipated to have drastic variation, whereas in the regions where the variation is low the elements can be made larger.

There exist various types of elements which can be one, two and three-dimensional. Some of the most commonly used elements are shown in figure-2.2. The triangle element in 2D FEM and tetrahedron in 3D FEM are widely used since any polygon of 2D plane, no matter how irregular can be represented by the combinations of triangles and any polyhedron of the 3D plane as a combination of tetrahedrons.

The corner point of a finite element is called grid point or node. The main task of the FEM computation is to solve for all unknown node potentials. Each element has a material property that may or may not be different from the surrounding elements. Excitation may also present within the element or at the nodes.

After the mesh formation, a polynomial shape function or interpolation is derived for the unknown variables. In a typical triangular element as shown in figure-2.3, it is assumed that the unknown potential 'A' can sufficiently be represented by the following polynomial expression:

$$A = a + bx + cy \quad (2.12)$$

where,  $a$ ,  $b$  and  $c$  are some constants that will be determined in the process. Thus, the real solution of the potential is replaced by the discretized function in the  $xy$  plane of the problem. Although a potential function is discretized, its distribution in the region remains continuous through out. Therefore, the approximate of equation (2.12) is discrete but continuous everywhere and can be differentiated anywhere [15].

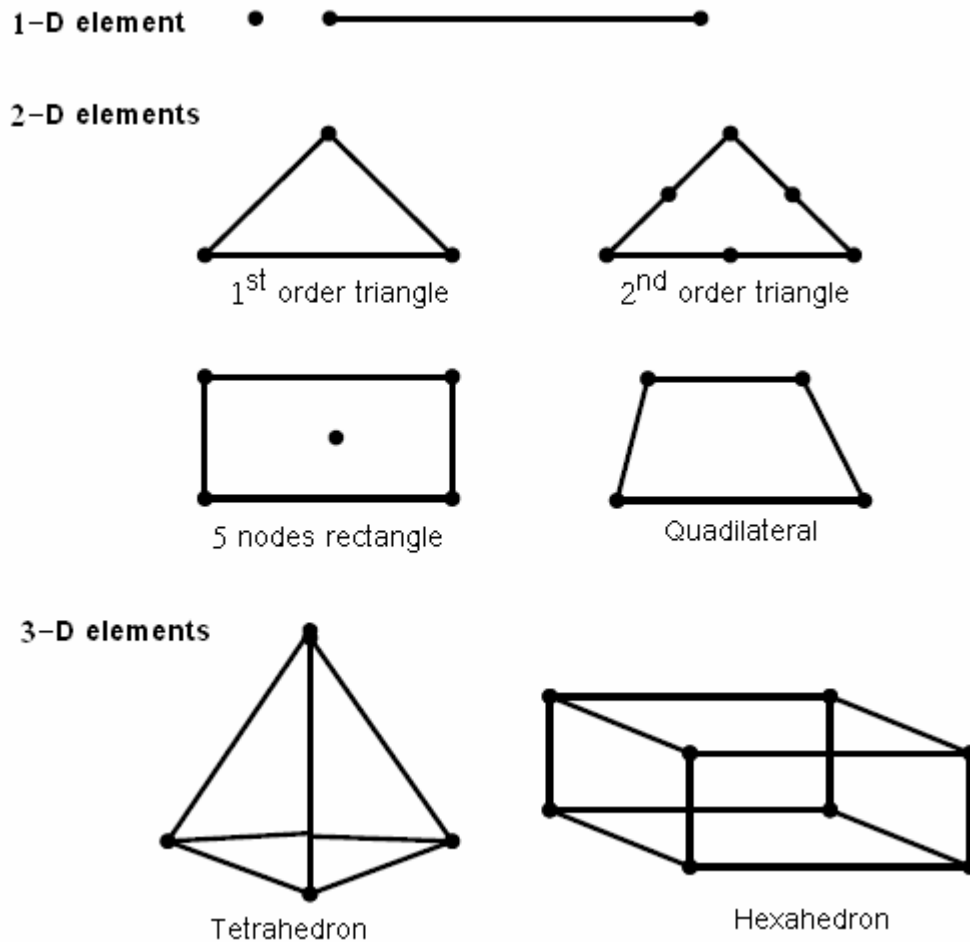


Figure 2. 2 Some basic elements used for mesh formation in a FE study, [15]

The constants  $a$ ,  $b$  and  $c$  are estimated from the three independent simultaneous equations of potentials that can be derived for three vertices of the triangle which given as,

$$a + bx_i + cy_i = A_i \quad (2.13)$$

$$a + bx_j + cy_j = A_j \quad (2.14)$$

$$a + bx_k + cy_k = A_k \quad (2.15)$$

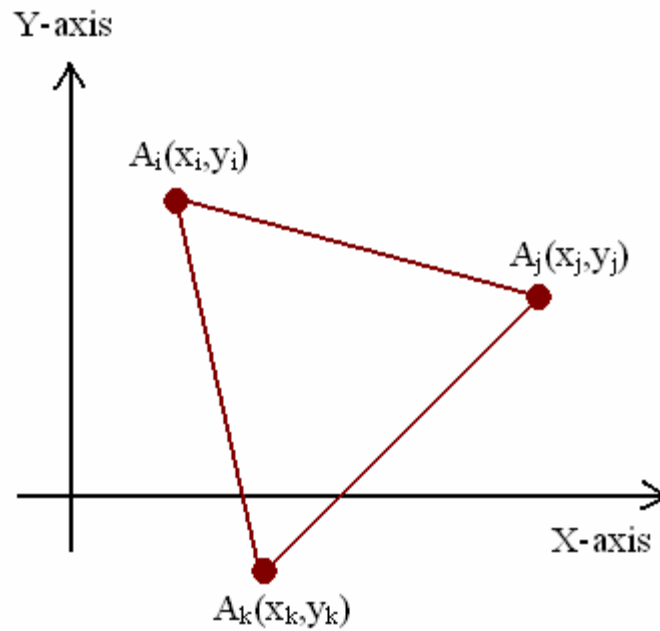


Figure 2. 3 The magnetic vector potential at the node of a typical triangular element

These equations can also be represented in a matrix form. The matrix of co-efficient can be derived from these equations as, [15]

$$\begin{bmatrix} a \\ b \\ c \end{bmatrix} = \begin{bmatrix} 1 & x_i & y_i \\ 1 & x_j & y_j \\ 1 & x_k & y_k \end{bmatrix}^{-1} \begin{bmatrix} A_i \\ A_j \\ A_k \end{bmatrix} \quad (2.16)$$

Substituting these constants in equation (2.12) and after some simplifications, the magnetic vector potential  $A$  can be expressed as,

$$A = \sum_{i=1}^m A_i \alpha_i(x, y) \quad (2.17)$$

where,  $m$  is the number of nodes in the element and  $\alpha_i(x, y)$  is the position function.

The position function  $\alpha(x, y)$  for nodes  $i, j, k$  are given as,

$$\alpha_i = \frac{1}{2\Delta} [(x_j y_k - x_k y_j) + (y_j - y_k)x + (x_k - x_j)y] \quad (2.18)$$

$$\alpha_j = \frac{1}{2\Delta} [(x_k y_i - x_i y_k) + (y_k - y_i)x + (x_i - x_k)y] \quad (2.19)$$

$$\alpha_k = \frac{1}{2\Delta} [(x_i y_j - x_j y_i) + (y_i - y_j)x + (x_j - x_i)y] \quad (2.20)$$

where,  $\Delta$  is the area of triangle. It can be shown that because of interpolatory nature of position functions,

$$\alpha_i(x_j, y_j) = \begin{cases} 0, & i \neq j \\ 1, & i = j \end{cases} \quad (2.21)$$

Depending on complexity of the problem, higher order element and polynomials are also used to define shape functions. The above discussion is valid for first order elements. The following section discusses how matrix equations of elements are used to solve a complicated electromagnetic problem in the FEM.

## 2.6 Matrix Equations of Elements

In order to solve a field problem, the matrix equations of elements need to be derived and assembled. The two main methods to derive the matrix equations of elements are:

- The weighted residual method and
- Variational method.

In both the methods, the error between real and approximate solution is minimized to zero. The most commonly used technique to minimize this error is known as *Galerkin's method*. It is closely related to both the variational formulation and weighted residual approach. In fact, *Galerkin's method* is a special case of the very general weight residual method. In *Galerkin's method* residual weight and shape functions become same.

In general, any electromagnetic field problem of region  $\Omega$  with boundary condition of 'C' can be expressed by an operator equation such as,

$$F(u) = v \quad (2.22)$$

The equation (2.22) can also be rewritten as,

$$F(u) - v = R \quad (2.23)$$

where,  $R$  is the residue that needs to be minimized. For this purpose, an appropriate weighing function  $W$  is chosen and a double integration is applied to the product of  $W$  and  $R$  over the region  $\Omega$ .

The formulation of Galerkin, including permanent magnet and time varying case, is expressed as,

$$\int_{\Omega} \int W \left( v \frac{\partial^2 \bar{A}}{\partial x^2} + v \frac{\partial^2 \bar{A}}{\partial y^2} \right) dx dy + j \omega \sigma \int_{\Omega} \int W \bar{A} dx dy - \int_{\Omega} \int W J_0 dx dy = \int_{\Omega} \int W J_m dx dy \quad (2.24)$$

where,  $\omega$  is the angular velocity,  $\sigma$  is the conductivity of the material,  $J_0$  is the current density of the source, and  $J_m = \nabla \times H_c$  is the equivalent current density of permanent magnet.  $H_c$  is the maximum field intensity of the magnet.

After some simplification, equation (2.11) can be expressed in matrix form as,

$$[S][\bar{A}] = [I] + [PM] \quad (2.25)$$

However, in this study, there is no any magnet. So equation (2.25) becomes:

$$[S][\bar{A}] = [I] \quad (2.26)$$

where,  $[S]$  is the global coefficient matrix that is expressed in terms of magnetic properties and coefficients  $b, c$ .

$$[S] = \frac{v}{4\Delta} \begin{bmatrix} b_i^2 + c_i^2 & b_i b_j + c_i c_j & b_i b_k + c_i c_k \\ b_i b_j + c_i c_j & b_j^2 + c_j^2 & b_j b_k + c_j c_k \\ b_i b_k + c_i c_k & b_j b_k + c_j c_k & b_k^2 + c_k^2 \end{bmatrix} + j \frac{\omega \sigma}{12} \begin{bmatrix} 2 & 1 & 1 \\ 1 & 2 & 1 \\ 1 & 1 & 2 \end{bmatrix} \quad (2.27)$$

The matrix of nodal magnetic vector potential is given as,

$$[\bar{A}] = \begin{bmatrix} \bar{A}_i \\ \bar{A}_j \\ \bar{A}_k \end{bmatrix} \quad (2.28)$$

The matrix of nodal currents is given as,

$$[I] = J_0 \frac{\Delta}{3} \begin{bmatrix} 1 \\ 1 \\ 1 \end{bmatrix} \quad (2.29)$$

The equation (2.25) is solved for vector potential  $\bar{A}$  in a region  $\Omega$  that contains triangular elements with nodes  $i, j$  and  $k$ . Generally, the study domain consists of finite number of elements. The matrix equation of (2.25) is determined for each element. Thus, the size of total matrix equations is determined by the number of finite elements present in the study domain. However, nodes can be common to various adjacent elements in a region. This results in a number of zero elements in the main matrix. Consequently, the resultant matrix is sparse, symmetric and definite and it can be solved using a standard processor.

## 2.7 Boundary Conditions

The boundary conditions are imposed on the study domains of the electromagnetic field problems. It restricts the study domain to certain extent which in turns reduces the computational burden. Hence, the accuracy and efficiency of a FEM solution greatly depends on appropriate boundary conditions.

The boundary due to symmetry reduces the size of an element matrix considerably. For example, most of the rotating electric machines have identical full or half pole pitch. In such case, the modeling of one or half pole pitch is sufficient to represent the field problem adequately. Thus, the size of the element matrix for an electric machine can be reduced significantly.

In general, boundary conditions are categorized in to three main groups [15,17]. They are:

- Dirichlet boundary condition
- Neumann boundary condition
- Interconnection boundary condition

In the Dirichlet boundary condition, a specified value is assigned to the magnetic vector potential of a particular point. It forces the flux lines to be parallel to the boundary edge. In a rotating machine, the outer stator yoke may have Dirichlet boundary condition of  $\bar{A}=0$ . It is valid as long as the leakage flux beyond the stator yoke is negligible. High permeability of the stator core material normally ensures that the majority of the fluxes are contained in the stator yoke. Therefore, assumption of Dirichlet boundary condition at the edge of the stator yoke is a reasonable simplification.

The requirement in a Neumann boundary condition is that normal derivative of magnetic vector potential in the boundary must be zero. Neumann boundary condition is also known as natural boundary of a finite element domain. Hence, it is not required to be specified explicitly. The flux lines cross Neumann boundary orthogonally. Neumann boundary is normally imposed to a region that has symmetry. The flux lines are orthogonal to the plane in Neumann boundary.

Interconnection boundary is also known as cyclic or periodic boundary. It sets a constraint between two nodes which could be geometrically adjacent or at a particular interval. In the rotating electric machine, the interconnection boundary condition relates two nodes that are one or multiple pole pitches apart.

## **2.8 Methods of Solving System Equations**

The linear algebraic equations are generally solved by either direct method or iterative method. From theoretical point of view, the direct method should be capable of giving an exact solution of the linear algebraic equations. However, in reality due to the



rounding off errors, the solution is actually an approximation. On the other hand, the iterative methods are not affected by the rounding off errors. The iterative methods can also take advantage of the sparseness of the coefficient matrix of the linear algebraic equations.

It is mentioned earlier that the global matrix of the finite element model is large but sparse and positive definite. Hence, the global matrix equation of the finite element model can be efficiently solved by the iterative methods. One of the most efficient methods to solve such matrix equations is Incomplete Choleski Conjugate Gradient (ICCG) iterative method. It is a preconditioned conjugate gradient method. The simultaneous equation given in (2.30) can be solved by the ICCG method.

$$Ax = b \quad (2.30)$$

In this method, first an arbitrary initial solution  $x_0$  is estimated, and then the associated residual  $r_0$  is computed. The initial search  $p_0$  for the final solution is chosen in such a way that it coincides with  $r_0$ .

$$r_0 = Ax_0 - b \quad (2.31)$$

$$p_0 = r_0 \quad (2.32)$$

Afterward, a succession of residuals and search directions are computed in recursive steps as shown below:

$$x_{k+1} = x_k + \alpha_k p_k \quad (2.33)$$

$$r_{k+1} = r_k + \alpha_k Ap_k \quad (2.34)$$

where,

$$\alpha_k = \frac{p_k^T r_k}{r_k^T A p_k} \quad (2.35)$$

In order to determine the preconditioned conjugate gradient, the matrix  $A$  is modified by a positive definite and symmetric preconditioning matrix  $B$  as  $BAB^T$ . The equation (2.30) can be rewritten as,

$$(BAB^T)(B^{-T}x) = Bb \quad (2.36)$$

From equation (2.36),  $y = B^T x$  is solved using modified right side and the coefficient matrix. Later the convergence  $x$  is recovered from  $y$ . the search direction of successive steps are expressed as,

$$p_{k+1} = Br_{k+1} + \beta_k p_k \quad (2.37)$$

where scaling factor  $\beta_k$  is calculated as,

$$\beta_k = -\frac{p_k^T A B r_{k+1}}{p_k^T A p_k} \quad (2.38)$$

Any symmetric, positive definite matrix 'A' can be represented in the form of:

$$A = LL^T \quad (2.39)$$

where,  $L$  is a lower triangular matrix that has only zero elements above and to the right of its principle diagonal and  $L^T$  is its transposition. The process of computing  $L$  is known as triangular factorization and labeled as triangular factor of 'A'. If the matrix 'A' is sparse, Incomplete Choleski Factorization is the best way to construct a sparse, lower

triangular preconditioning matrix  $L$ . In this type of factorization, many elements of the Choleski factors are forced to zero so that the computing time and memory space can be saved. The resultant factorization is an approximation only, but accuracy can be improved with additional conjugate gradient steps. The incomplete Choleski factorization of the modified matrix  $BAB^T$  produces most of its Eigen values close to unity and all others remaining values are very close to each other. As a result, residual components corresponding to them can be eliminated with fewer conjugate gradient steps [15].

## 2.9 Iterative Method for Nonlinear Problems

It is well known that the most of the electromagnetic problems have nonlinear characteristics. Nonlinearity can be faced in the problems that have ferromagnetic property of the core material or existence of permanent magnets. Hence, the mathematical model of the electric machine consists of a set of nonlinear equations which can not be solved directly in closed form. These types of equations are solved using numerical iterative methods. Among various iterative schemes, Newton Raphson method is widely used for solving nonlinear finite element equations. The popularity of this method lies in the fact that it converges rapidly and has an unconditional stability. Here, the error in a given step decreases as the square of the error in the previous step. The formulation of Newton Raphson iteration method for FEM solution can be described in brief as follows:[19]

$$A' = A - \partial A' \quad (2.40)$$

where,  $A$  is the correct solution to be found and  $A'$  is the reasonably close estimate of  $A$ . Then the multidimensional Taylor's series gives the gradient of function  $F(A')$  as,

$$\frac{\partial F}{\partial A'_m} = \frac{\partial F}{\partial A'_m} \Big|_{A'} + \sum_n \frac{\partial^2 F}{\partial A'_m \partial A'_n} \Big|_{A'} \partial A'_n + \dots \quad (2.41)$$

However, when  $A = A'$ , all components of gradient vanishes. Thus, neglecting the higher terms of Taylor's series,

$$\partial A' = -P^{-1} \frac{\partial F}{\partial A'_m} \Big|_{A'} \quad (2.42)$$

where,  $P$  is the Jacobian matrix of Newton Raphson iteration and the element  $mn$  is given as,

$$P_{mn} = \frac{\partial^2 F}{\partial A'_m \partial A'_n} \Big|_{A'} \quad (2.43)$$

The difference  $\partial A'$  is estimated and added to the initial approximation of  $A'$  until it converges to  $A$ . Thus, an iterative process is established and for any step  $k$  it is expressed as,

$$A'^{(k+1)} = A'^{(k)} - (P^{(k)})^{-1} \frac{\partial F}{\partial A'_m} \Big|_{A'}^{(k)} \quad (2.44)$$

The precision of Newton Raphson method depends mainly on derivation of  $\frac{\partial F}{\partial A'_m}$  and

$$\frac{\partial^2 F}{\partial A'_m \partial A'_n}$$

Now let us consider the simplified version of (2.25),

$$\frac{v}{4\Delta} \begin{bmatrix} S_{ii} & S_{ij} & S_{ik} \\ S_{ji} & S_{jj} & S_{jk} \\ S_{ki} & S_{kj} & S_{kk} \end{bmatrix} \begin{bmatrix} A_i \\ A_j \\ A_k \end{bmatrix} = \frac{\Delta}{3} J \begin{bmatrix} 1 \\ 1 \\ 1 \end{bmatrix} \quad (2.45)$$

The  $B$ - $H$  characteristics of the stator and rotor core materials are nonlinear. In such a case, solution of equation (2.45) in one single iteration step is not possible. For simplicity, we will derive Newton Raphson form only for the first row of (2.45). The procedure is repetitive for other rows and will not be considered here. Let us assume:

$$F = \frac{v}{4\Delta} \begin{bmatrix} S_{ii} & S_{ij} & S_{ik} \end{bmatrix} \begin{bmatrix} A_i \\ A_j \\ A_k \end{bmatrix} - \frac{J\Delta}{3} \quad (2.46)$$

Taking derivation with respect to  $A$  gives,

$$\frac{\partial F}{\partial A_i} = \frac{v}{4\Delta} S_{ii} + \frac{1}{4\Delta} [S_{ii} A_i + S_{ij} A_j + S_{ik} A_k] \frac{\partial v}{\partial A_i} \quad (2.47)$$

$$\frac{\partial F}{\partial A_j} = \frac{v}{4\Delta} S_{ij} + \frac{1}{4\Delta} [S_{ii} A_i + S_{ij} A_j + S_{ik} A_k] \frac{\partial v}{\partial A_j} \quad (2.48)$$

$$\frac{\partial F}{\partial A_k} = \frac{v}{4\Delta} S_{ik} + \frac{1}{4\Delta} [S_{ii} A_i + S_{ij} A_j + S_{ik} A_k] \frac{\partial v}{\partial A_k} \quad (2.49)$$

The term  $\frac{\partial v}{\partial A}$  can be represented by using chain rule,

$$\frac{\partial v}{\partial A} = \frac{\partial v}{\partial B^2} \frac{\partial B^2}{\partial A} \quad (2.50)$$

In the equation (2.50), the term  $\frac{\partial B^2}{\partial A}$  is derived as follows:

We know from the earlier analysis that,

$$A = \frac{a_i + b_i x + c_i y}{2\Delta} A_i + \frac{a_j + b_j x + c_j y}{2\Delta} A_j + \frac{a_k + b_k x + c_k y}{2\Delta} A_k \quad (2.51)$$

$$\text{and} \quad B = \sqrt{B_x^2 + B_y^2} \quad (2.52)$$

where,

$$B_x = \frac{\partial A}{\partial x} = \frac{A_i b_i + A_j b_j + A_k b_k}{2\Delta} \quad (2.53)$$

$$B_y = \frac{\partial A}{\partial y} = \frac{A_i c_i + A_j c_j + A_k c_k}{2\Delta} \quad (2.54)$$

Therefore,

$$B^2 = \left( \frac{\partial A}{\partial x} \right)^2 + \left( \frac{\partial A}{\partial y} \right)^2 = \frac{(A_i b_i + A_j b_j + A_k b_k)^2 + (A_i c_i + A_j c_j + A_k c_k)^2}{4\Delta^2} \quad (2.55)$$

and

$$\frac{\partial B^2}{\partial A_i} = \frac{2b_i(A_i b_i + A_j b_j + A_k b_k) + 2c_i(A_i c_i + A_j c_j + A_k c_k)}{4\Delta^2} \quad (2.56)$$

$\frac{\partial B^2}{\partial A_j}$  and  $\frac{\partial B^2}{\partial A_k}$  can also be calculated in similar way. The second term of equation

(2.50),  $\frac{\partial v}{\partial B^2}$  comes from the nonlinear magnetizing curve of the core material which

can be represented in a number of ways for the computation purpose.

## 2.10 Representation of Nonlinear BH curve for FEM Computation

Normally, the magnetizing curve of a core material is represented by a set of discrete points in the computer. However, in iterative methods like Newton Raphson, continuous representation of data is necessary. Hence, for such cases, interpolation methods are used for data representation. There exists a number of models to describe the physical property of the ferromagnetic material for this purpose. Some of them are:[18]

*Simple analytical saturation curve:* It defines BH curve very quickly by combining a straight line and an arc tangent. In this model, the BH curve closely follows the approximate asymptote of the saturation. However, the difference between experimental curve and the model can be large in the saturation band region.

*Analytical saturation curve with bend adjustment:* This model is more accurate than the simple analytical saturation curve. In this model bend of the saturation is adjusted with the help of a co-efficient so that curve resembles closely to the curve obtained from measured data points. The smaller is the coefficient the sharper will be the bend in the BH curve.

*Spline saturation curve:* This model is based on the cubic spline functions. It defines the BH curves from the measured data. Computation wise it takes longer time but fits the experimental curve very well. It comprise of three main parts, first of which is a homographic function that passes through the origin and describes the bend, the second part is a connecting function that is tangent to the first and last parts of the curve and the third part is a straight line of slope  $\mu_0$ , of which ordinates at the origin is the saturated magnetization.

The construction of BH curve to use in the FEA by utilizing the above mentioned models is shown in figure-2.4. Usually, the spline model is chosen for the best accuracy

when data of BH curves comes from actual measurements. The analytical model serves best when quicker computation is necessary.

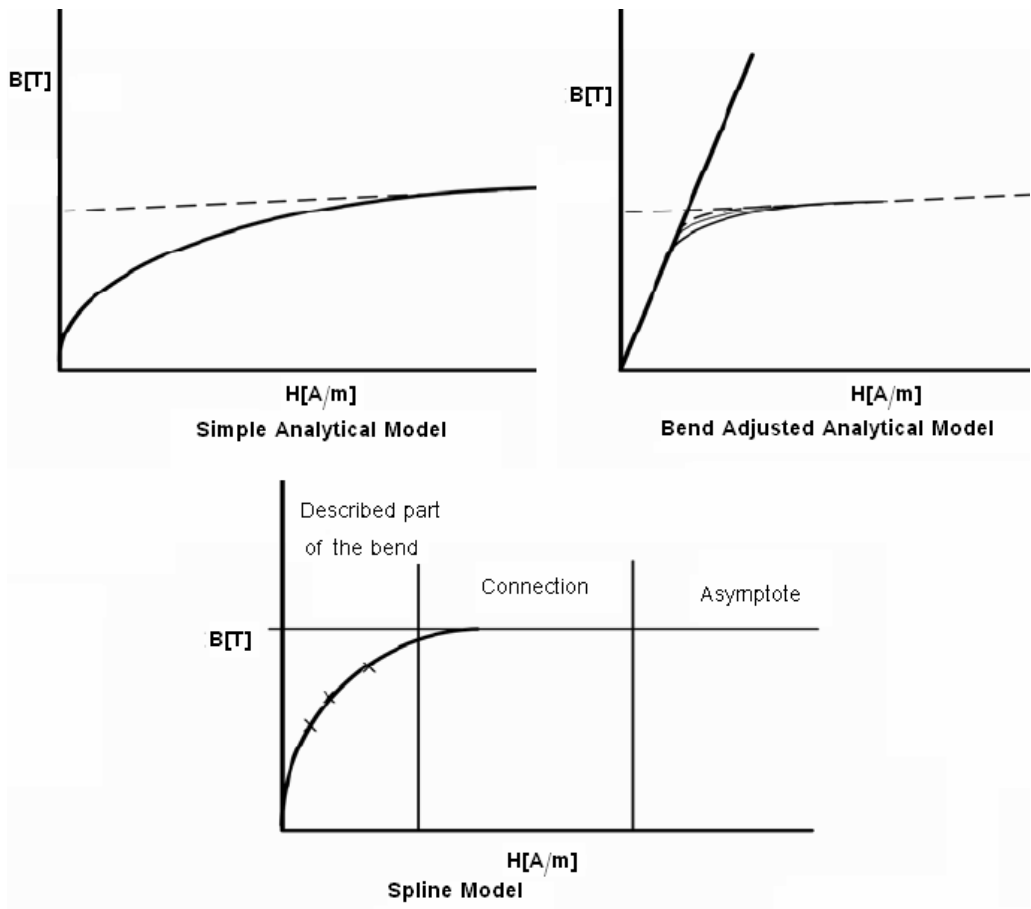


Figure 2. 4 BH models to represent nonlinear characteristic



## 2.11 Force Computations

There are two methods to compute the force in a 2D application: Virtual Works Method or Maxwell stress tensor method. If the virtual work principle for applied forces is used on individual elements of a rigid body, the principle can be generalized for a rigid body; when a rigid body that is in equilibrium is subject to virtual compatible displacements, the total virtual work of all external forces is zero; and conversely, if the total virtual work of all external forces acting on a rigid body is zero then the body is in equilibrium. The expression compatible displacements means that the elements remain in contact and displace together so that the work done by pairs of action/reaction inter-particle forces cancel out.

The virtual works method computes the electromagnetic force and torque exerted on parts that keep their shape and that are surrounded by air. The force exerted in a given direction is obtained by differentiating the magnetic energy  $W$  of the system with respect to a virtual displacement  $s$  of the object (eq-2.57) in the same direction (virtual angular displacement for the torque). This method supposes that the virtual displacement carried out does not change the saturation state of the non linear materials.[18]

$$F_s = -\frac{\partial W}{\partial s} \quad \text{in general} \quad (2.57)$$

$$F_s = \int_{vol} B^T \frac{\partial H}{\partial s} d(vol) + \int \left( \int_{vol} B^T dH \right) \frac{\partial}{\partial s} d(vol) \quad (2.58)$$

where:

$F_s$  : is the force element in the  $s$  direction

$W$ : is the magnetic energy of the system

$\partial s$ : is the virtual displacement.

Equation (2.58) defines the force element in  $s$  direction in terms of magnetic flux density and flux intensity based on virtual work method.

However, Maxwell stress tensor is used to determine forces on ferromagnetic regions. This force calculation is performed on surfaces of air material elements which have a nonzero face loading specified. For the 2D application, this method uses extrapolated field values and results in the following numerically integrated surface integral:[16]

$$F^{mx} = \frac{1}{\mu_0} \int_s A_n^T \begin{bmatrix} T_{11} & T_{12} \\ T_{21} & T_{22} \end{bmatrix} \begin{Bmatrix} n_1 \\ n_2 \end{Bmatrix} ds \quad (2.59)$$

where:

$$T_{11} = B_x^2 - 0.5 * |B|^2$$

$$T_{12} = B_x B_y$$

$$T_{21} = B_x B_y$$

$$T_{22} = B_y^2 - 0.5 * |B|^2$$

$$|B|^2 = B_x^2 + B_y^2$$

$n_1$  is the component of unit normal in  $x$  direction

$n_2$  is the component of unit normal in  $y$  direction

## 2.12 Conclusion

The finite element method is a numerical technique. In this method, the partial differential equations modeling the field problem are transformed into energy-related functionals. Approximate solutions are then sought to be the field problem extremize (or minimize) these functionals. By this procedure, a detailed modeling of the geometry of the field region is possible, and the results obtained are found to be accurate. Finite element method has several advantages; besides that it offers flexibility for modeling complex geometry, but also it yields stable and accurate solutions. In addition, it can handle nonlinear problems. Moreover, natural boundary conditions are implicit in the functional formulation.

In this chapter, finite element analysis of an electromagnetic two dimensional problems is briefly introduced. The main steps involved in the finite element analysis are discussed in detail. However, this is the background theory for such a numerical method. What is discussed in force computation section represents the way that FEA software tools use to compute the final result of the force acting on a rigid body. But in some models, one can't depend on the results obtained by these tools unless the conditions of these methods apply. The author will discuss later how force results can be obtained by plotting suitable paths around the rigid body.

## **CHAPTER 3**

### **DEVELOPING A MODEL FOR PERMEANCE AND FORCE CALCULATION**

#### **3.1 Outline**

This chapter discusses the model required to obtain the normalized data by finite element analysis. Later on, a detailed discussion of how to build and mesh the geometry by FLUX2D-8.1 is included. Definition of materials, boundary condition, and solution accuracy is also included. At the end of this chapter, several steps were applied to investigate the model whether it is defined well or not. In addition, the computations of force, permeance, tooth flux density and torque are discussed to show how the author obtained this data.

#### **3.2 Introduction**

Ertan's model is basically composed of two identical groups of teeth made of steel as shown in figure-3.1. As explained in chapter one section 1.3, this model was developed by Ertan for the aim of computing tangential force and normalized permeance only for the center tooth for different relative positions and several excitation levels. The boundary conditions are shown on the figure in terms of scalar potential. It is important to clarify that  $x$  stands for the relative position between the upper and the lower teeth. And it extends from 0.0 which stands for aligned position up to 8.6 mm which stands for OUT position in which the lower teeth are centered in the slots of that for the upper ones. It is worth mentioning that in all his calculations, Ertan set the tooth pitch as 17.2

mm. Also, it is important to remember that the stack length of the model is taken as one meter.

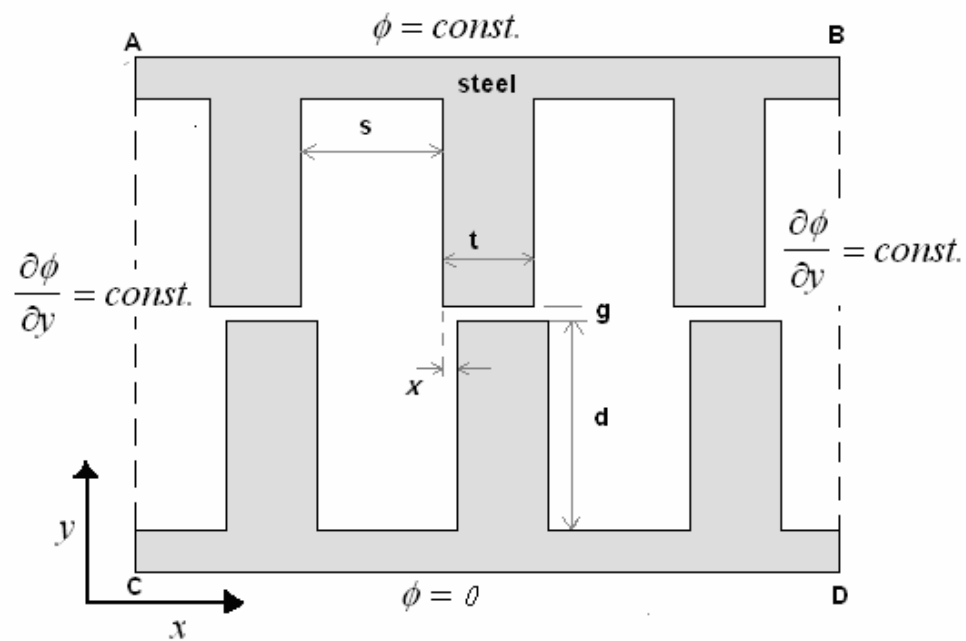


Figure 3. 1 Ertan's Model

This is the basic model that the author will depend on in this study. However, this model is not suitable to be used by a FE software tool. In other words, the author will redefine the model in such a way to be compatible with FE tool matching the basic assumptions set by Ertan. And then to study the relation between both permeance and force versus tooth flux density for various positions, dimensions and excitation levels.

There are many software tools existing based on finite element method such as ANSYS, OPERA, VECTOR FIELDS, MAXWELL, FLUX2D, FIELD PRECISION... However, in this study, ANSYS11.0 and FLUX2D-8.1 have been used. The following section discusses the definition of the model that the author used in this study as performed in FLUX2D.

### 3.3 Model of Normalized Data

As mentioned before, the model, shown in figure-3.2, consists of three upper teeth and three lower teeth. And the aim is to compute normalized permeance for a tooth pitch and force acting on the center tooth as we shift the lower teeth starting from the aligned position (IN position) up to the unaligned position (Out position). Since many results have to be obtained, the model must be easy to modify according to dimensions and excitation levels. A coil, for the aim of changing excitation level, is wound around a core to complete the magnetic circuit. This coil is divided into two parts; coil-in, where the current is passing normally inward the plane, and coil-out, where the current is passing normally outward the plane. The core is given the name 'C-core' and defined to have a large permeability to not affect on the basic assumptions. Although the dimensions of this core are not so important, they are placed on the figure. In addition, a shell is placed around the model for the aim of defining the boundary conditions as it will be explained later. This shell is considered to be the boundary of the study domain.

For figure-3.2, the following notations of dimensions were used:

$d$  : tooth depth ( $40 \cdot g$ )

$g$  : air gap length,

$s$  : slot width, the distance between two successive teeth,

$t$  : tooth width,

$x$  : relative position between upper and lower teeth and equals to  $X_n \cdot \lambda/2$ ,

$X_n$  : normalized position, 0.0, 0.2, 0.4, 0.6, 0.8, 1.0

$\lambda$  : tooth pitch and is equal to  $(t + s)$ .

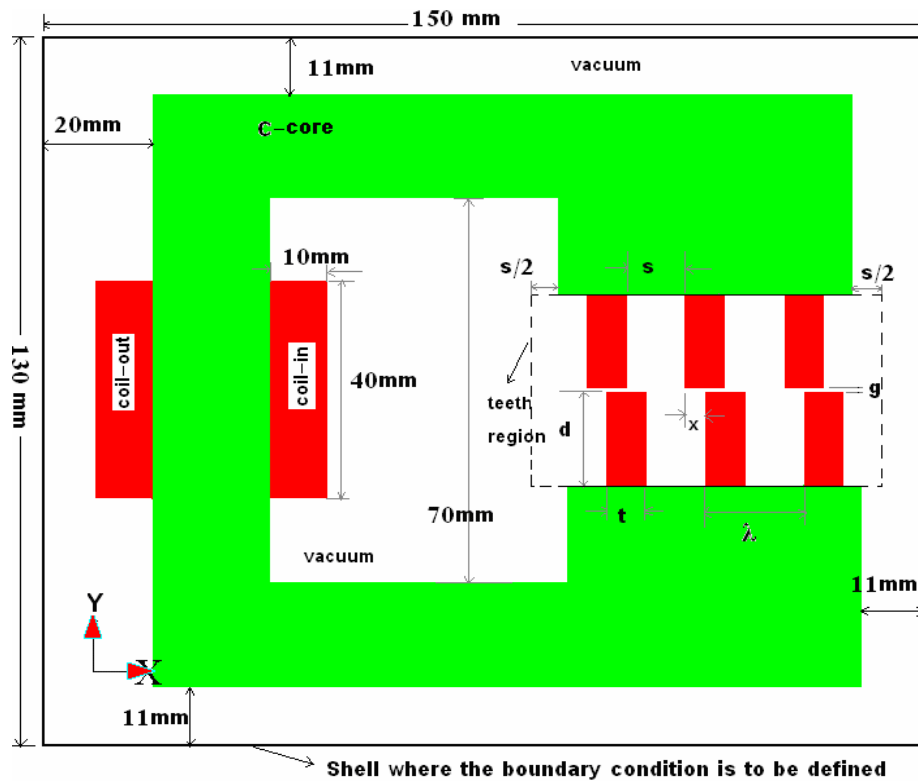


Figure 3. 2 Model Geometry for  $X_n = 0.4$ ,  $t/\lambda = 0.4$

### 3.4 Model Definition in Flux2D

Flux2D-8.1 software has a friendly user interface. Figure-3.3 shows the layout of Flux2D Supervisor. However, the following general steps must be performed in order to build and solve a magnetostatic problem:

1. Drawing the Geometry of the actual design (PreFlux2D)
2. Building faces (PreFlux2D)
3. Building mesh (PreFlux2D)
4. Definition of materials (cslmat)
5. Creating a physical problem (Prophy)
6. Solving the problem (SOLVER\_2D)
7. Getting the results (Flux2D- PostPro)

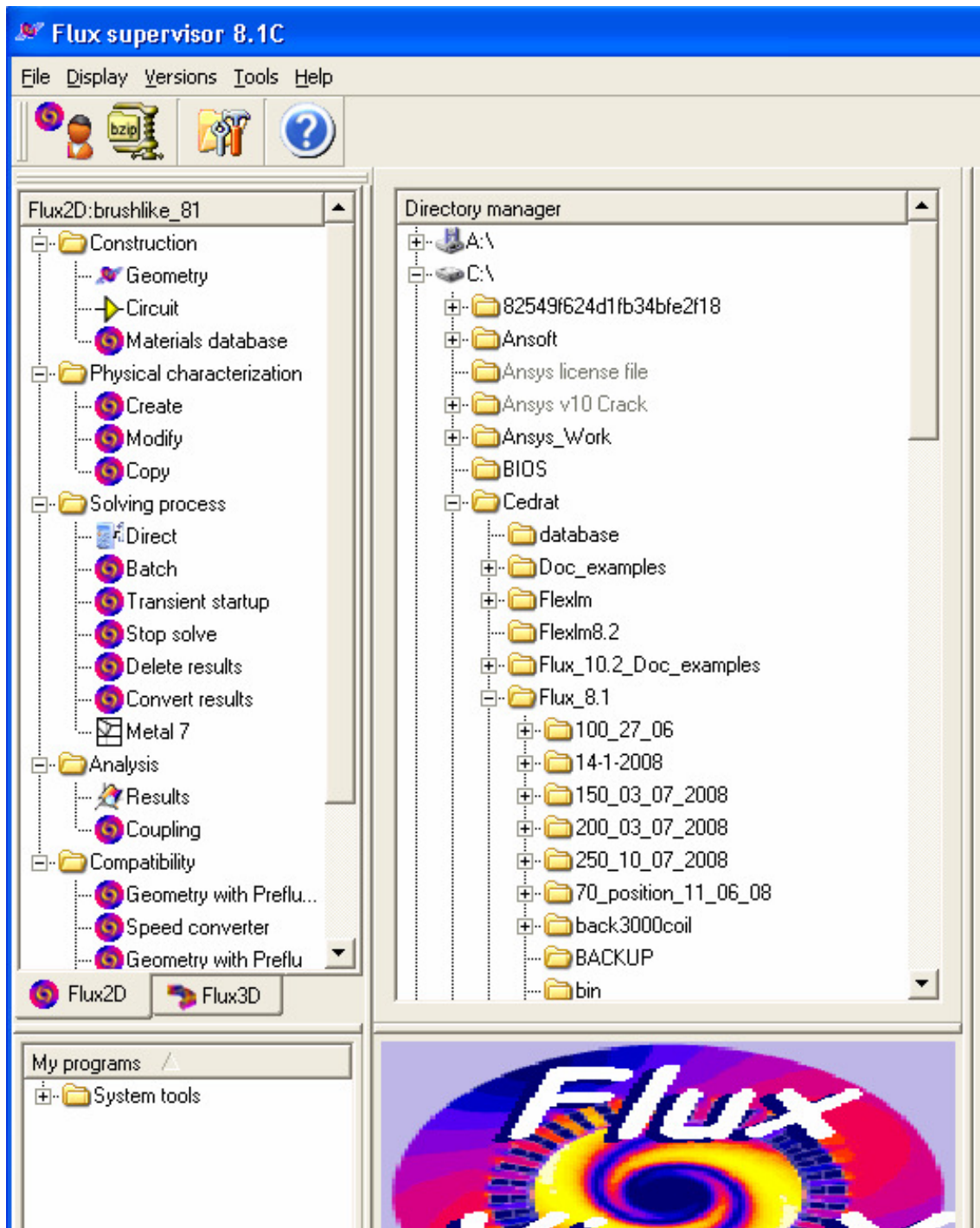


Figure 3. 3 Layout of Flux2D Supervisor



### 3.4.1 Definition of Geometry in Flux2D8.1

The geometric pre-processor of PREFLU\_2D is of the boundary type: this indicates that a face is described by the lines that border it and a line is created using points. This leads to a progressive construction of the geometry: first the points, then the lines, and finally the faces. The points and the lines are essentially defined in a manual manner, while the faces are defined in an automatic manner.

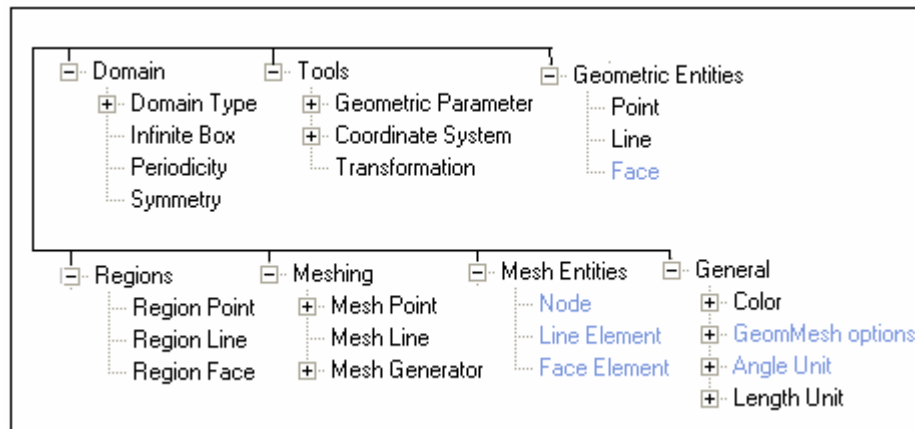


Figure 3. 4 Tree of commands of Preflux2D

To start building the geometry in Flux2D8.1 (Preflux2D), one has to define the coordinate systems which are Cartesian type. In this problem, two coordinate systems were built, that is; in Preflux2D and from DATA menu, we choose ADD Coordinate system. The first one has the name “XY” with (0,0) origin which is the reference point for the model and stands for the tooth tip corner of the upper tooth. The second coordinate has the name “ROTOR\_CORD” and has the origin (x, -gap) as shown in figure-3.5, where x and gap were defined before in Preflux2D as “geometric parameters” from the same menu. They stand for the shift between stationary and moving teeth in positive x-direction and the air-gap width, respectively. That is, since it

is a simple model, the author defined all the points of the geometry expressed by the airgap length, tooth pitch, slot width and tooth width. This has a great benefit in modifying the geometry, it is quick and easy just by changing x and gap (or tooth width if needed) to the desired values without building a new geometry which wastes much time. As an example, for aligned position, x must be set to 0.0, for 0.4 position, x equals to 3.44 mm, and so on. Also the same benefit we get from defining (-gap) as we have to solve for different lengths of airgap.

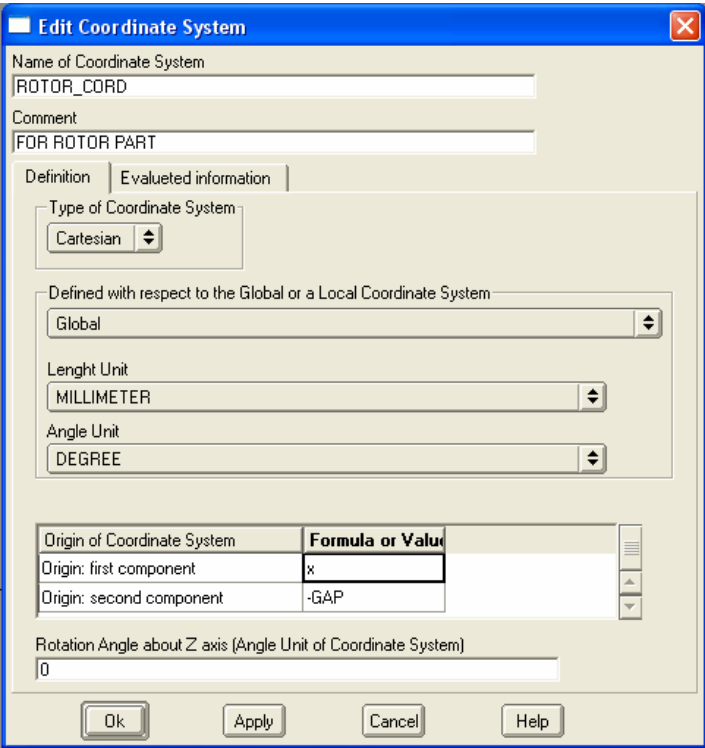


Figure 3. 5 Adding “Rotor Coordinates” Menu

After defining coordinate systems, building the geometry can be started referring each point to the corresponding coordinate system. It is straight forward just by entering the coordinates of points from the ADD menu as shown in figure-3.6. Then, draw the

connecting lines between points that form the model from the same menu “DATA>>ADD>> Line” as shown in figure-3.7.

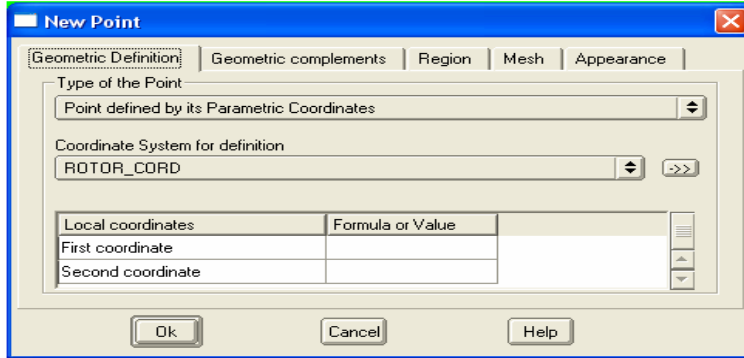


Figure 3. 6 Adding “new POINT” Menu

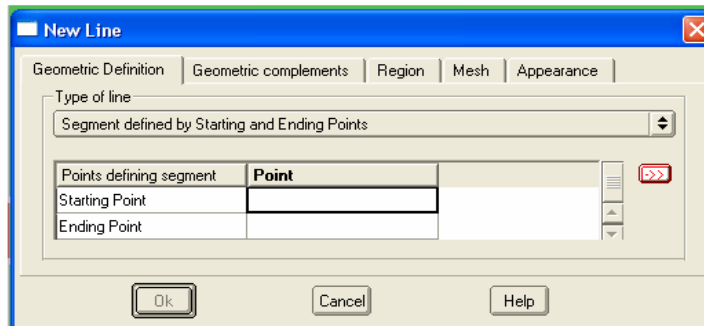


Figure 3. 7 Adding “New Line” Menu

Building faces is also important to finish any geometry in Flux2D. From “ACTIONS” menu, one has to choose build faces. This step defines the entire areas inside closed paths. Previously, adding regions names should be done to assign those names to the corresponding faces or regions. Then one must assign names of regions to the corresponding areas that form the complete geometry (figure-3.2) as a preparation for problem definition in Flux2D-Prophy module.

### **3.4.2 Meshing the Model**

Once building the whole geometry and assigning names of regions to the corresponding areas as explained in section 3.4.1 is completed, one has to start meshing the model; that is, we must convert the model into finite element representation. However, computing time depends on the number of nodes and elements, and the finer the mesh, the longer it takes to solve the problem. Hence, there is a trade off between accuracy and computing time. Generating an optimal mesh requires experience and some luck. However, since the model has a simple geometry composed of three stationary teeth and three moving teeth placed one the opposite side, assigning very small mesh points, but not too much small, to the teeth will not lead to have long time required for solving the problem. How to obtain mesh and how it will be changed when the model is modified to get another shift is explained in the following sections.

#### **3.4.2.1 Description of the Automatic/Mapped Mesh Generator in FLUX**

Mesh elements are created by either the automatic mesh generator (triangular elements) in Preflux 8.1 or mapped mesh, and the default mesh is usually satisfactory in terms of quality, accuracy and size (number of nodes and elements). However, because the automatic mesh generator is controlled by predefined mesh weights, it may not be appropriate in every case. So the user can control the density of the mesh through custom mesh points in C-core and slots. With the Mesh\_Points option, Preflux 8.1 automatically adjusts the distribution of nodes between two geometric points.

The mapped mesh generator allows the user to mesh faces in triangular or rectangular elements. The main quality of this mesh generator consists of the total user's control of the number and quality of the obtained elements. Also it allows the user to benefit from a possible anisotropy of the physical proprieties for the skin meshing or in magnetic circuits. The use of mapped mesh is limited to simple geometric domains:

- faces built starting from four lines or that can be assimilated to rectangles.
- volumes constructed starting from six faces of four lines each.

The mesh adjustment (number of elements in the two or three directions) is made starting from the lines. There is an important rule stating that the number of nodes on a line must be equal to the number of those on the opposite line. In other words, nodes on line 'a' equal to nodes on line 'a'' as shown in figure-3.8, the same is applied for other opposite lines.

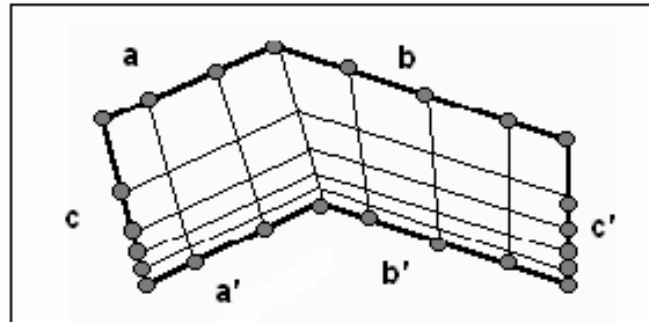


Figure 3. 8 Mapped mesh example

The mapped mesh generator is a relatively powerful one. However, if the geometry of a face goes too far away from the square domain of reference, the mesh quality is affected, and the mesh may become incoherent.

To summarize, the mapped mesh is often correct on faces with four lines. For such faces, the mesh quality is affected only if the corners are not corners any longer. For the faces with more than four lines, the mesh quality is affected when the face concavity becomes too important. However, a precise limit cannot be given.

### 3.4.2.2 Meshing the Model in Flux2D

The author used both of mapped mesh (in the teeth) and automatic mesh generators for the other regions. To start with, one must define mesh\_lines from Preflux 8.1 menu and choose the number of divisions in such a way that will be suitable for the corresponding region. The second step is to assign mesh\_lines to the lines of the hard model. For the automatic mesh generator, regions will be subdivided into finite triangular elements automatically keeping the number of divisions on lines the same as they are defined previously. However, for the mapped mesh, all finite elements in a mapped-mesh region are set in rows.

It is impossible to modify any point in the geometry unless the mesh is completely erased. In other words, if we want to modify a point in the hard model, we must select: delete\_mesh then modify that point... then choose Mesh menu to remesh the model again. After modification, the user must define the mesh on lines in a similar manner before deleting the mesh. Otherwise, the modified geometry will have a completely different mesh. For this reason, the author built the hard model and defined the mesh for all lines in the teeth and airgap to have the same mesh once a new geometry is desired.

The elements in the teeth (in shape and number) were kept the same for all positions since it is a mapped-mesh type. For the airgap region, however, meshing a new position will affect slightly on the shape of some elements compared with different position but the number of elements is kept the same. It is important to mention that four rows of triangular elements are placed in the airgap for all lengths.

As an illustration, figure-3.9a and 3.9b show element distribution for two positions as indicated under each figure. The corresponding dimensions of these figures are  $\lambda/g = 40$ ,  $t/\lambda = 0.3$ ,  $X_n = 0$  and at  $X_n = 0.2$ , respectively. As noticed, elements distributions in the teeth are identical. Also, the author made this distribution in such a way that elements become larger in size as we go further away from the airgap region. That is, the vertical sides of a tooth are meshed by elements starting from 0.15 mm in length and

gradually increasing up to 1.12 mm near C-core. Similarly, the tooth is divided into 35 elements horizontally. According to airgap region, if we compare the distributions for both positions in figure-3.9a and 3.9b, we can see that elements are almost kept the same in four rows.

Figure-3.10 shows the elements distribution in the whole study domain for  $\lambda/g = 200$ ,  $t/\lambda = 0.4$ ,  $X_n = 0$ . As seen from the figure, the largest elements have been assigned to region between C-core and the shell which has 68 elements. Actually it is not required to have many elements around C-core since it is defined to have a large permeability. This definition ensures that the leakage flux from C-core can be neglected.

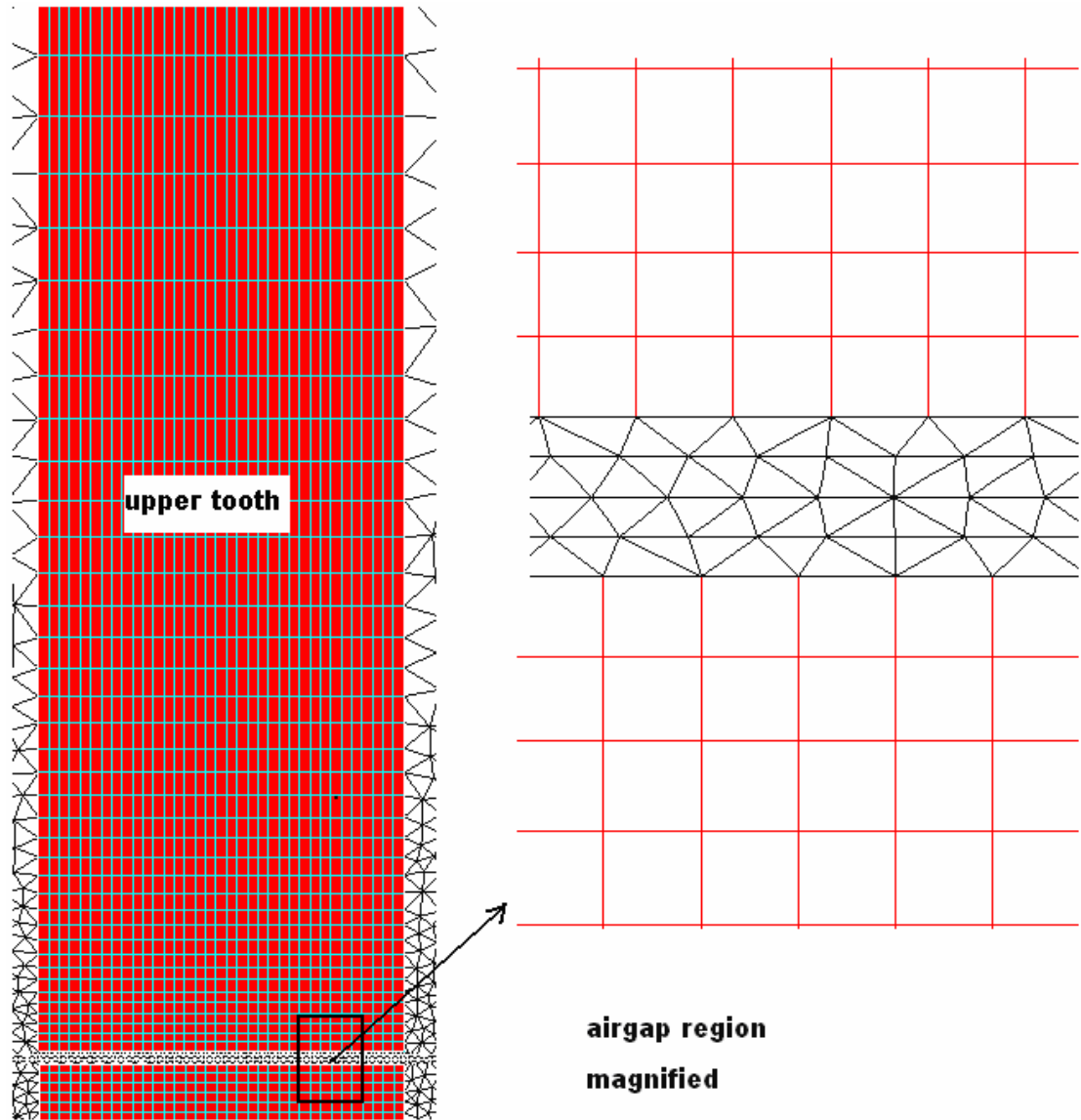


Figure 3. 9 Elements distribution in the middle tooth and in the airgap region( $\lambda/g = 40$ ,  
 $t/\lambda = 0.3$ ,  $X_n = 0$ )



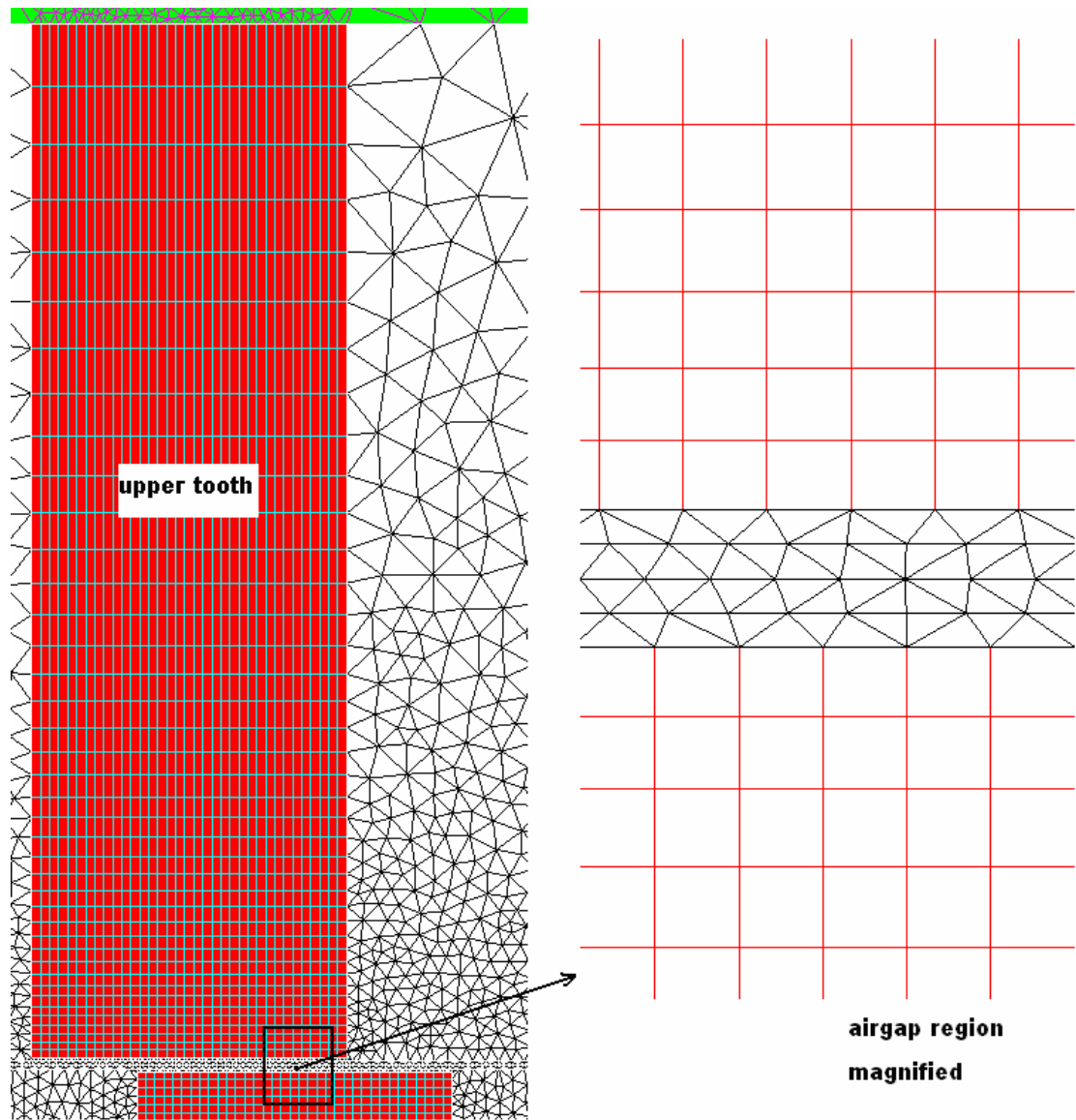


Figure 3. 10 Elements distribution in the middle tooth and in the airgap region( $\lambda/g = 40$ ,  
 $t/\lambda = 0.3$ ,  $X_n = 0.2$ )

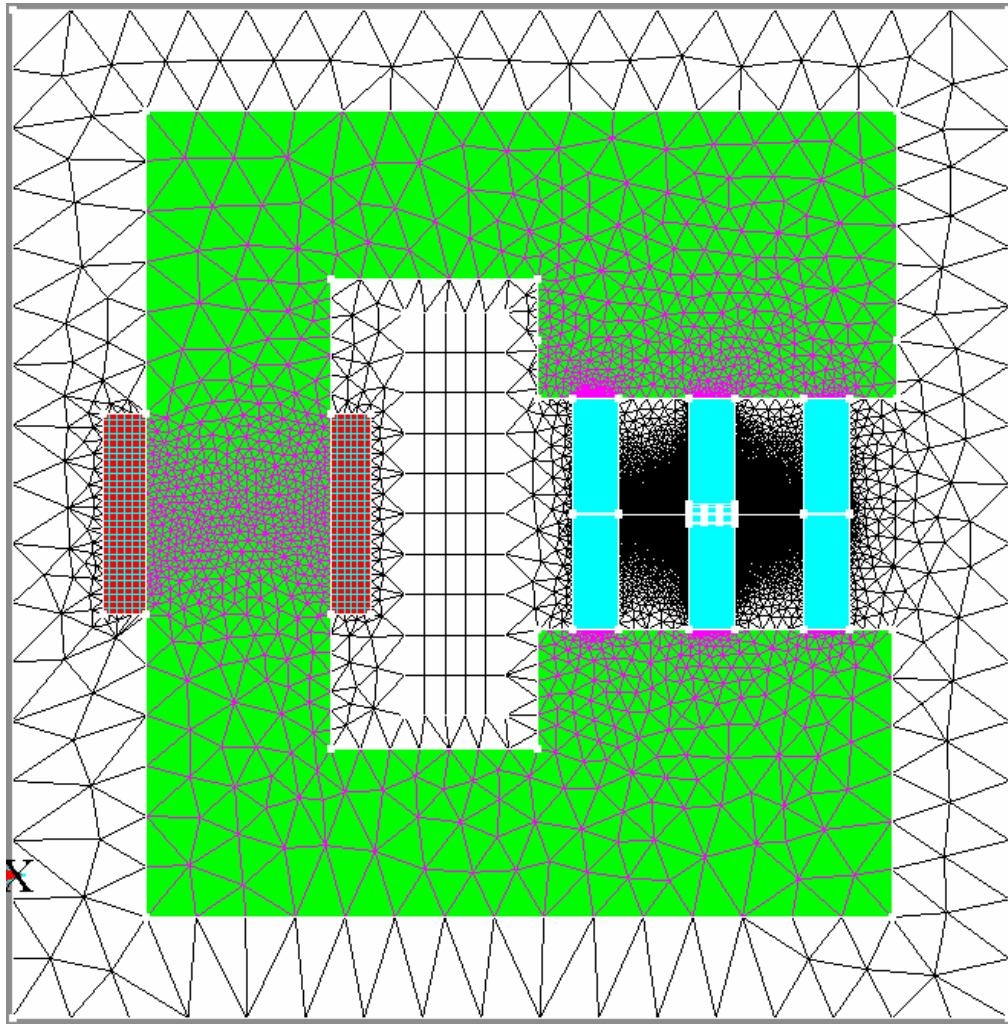


Figure 3. 11 Elements distribution in the study domain( $\lambda/g = 200$ ,  $t/\lambda = 0.4$ ,  $X_n = 0$ )

The following mesh information gives us an idea for the resultant mesh specification:

Number of elements in Vacuum (except vacuum in teeth region) = 520 elements

Number of elements in coil-in and coil-out = 360 elements

Number of elements in one tooth = 1200 elements

Number of the elements in the airgap = 3500 elements

Number of elements in C-core = 2800 elements

For the whole geometry:

Total number of elements = 21,000 elements

Number of elements not evaluated	: 0.0 %
Number of excellent quality elements	: 94.14 %
Number of good quality elements	: 5.3 %
Number of average quality elements	: 0.11 %
Number of poor quality elements	: 0.45 %

This mesh specification is kept the same for all dimensions with a very slight change. Being excellent or good quality elements, the evaluation depends on the angle of the triangular element; if the three angles range within  $60 \pm 5$  degrees, then the element is classified as an excellent quality element. If the angles range within  $60 \pm 10$ , the element is considered to be a good quality element. Finally if the element has an angle of less than 15 degrees, it is considered as a poor quality element. On the other hand, all square elements are considered to be excellent quality elements. According to the mesh reliability, it can be said, by experience, that it is good enough to be considered when solving a problem by a FE software tool. The next step comes after meshing a problem is the definition of the materials that the problem has as a preparation for creating the physical problem.

### **3.4.3 Definition of Materials**

The model has two different materials; one is C-core material which is defined to have a large permeability ( $B / H = 10,000$  Henry/meter). The author assigned this large permeability to the core to avoid the effect of adding the core itself to the basic model. In other words, the MMF drop on the core must be negligible. The second property that the model has is the teeth material which is defined as points on Flux2D (table-3.1) with the resultant BH curve as shown in figure-3.12. This BH-characteristic is taken from ERTAN [11]. Because of nonlinearity in the relation between B and H for teeth material, the problem is classified as nonlinear.

For the empty regions, Flux2D defines air in the problem as vacuum (relative permeability = 1). These three materials are defined in Flux2D\_cslmat module which is easy to use. The material definition must be done before starting the definition of the physical problem.

Table 3. 1 B-H values of the teeth material

<b>POINT</b>	<b>H (A/m)</b>	<b>B (Tesla)</b>	<b>Slope</b>
<b>1</b>	0	0.0	0.005300000
<b>2</b>	200	1.06	0.001100000
<b>3</b>	400	1.28	0.000300000
<b>4</b>	600	1.34	0.000175000
<b>5</b>	1000	1.41	0.000056667
<b>6</b>	4000	1.58	0.000023333
<b>7</b>	10000	1.72	0.000013000
<b>8</b>	20000	1.85	0.000005000
<b>9</b>	30000	1.90	0.000003333
<b>10</b>	60000	2.00	0.000001000

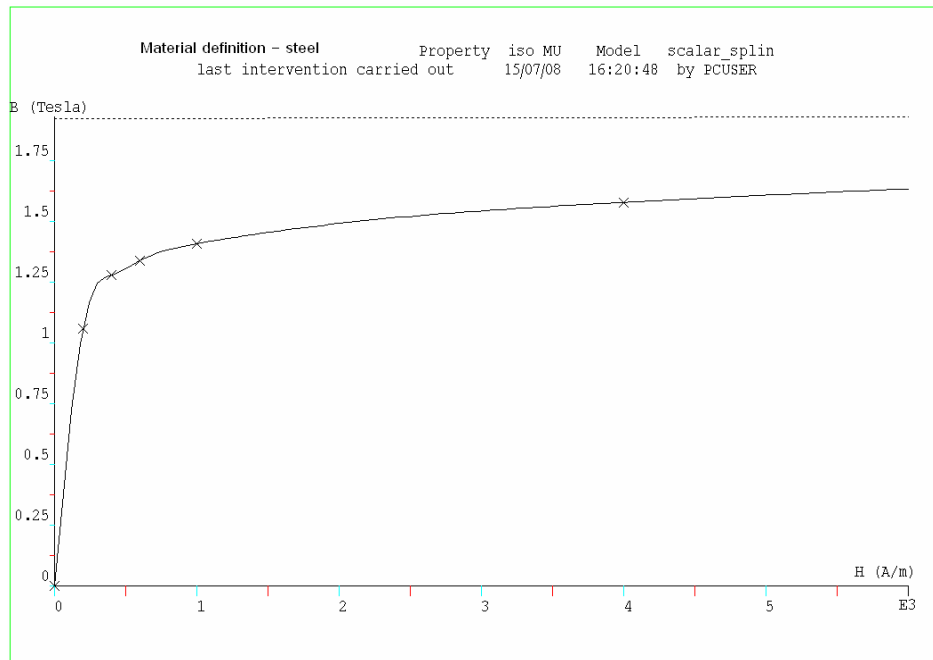


Figure 3. 12 B-H Curve of teeth material

### 3.4.4 Creating the Physical Problem (Prophy in Flux2D)

Prophy allows us to assign a material and a source property to each region of the domain and to set the boundary conditions (figure-3.13). First one has to select the type of domain: axisymmetric or plane (figure-3.14). For plane geometries, we have to enter the thickness of the device. This allows us to calculate quantities on an entire region in the postprocessor. In this work, one has to choose plane type then enter the thickness which is one meter then choose the problem type as magnetostatic. The next step is to assign all regions to the corresponding definitions.

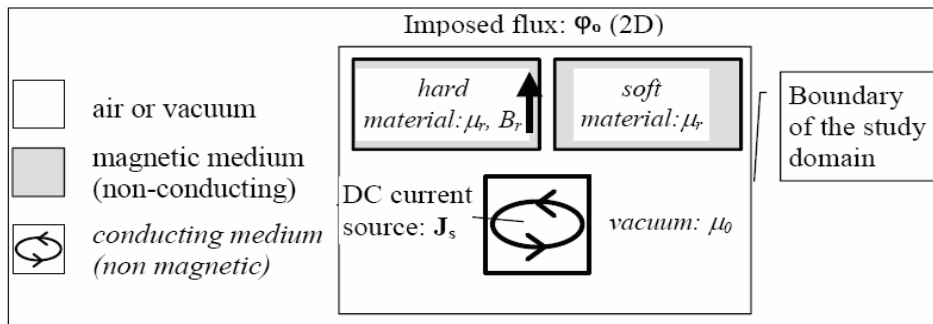


Figure 3. 13 General Diagram of Creating a Physical Problem in Prophy

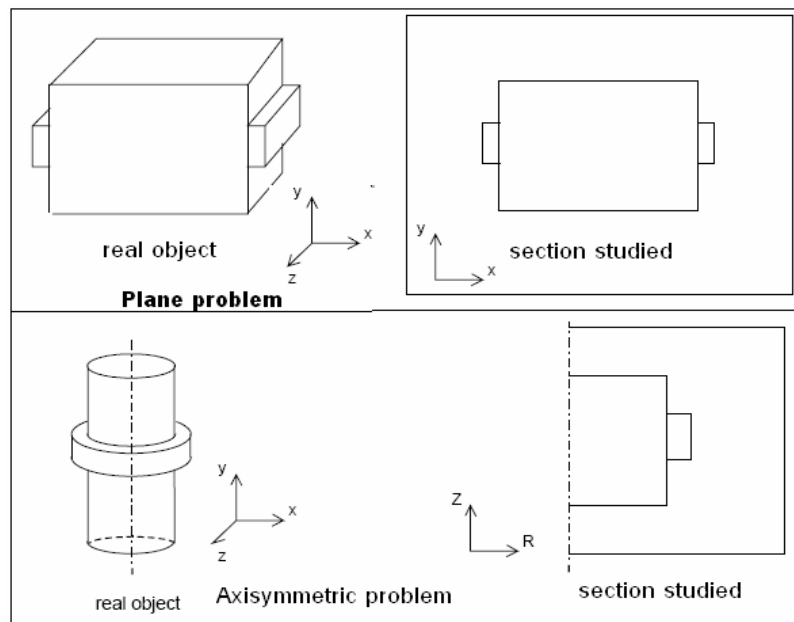


Figure 3. 14 Section Studied in Plane and Axisymmetric Problems

### 3.4.4.1 Definitions of Regions

The model is composed of 10 regions or areas; six teeth, C-core, coil-in, coil-out and the air surrounding these areas as shown in figure-3.15. These regions are meaningless for Flux2D software unless each one is defined to meet the actual model. So for this aim, the following definitions must be assigned to the corresponding regions in Flux2D-Propy:

- Vacuum : defined as Vacuum (relative permeability = 1).
- C-core : Corematerial (permeability = 1000 H/m ).
- Coil-in and Coil-out : constant > current density.
- Teeth : BH-curve (shown in figure-3.12).

Here, according to the coils, one can set the desired Magneto Motive Force (MMF) by one of the following choices offered by Flux2D and no difference in results for which one we choose (regardless of the chosen option, Coil-in must be assigned with a positive value and Coil-out with a negative value).

1. Total Value: assigns current value to the region (equivalent to one turn)
2. Density: assigns amperes/mm<sup>2</sup> to the region.
3. Ampere Turns: assign both of current and number of turns of the coil for the corresponding region from an external circuit

### 3.4.4.2 Boundary Condition

Electric and magnetic fields can be confined or unconfined. For example, a current carrying coil in air has magnetic fields extending to infinity. Surrounding the coil by steel essentially confines magnetic field within the outer boundary of the steel. Thus, in addition to boundary conditions that confine electromagnetic fields within a finite element model, finite boundary conditions are also useful. Usually constraints are needed only on the boundaries of the finite element model, not within it.

However, for 2D problems, it is enough to place a shell far away from the model boundary with a minimum distance of at least 10% of the study domain. In the model described in this work, the shell is far away from the study problem as much as 1.5 times the tooth pitch. By using **Dirichlet condition**, the user can set a value of a variable along external boundary nodes (figure-3.15, where  $A$  is the magnetic vector potential). This condition can be assigned to external and internal shell regions, to internal pinpoint regions and to nodes of the external boundaries.

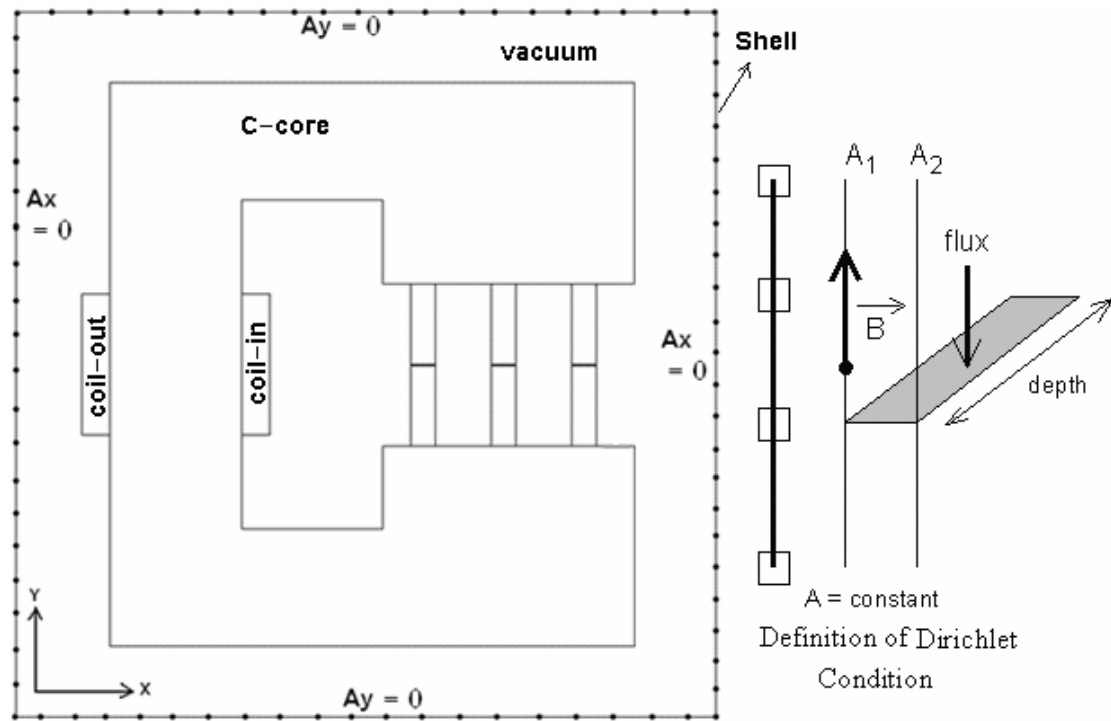


Figure 3. 15 Application of Dirichlet Condition

In this type of boundary condition, the value of  $A$  is explicitly defined on the boundary, e.g. the magnetic vector potential  $A = 0$ . The most common use of Dirichlet-type boundary conditions is to define  $A = 0$  along a boundary to keep flux from crossing the boundary. This implies that no flux exits from the shell.



### 3.4.5 Solving the Problem (SOLVER\_2D)

In order to configure the solving options, one should open SOLVER\_2D and specify the problem, then enter data required for the solution criteria as shown in figure-3.16. Note that the precision is set to **1e-5**. This value is chosen depending on the convergence of results as discussed in section 3.5.2.

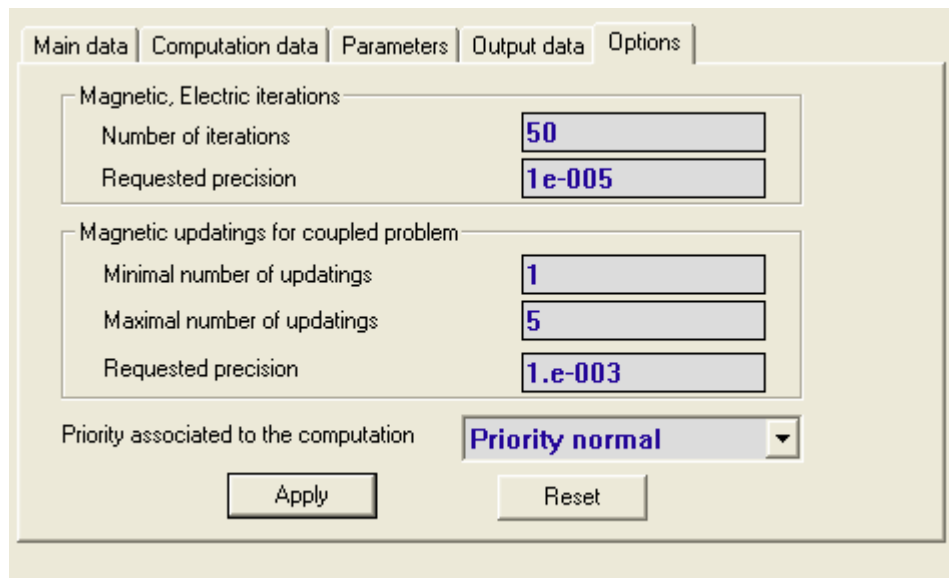


Figure 3. 16 Solver configuration

Then from Computation command the user has to choose Solve icon to run the solving process (figure-3.17).

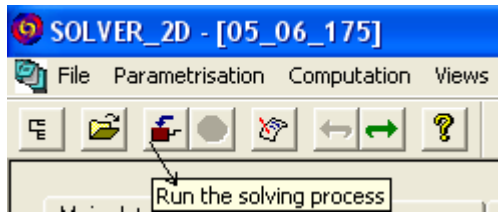


Figure 3. 17 Tool bar of SOLVER\_2D

However, since the author is going to solve the model for several MMF values for each position, there is a possibility to change or modify the MMF value in SOLVER\_2D module before the solution is started.

### 3.5 Model Investigation

Once the model is drawn and meshed, one needs to check out whether it is defined well to meet the actual design. In this work, the author has investigated the model through several ways which are quite enough to be sure about the accuracy of solutions results:

1. Studying the mesh.
2. Solution Criteria.
3. MMF Drop.
4. Contour Plots of Potential.
5. Using Another FEA-based Software.

#### 3.5.1 Studying the Mesh

The mesh described in section 3.4.2.2 is applied for all solutions in this work. However, the author needs to study the effect of changing the specification of this mesh. In other words, it is important to check out how much change obtained in the results if the model is meshed finer or coarser than that described previously. But as mentioned before, solution time is highly dependent of number of nodes used to mesh the model. This

means that the finer the mesh is, the longer time of solution the computer will have. So to compromise between the mesh and the time of solution, a specific parameter has to be studied while changing mesh specification.

For the aim of mesh investigation, the tangential force acting on the tooth is taken into account. In addition, to study the effect of mesh only, solution criteria are kept the same as shown in figure-3.16. In that figure, the requested precision is set as  $1e-5$ . Also a specific normalized position is chosen with the following parameters:

$$\lambda/g = 70$$

$$t/\lambda = 0.3$$

$$X_n = 0.2$$

$$N \cdot I = 707 \text{ Amp.turn}$$

where:

$\lambda$  is the tooth pitch,

$g$  is the airgap length,

$t$  is the tooth width,

$X_n$  is normalized position,

$N$  is number of coil turns, and

$I$  is the current in the coil.

The total number of nodes described in section 3.4.2.2 is 20,029 (for teeth and airgap only). The author changed the number of elements, which describes the mesh of the model, in the teeth and airgap only. Five different cases of mesh formation have been studied. Table-3.2 and figure-3.18 summarize the results obtained together with time of solution required to solve each case.

Table 3. 2 Mesh effect on Tangential force.

<b>Number of Mesh Specification</b>	1	2	3	4	5
<b>Number of Elements in One Tooth</b>	400	600	800	1200	1600
<b>Number of Elements in the Airgap</b>	1100	1800	2400	3500	4600
<b>Tangential Force</b>	383.1	415.7	435.5	440.0	440.04
<b>Time of Solution(in sec)</b>	21	38	55	83	118

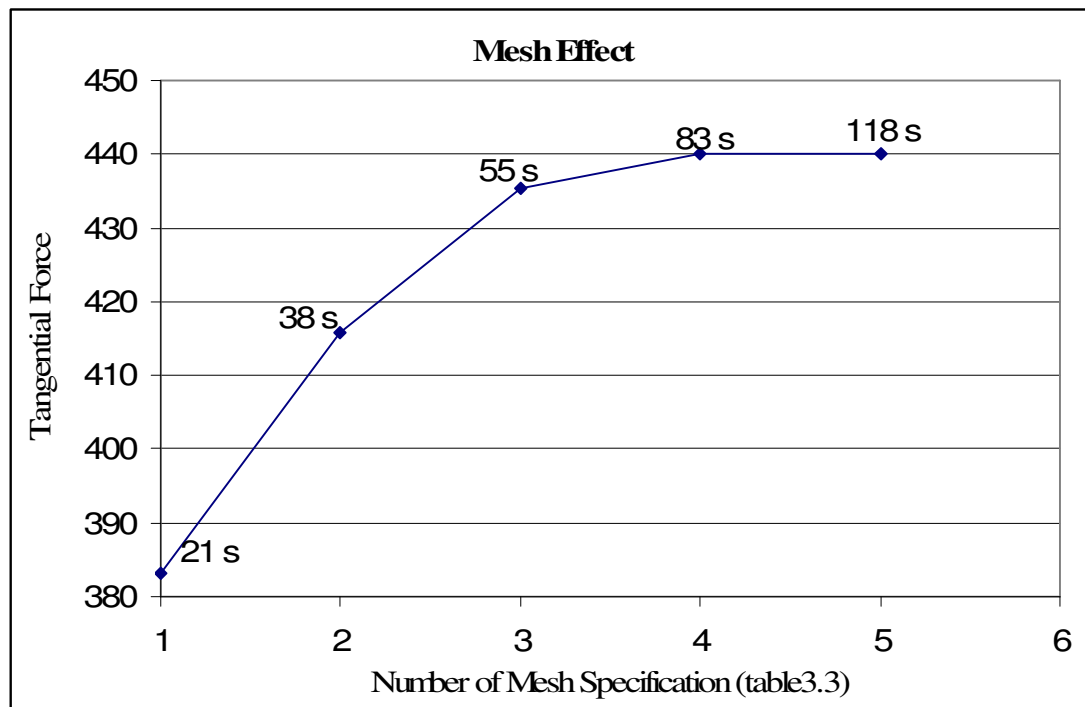


Figure 3. 18 Tangential force vs. Number of nodes in teeth and airgap

As shown in table-3.3, tangential force converges to 440 Newtons and this value is obtained when a tooth has 1200 elements and the airgap region has 3500 elements. The corresponding time of solution is 83 seconds which is much less than that for case number 5. Thus, case number four comes to be a reasonable choice for meshing the model.

### 3.5.2 Solution Criteria

In this section, solution accuracy has been investigated. As shown in figure-3.16, SOLVER\_2d offers two options for solution criterion; number of iterations and requested precision or accuracy. This means the solution is stopped either the number of iterations is reached or the requested precision is accomplished. The author focused on the requested precision because it is the advised criterion that should be chosen. However, one should put a limit for the maximum number of iterations since sometimes the solution falls into a loop because it can't reach the requested precision. This limit of the maximum number of iteration, on the other hand, mustn't affect on the precision. So, a relatively high number should be used and is chosen as 50 iterations in this work.

Again, for the aim of accuracy investigation, the tangential force acting on the tooth is taken into account. In addition, to study the affect of accuracy only, mesh specification is chosen as the result of section 3.5.1; the total number of elements in airgap is 3500. The problem is studied for the following parameters:

$$\lambda/g = 70$$

$$t/\lambda = 0.3$$

$$X_n = 0.2$$

$$N*I = 707 \text{ Amp.turn}$$

From table-3.3, it is clear that tangential force converges to 440.0 Newtons at a precision of  $1e-5$ . Also at that precision, the time of solution is 83 seconds. If one tries to decrease the precision even less than  $1e-5$ , there will be no any improvement in convergence of the tangential force anymore but time of solution is increased. Figure-3.19 shows the variation of tangential force as the precision decreases.

Table 3. 3 Precision (Accuracy) Effect on Tangential Force.

Requested Precision	1e-3	1e-4	1e-5	1e-6
Tangential Force	437.2	439.5	440.0	440.0
Time of Solution(in sec)	67	72	83	87

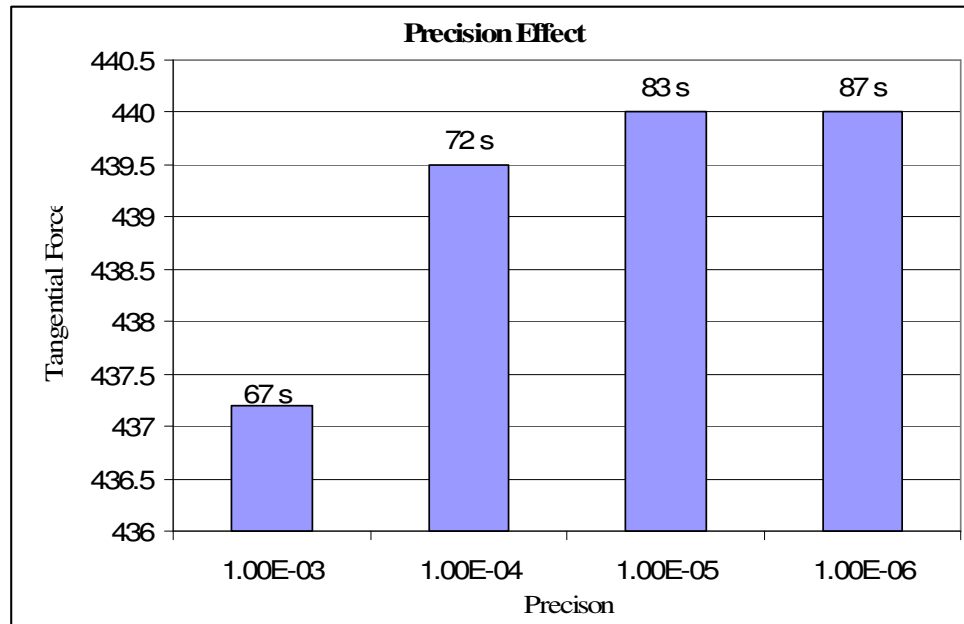


Figure 3. 19 Tangential force vs. Precision (Accuracy)

### 3.5.3 MMF Drop

Another step according to model investigation is measuring the resulting MMF drop on the core which is defined to have a large permeability. It is assumed that this MMF drop must be small as much as possible so as not to affect on the model. That is; since the author is trying to build a FEA-compatible model and equivalent to that of Ertan [11], N\*I input data must be defined the same as described by Ertan.

MMF drop investigation can be performed in two steps; the first one is to compute MMF drop on C-core, and the second step is to compute the drop on the teeth and the airgap together. For this aim, Flux2D offers the user to plot a path and obtain the values of field intensity on that path.

For  $\lambda/g = 70$ ,  $t/\lambda = 0.3$ ,  $X_n = 0.0$ (IN-position),  $N \cdot I = 220$  Amp.turn and accuracy of  $1e-5$  with 20,000 nodes in the teeth and the airgap, two paths are drawn in C-core, a third path is drawn in middle of the second group of teeth and a fourth one is drawn between the second and third groups as shown in figure-3.20.

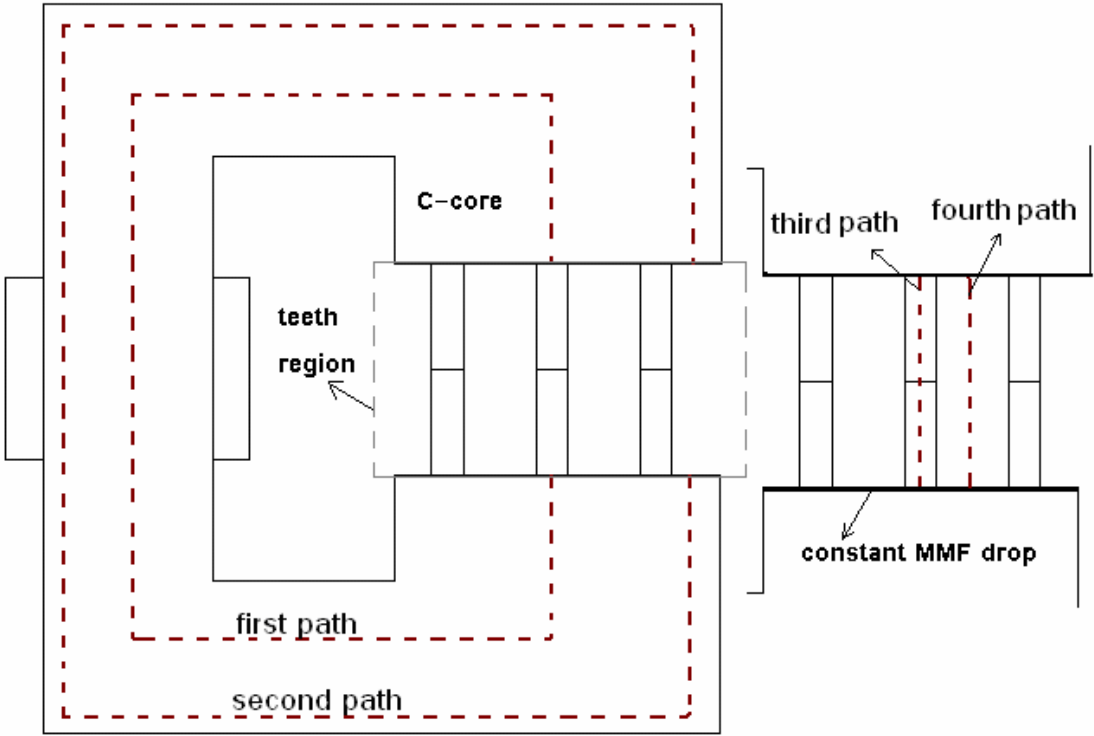


Figure 3. 20 Places of drawn path for  $\lambda/g = 70$ ,  $t/\lambda = 0.3$ ,  $X_n = 0.0$ .

Each path is discretized into 1000 segments. For each segment, Flux2D writes the field intensity magnitude. Then by using equation 3.1 in an excel sheet, the MMF drop on each path can be found. Table-3.4 shows the MMF drop on each path.

$$MMF\_drop = \sum_{i=1}^{1000} H_i \cdot \Delta l \quad (\text{in Amp.turn}) \quad (3.1)$$

Where:

$H_i$  is the field intensity,

$\Delta l$  is path length divided by 1000.

Table 3. 4 MMF drop results.

<b>Path</b>	<b>MMF drop (A.t)</b>
<b>First Path</b>	0.235
<b>Second Path</b>	0.246
<b>Third Path</b>	219.72
<b>Fourth Path</b>	219.75

As seen from table-3.4, it is obvious that MMF drop on C-core can be neglected. Moreover, if the drop on C-core is added to the drop on a path in the teeth region, the results comes to be very close to 220 A.t. which is already have been assigned to the coil as defined at the beginning of this section. As a conclusion, adding a core with a large permeability to the model will not affect on the MMF drop, thus on the results.

### **3.5.4 Contour Plots of Potential**

The best way to quickly understand and to check the reliability of the results of finite element analysis is to obtain a contour of the calculated potential. The contour plot shows, first, whether the desired boundary conditions have been properly applied or not. For example, if many contour lines go to a boundary, then that boundary has not been constrained to zero. In the case of two-dimensional magnetic field problems, the density



of  $A$  contours is proportional to flux density  $B$ . the direction of the lines is the direction of  $B$ . Thus the contour plot is a flux plot that tells the designer, for example, where steel should be added to avoid saturation and where it can be removed to save cost and space.

So for the model described in this work, contour of potential is plotted on figure-3.21. This figure corresponds to  $\lambda/g = 70$ ,  $t/\lambda = 0.3$ ,  $X_n = 0.2$  and  $MMF = 707$  A.t. Figure-3.22 shows the contour plot in the teeth region for the same dimension and data.

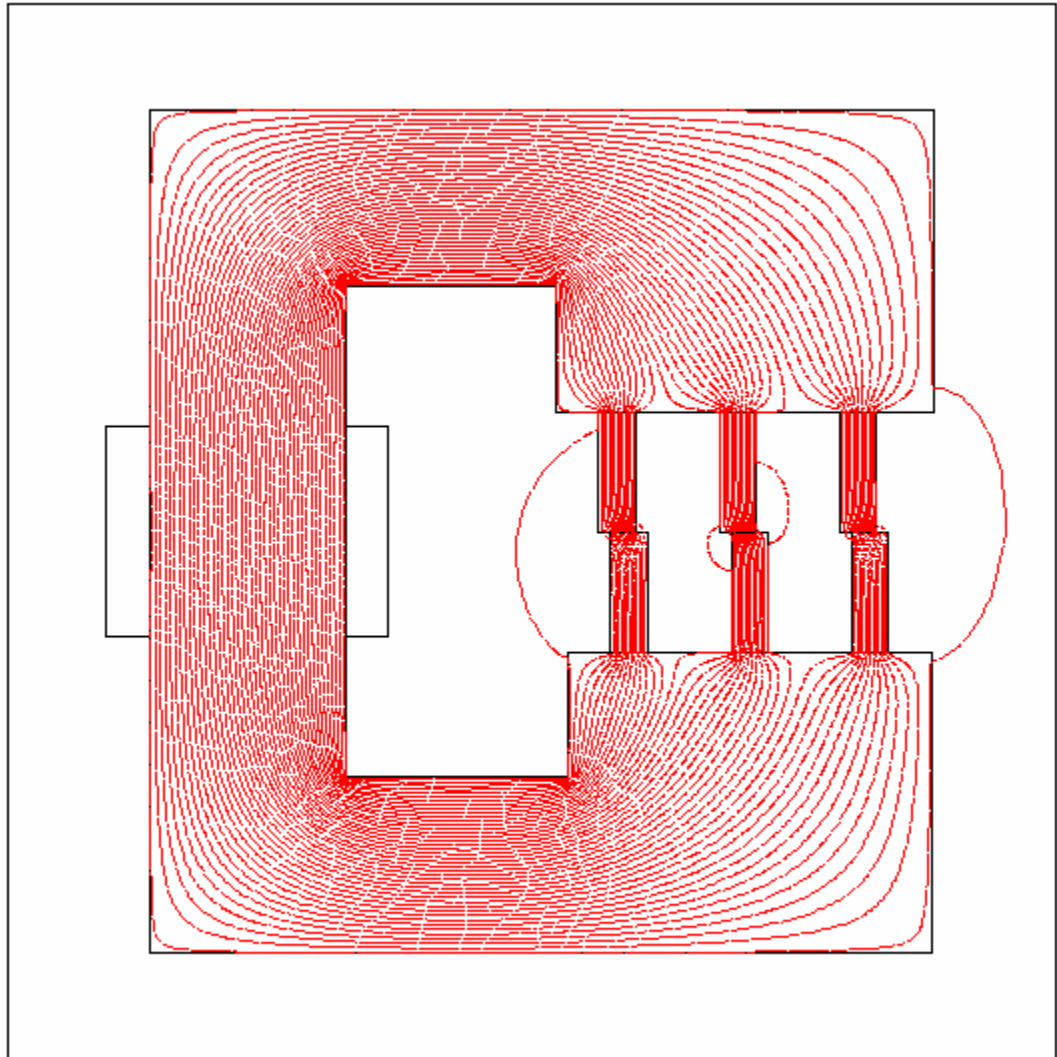


Figure 3. 21Contour Plot for  $\lambda/g = 70$ ,  $t/\lambda = 0.3$ ,  $X_n = 0.2$  and  $MMF = 707 \text{ A.t}$

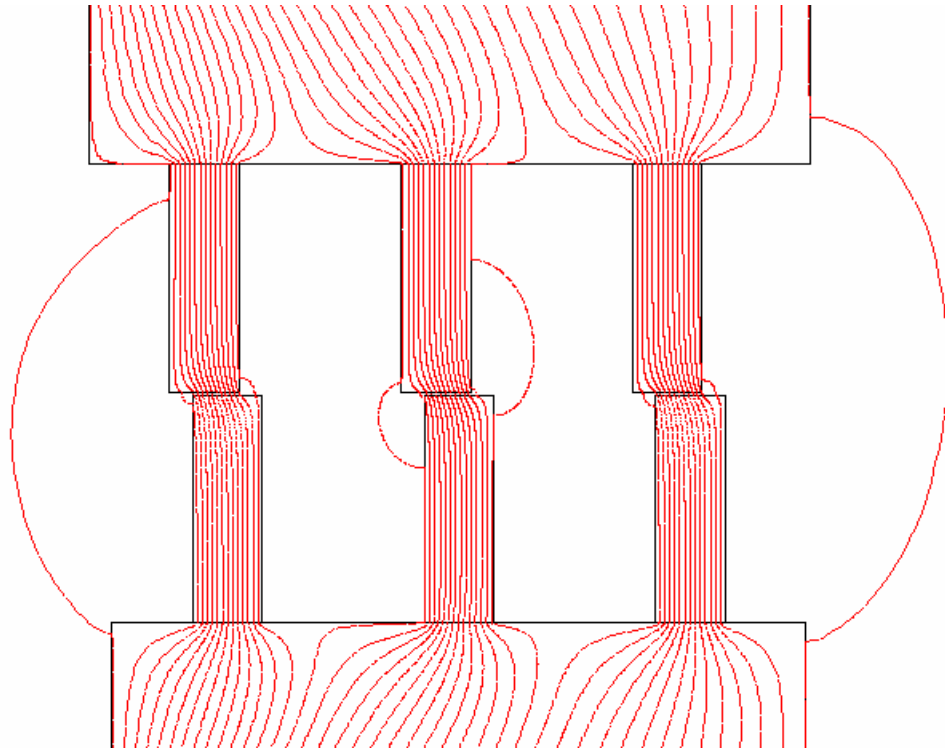


Figure 3. 22 Contour Plot in teeth region for  $\lambda/g = 70$ ,  $t/\lambda = 0.3$ ,  $X_n = 0.2$  and  $MMF = 220 \text{ A.t}$

### 3.5.5 Using Another FEA-based Software (ANSYS):

The last point remaining for the aim of model investigation is to use another FEA-based software. ANSYS 11.0 is used for this purpose. Definition of the model in ANSYS is quite similar to that for FLUX2D. However, obtaining the same mesh 'exactly' in both of these programs is nearly impossible. But the most important thing is to mesh the airgap region in such a way that the number of nodes in this region must be the same as the case in Flux2D. The same boundary condition is also applied, the accuracy as well.

Four cases with different geometries were chosen to solve in ANSYS as shown in table-3.5 where the percentage error is defined as:

$$ERR\% = \frac{Ft_{FLUX2D} - Ft_{ANSYS}}{Ft_{FLUX2D}} * 100\% \quad (3.2)$$

Table 3. 5 Comparison between ANSYS 11.0 & FLUX2D.

<b>Input parameters</b>	$Ft_{FLUX2D}$	$Ft_{ANSYS}$	$ERR\%$
$\lambda/g = 70, t/\lambda = 0.3, X_n = 0.2, MMF = 220$	105.40	104.50	+0.86
$\lambda/g = 70, t/\lambda = 0.4, X_n = 0.2, MMF = 470$	295.70	293.12	+0.87
$\lambda/g = 40, t/\lambda = 0.4, X_n = 0.4, MMF = 825$	680.1	683.23	-0.46
$\lambda/g = 40, t/\lambda = 0.5, X_n = 0.4, MMF = 481$	272.5	268.51	+1.10

The results of tangential force acting on the middle tooth ensure that data obtained by Flux2D is quite accurate. As seen from table-3.5, the percentage error between ANSYS and FLUX2D is low and it can be acceptable.

In section 3.5, there is no explanation for how the author obtained tangential force. In addition, this model is built and investigated to obtain the normalized data. So, in the following section (3.6), the author discusses how he obtained tooth flux density, normalized permeance, tangential force, and normal force from the field solution. The corresponding computations for the switch reluctance motors that will be studied in chapter four are also included in section 3.6.

### 3.6 Computations

In this section and before introducing the table of normalized data, computations of tooth flux density, normalized permeance, static torque, flux linkage, and both tangential force and normal force are clarified. Since the author has solved the model by using finite element method, he has to show how these computations can be obtained from a FEA tool.

#### 3.6.1 Tooth Flux Density.

To obtain tooth flux density, a horizontal path must be drawn with a length of tooth pitch. Figure-3.23 shows both the definition of the tooth pitch and where the path has to be drawn. The path must be extended from the center of the first slot to the center of the second slot in the model as much as tooth pitch. Basically, the path can be placed anywhere in terms of the depth. However, the author chose to place the path at a depth of  $0.2d$  from the tooth tip since there are quite many elements around that region. In other words, placing a path at a higher depth can have less accurate results, but not much even the difference can be neglected. On the other hand, to consider unaligned positions, the author didn't choose to place the path even closer to the airgap region where the field intensity changes rapidly.

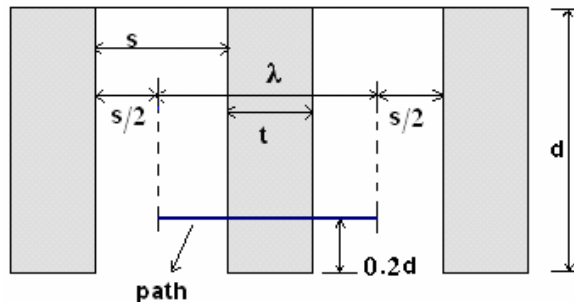


Figure 3. 23 Tooth pitch definsion

The path is discretized into 1000 points. From Flux2D- PostPro, the user can get the magnitude of flux density (in Tesla) versus the length of the path. As an example, figure-3.24 shows the magnitude of flux density along the path drawn across the tooth for  $\lambda/g = 70$ ,  $t/\lambda = 0.5$ ,  $X_n = 0$  and  $MMF = 470$ , and figure-3.25 at  $\lambda/g = 70$ ,  $t/\lambda = 0.5$ ,  $X_n = 0.8$ ,  $MMF = 470$ . In these two figures, the path was drawn at a height of  $0.2*d$  from tooth tip where  $d$  stands for the tooth depth.

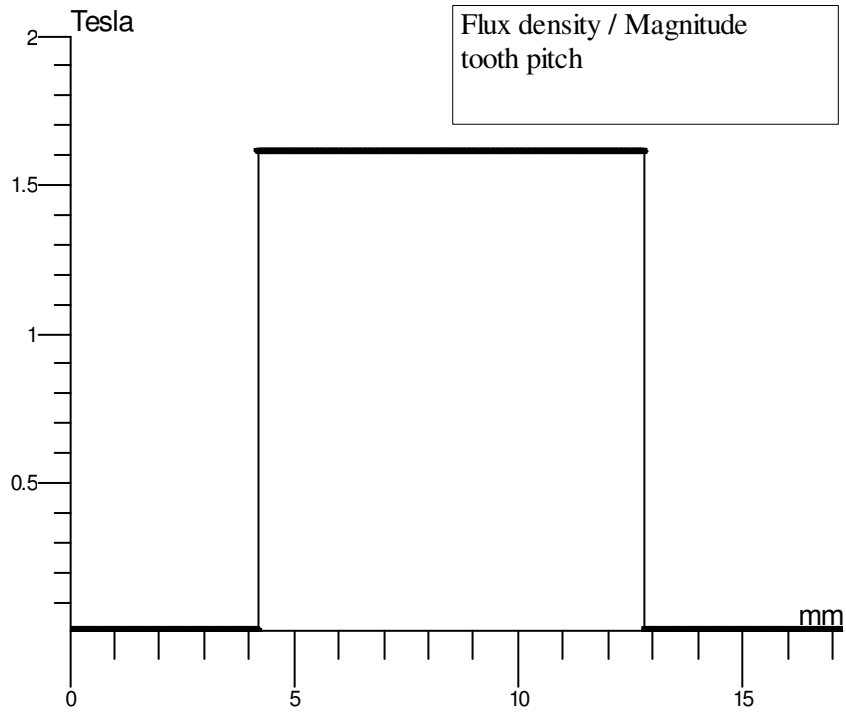


Figure 3. 24 Magnitude of flux density for ( $\lambda/g = 70$ ,  $t/\lambda = 0.5$ ,  $X_n = 0$ ,  $MMF = 470$ )

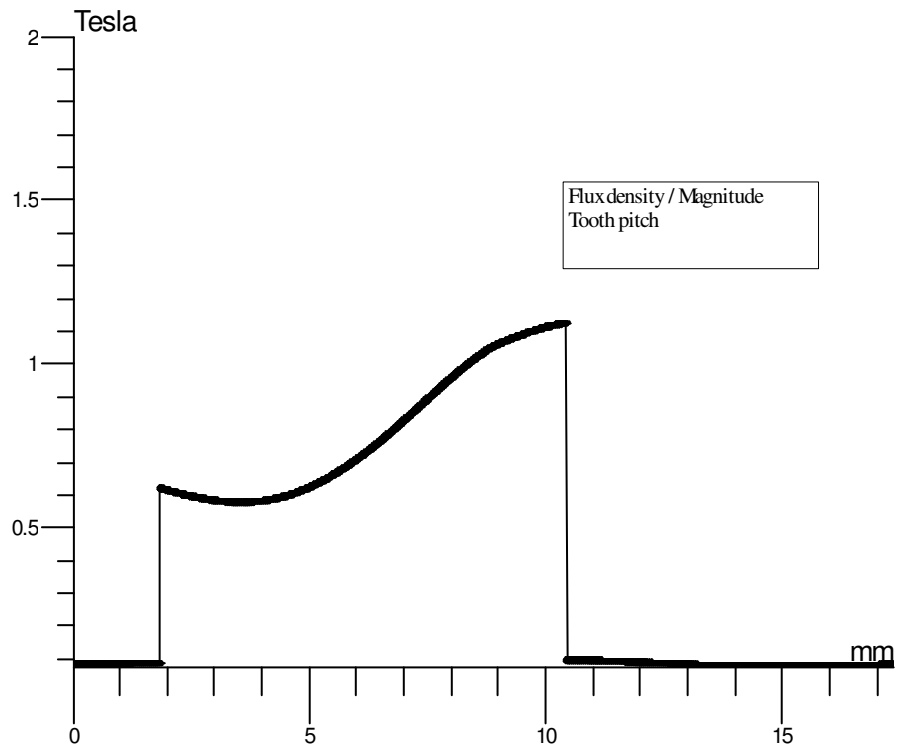


Figure 3. 25 Magnitude of flux density for ( $\lambda/g = 70$ ,  $t/\lambda = 0.5$ ,  $X_n = 0.8$ ,  $MMF = 470$ )

Then from the property of the curve, one can get its integral. However, the integral of flux density magnitude along the path is independent of the place of the path; i.e. the same integral one can get either the path is close to tooth tip or far away from the tip. Once the integral is obtained, equation 3.3 must be used:

$$B_t = \frac{\int_0^l B_i . dl}{t} \quad (3.3)$$

where:

$B_i$  is flux density magnitude at point  $i$  on the path

$B_t$  is the tooth flux density

$t$  is tooth width

$l$  is the length of the path (17.2mm)

This procedure is applied for all solutions to calculate tooth flux density,  $B_t$ . It is worth mentioning that, by using Flux2D- PostPro which is based on finite element method, one can check color shade results everywhere and in details. Actually this a very great advantage to design process since the designer can check the magnetic behavior in the problem. As seen from figure-3.26 which shows color shade results for  $\lambda/g = 70$ ,  $t/\lambda = 0.5$ ,  $X_n = 0.8$ , and  $MMF = 470$ , the white regions in teeth corners have the maximum value of flux density for that position and excitation. Figure-3.27 shows the colors corresponding to flux density intervals. Figure-3.28 is the same as figure-3.26 but for better view in mid-teeth tips.

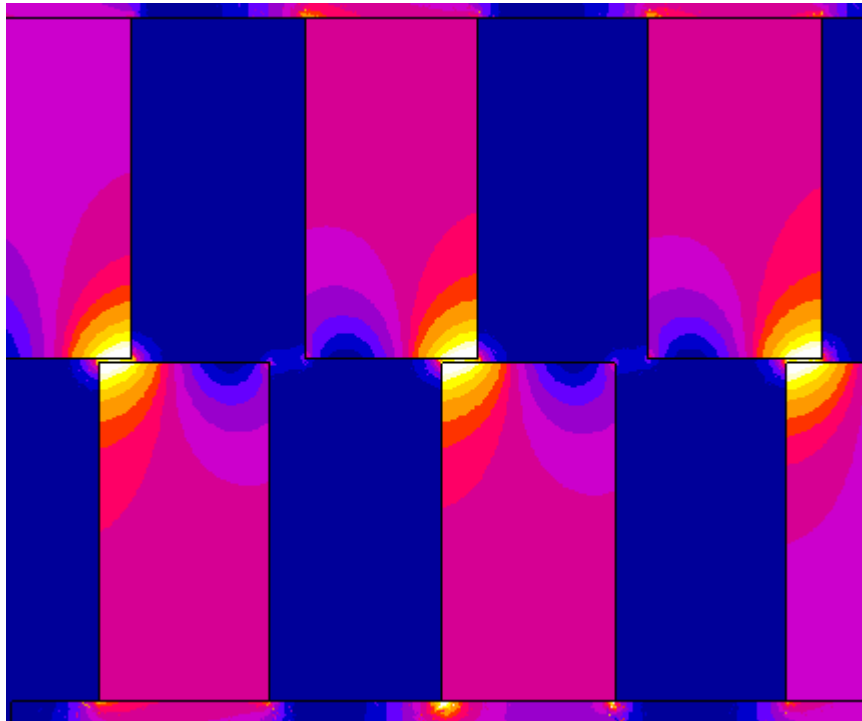


Figure 3. 26 Color shade results for  $\lambda /g = 70$ ,  $t/\lambda = 0.5$ ,  $X_n = 0.8$ ,  $MMF = 470$



## Color Shade Results

Quantity : |Flux density| Tesla

Scale / Color

10.0459E-9 / 0.125

0.125 / 0.25

0.25 / 0.375

0.375 / 0.5

0.5 / 0.625

0.625 / 0.75

0.75 / 0.875

0.875 / 1

1 / 1.125

1.125 / 1.25

1.25 / 1.375

1.375 / 1.5

1.5 / 1.625

1.625 / 1.75

1.75 / 1.875

1.875 / 2



Figure 3. 27 Color shade definition

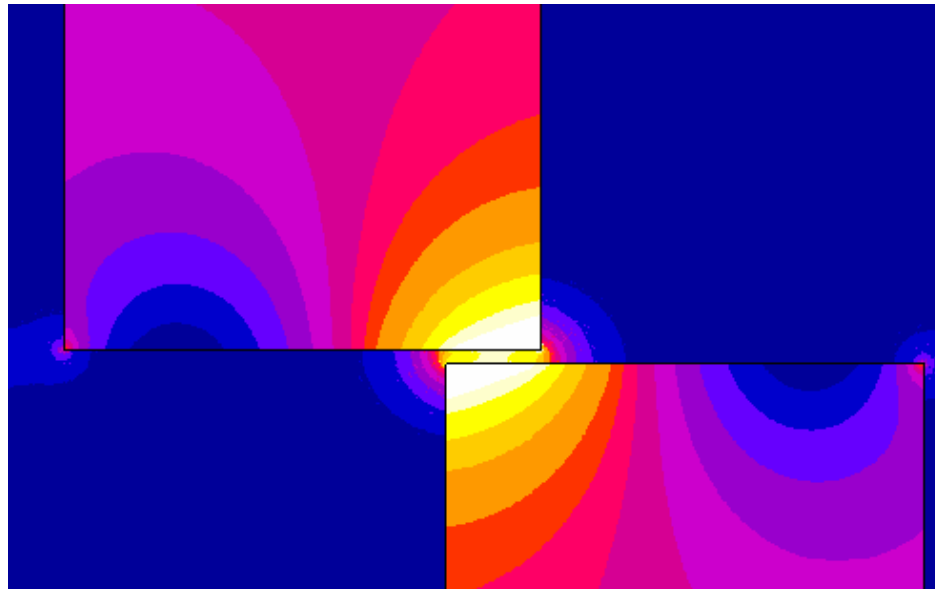


Figure 3. 28 Color shade for  $\lambda/g = 70$ ,  $t/\lambda = 0.5$ ,  $X_n = 0.8$ ,  $MMF = 470$ (Magnified)

### 3.6.2 Permeance Computations

Normalized permeance can be computed by the following equation:

$$P_n = \frac{P_x}{P_{base}} \quad (3.4)$$

where  $P_x$  and  $P_{base}$  are given by equation 3.5 and 3.6 respectively:

$$P_x = \frac{\phi_\lambda}{N * I} \quad (3.5)$$

$$P_{base} = \frac{\mu_0 * \lambda * L_c}{g} \quad (3.6)$$

where:

$\phi_\lambda$  is the flux in wb over the tooth pitch,  $\lambda$

$N * I$  is ampere turns of the coil ( $MMF$ )

$\mu_0$  is air permeability ( $4\pi * 10^{-7} H / m$ )

$L_c$  is the stack length, and is taken as 1 meter.

Substituting equations 3.5 and 3.6 into 3.4, equation 3.4 becomes:

$$P_n = \frac{\phi_\lambda}{(N * I)\mu_0} * \frac{1}{\lambda / g} \quad (3.7)$$

Since all geometries are expressed in terms of the coefficient  $\frac{\lambda}{g}$ , it is better to express

normalized permeance in terms of this coefficient.

To compute normalized permeance by equation 3.7, three parameters are needed;

- $\frac{\lambda}{g}$  which has six different values: 40, 70, 100, 150, 200, and 250.
- $(N * I)$  is the excitation level of the coil.
- $\phi_\lambda$  is the integration of flux density magnitude along the path which is clarified in section 3.6.1 for the aim of tooth flux density computation. Since the stack length is one meter,  $\phi_\lambda$  can be expressed by:

$$\phi_\lambda = L_c * \int_0^l B_i .dl = \int_0^l B_i .dl \quad (3.8)$$

### 3.6.3 Force Computations

In chapter two (section 2.11), the equations of Virtual Works Method and Maxwell stress tensor method have been introduced. However, these methods are applied by ANSYS and FLUX2D if the user wants to depend on force results obtained automatically by these softwares. But in this model, the results that ANSYS and FLUX2D compute, are not accurate because of the following two points:

- Virtual Works Method assumes that the part for which the force or torque is to be calculated is totally surrounded by air. This condition is not applied since the tooth is attached by the core from the back side.
- Maxwell stress tensor method is only valid when the permeability of the region is high compared to that of neighboring regions (1/1000). Thus, the problem here is that the permeability of C-core is higher than the permeability of the tooth itself, hence this method is also not applicable.

So for these reasons, the author must plot paths around the tooth where the force has to be computed. And the theory behind this is as follows:

The force on an iron body enclosed in a surface S can be calculated from Helmholtz equation. Before Helmholtz, Maxwell derived a formula giving force for a similar situation. The formula is widely used and known as Maxwell Stress Method. Both Maxwell and Helmholtz equations can be used. However, the author used Helmholtz equations. In air, these equations are expressed as follows: (giving force on a surface element  $ds$ )

$$F_t = \mu_0 H_n H_t \quad (3.9)$$

$$F_n = 0.5 * \mu_0 (H_n^2 - H_t^2) \quad (3.10)$$

where:

$F$  is the force

“ $n$ ” means perpendicular to the surface of integration

“ $t$ ” stands for the tangential direction to the surface

$H$ : field intensity.

However, the author has to rewrite equations 3.9 and 3.10 in a form suitable to the FEA software;

$$F_t = \Delta l * \sum_{i=1}^m \mu_0 H_{n,i} H_{t,i} \quad (3.11)$$

$$F_n = \Delta l * \sum_{i=1}^m 0.5 * \mu_0 (H_{n,i}^2 - H_{t,i}^2) \quad (3.12)$$

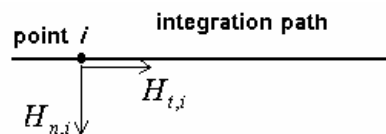


Figure 3. 29 Field intensity components at a point in an integration path

where:

$F_t$  is the tangential force in parallel with the path

$\Delta l$  is path segment (distance between two successive points)

$m$  is the discretization number (1000 points)

$H_{n,i}$  is the  $i^{\text{th}}$  normal component of field intensity (normal to the path)

$H_{t,i}$  is the  $i^{\text{th}}$  tangential component of field intensity (tangential to the path)

$F_n$  is the normal force (normal to the path)

To perform these computations, three paths must be drawn around the tooth where the force has to be computed. That is, the first path is in the middle of the left slot as shown in figure-3.30, this path is placed between the points **a** and **b**. The second path is placed in the middle of the airgap between **b** and **c**. And the third path, **cd**, is placed in the center of the right slot. Referring to equations 3.11 and 3.12, force components  $F_t$  and  $F_n$  are indicated for each path in the figure. As mentioned before, being tangential or normal component is referred to the path itself.

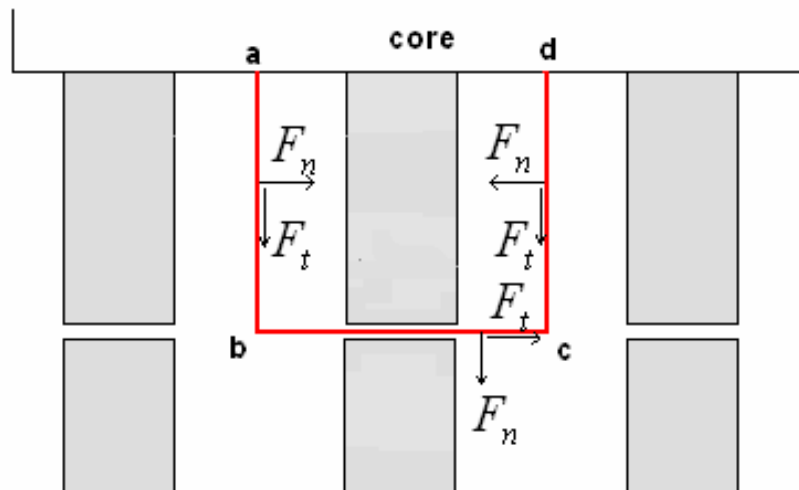


Figure 3. 30 Paths of Stress Integration taken for a tooth pitch

Each path is discretized into 1000 points to obtain accurate results. Once the paths are defined, one can extract the values of normal and tangential components of the field intensity for each point from FLUX2D. Figure-3.31 and figure-3.32 show, respectively, the values of normal components and tangential components of the field intensity for the second path, **bc**, at MMF = 707 A.t,  $\lambda/g = 70$ ,  $t/\lambda = 0.5$ , and  $X_n = 0.4$ .

For each solution, these three paths are drawn and the corresponding field intensity components are obtained. Then the total tangential and normal force components acting on the tooth are computed by equations 3.13 and 3.14 respectively.

$$F_{t-total} = F_{n-ab} - F_{n-cd} + F_{t-bc} \quad (3.13)$$

$$F_{n-total} = F_{t-ab} + F_{n-bc} + F_{t-cd} \quad (3.14)$$

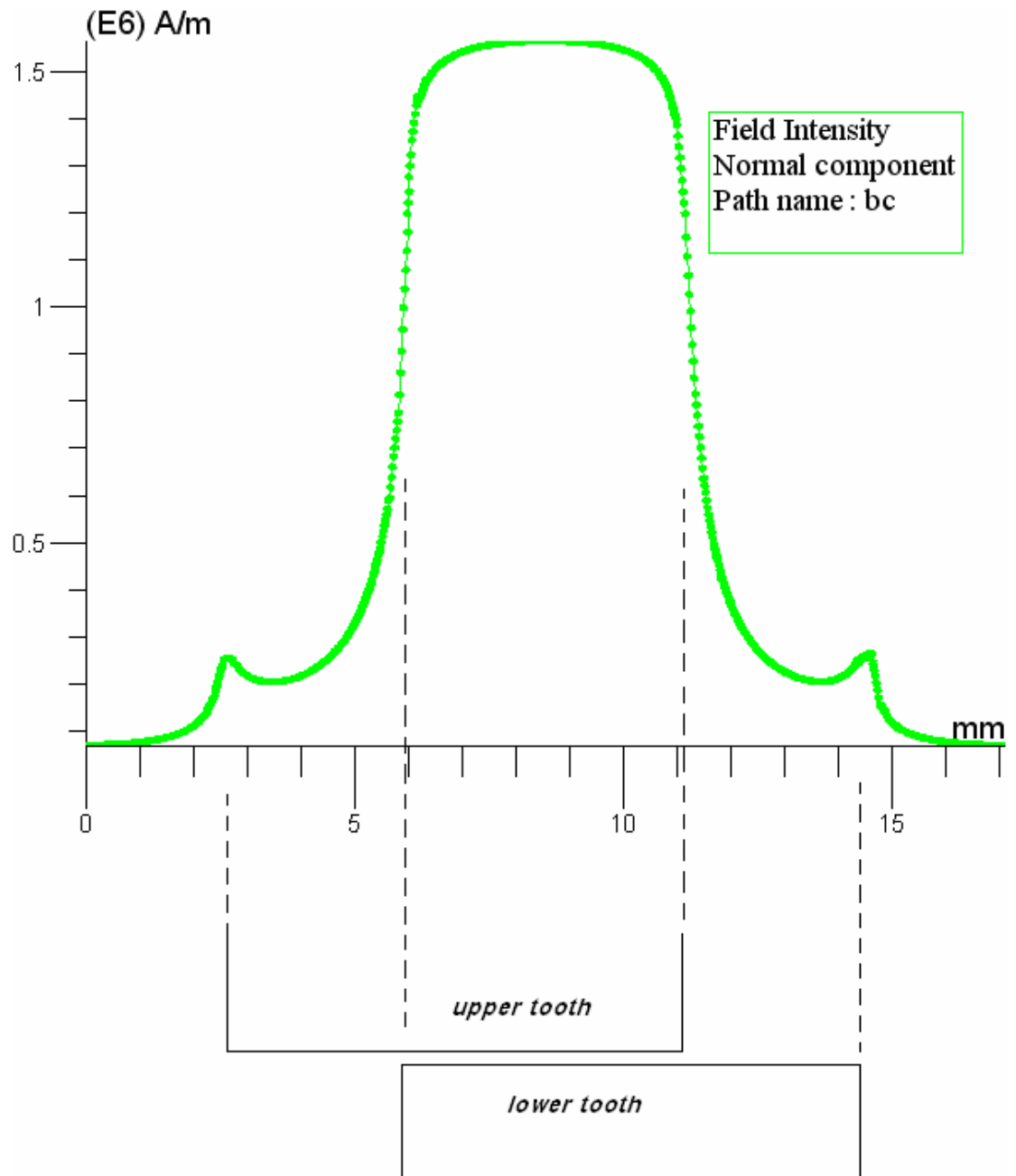


Figure 3. 31 Normal field intensity component of the path bc at MMF = 707 A.t,  $\lambda/g = 70$ ,  $t/\lambda = 0.5$ , and  $X_n = 0.4$

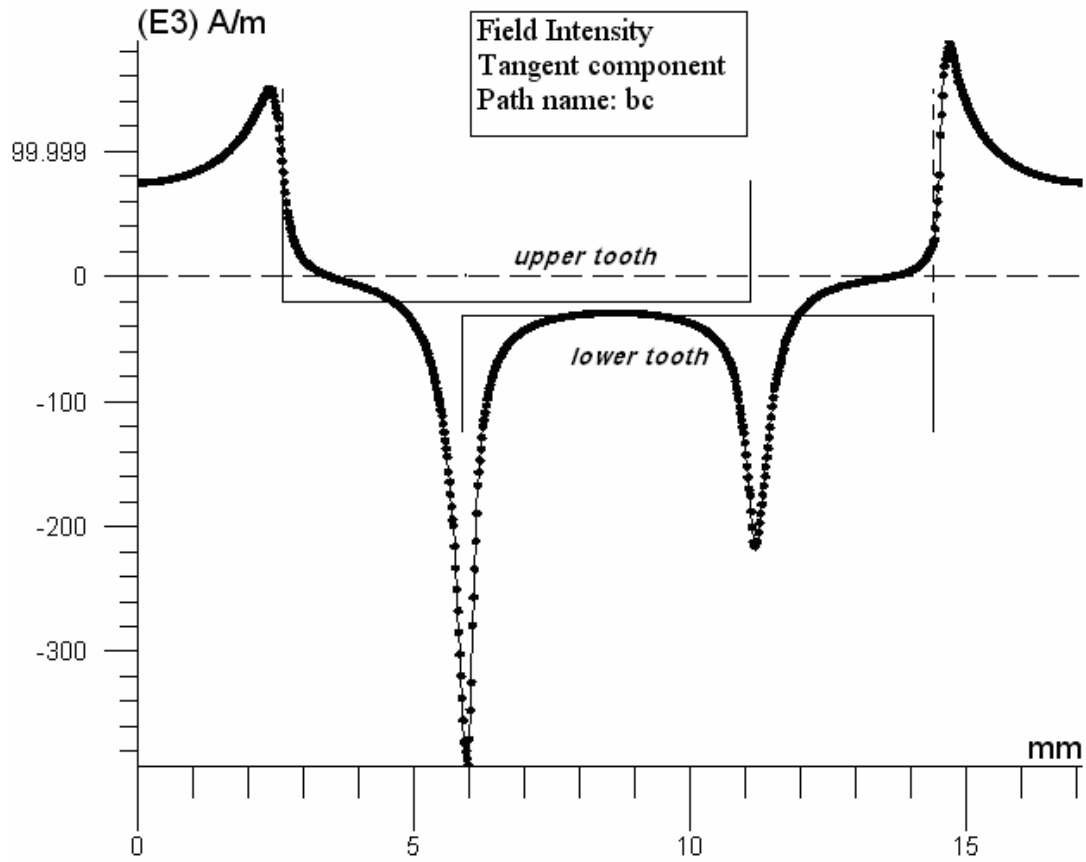


Figure 3. 32 Tangential field intensity component of the path bc at MMF = 707 A.t,  $\lambda_g$  = 70,  $t/\lambda = 0.5$ , and  $X_n = 0.4$

### 3.6.4 Torque Calculations:

In a FEA software, the torque on a rigid body can be obtained using Maxwell stress tensor method and is given by:

$$T = \int \left( (\bar{B} \cdot \bar{n}) (\bar{r} \times \bar{B} / \mu_0) - |\bar{B}|^2 (\bar{r} \times \bar{n}) / 2\mu_0 \right) ds \quad (3.15)$$

where  $\bar{r}$  is the position  $\bar{n}$  is the normal vector.



For the two dimensional planer case,  $\vec{r} \times \vec{B}$  has only a single out of plane vector component and can thus be treated as the scalar:

$$K = (r_x \cdot B_y - r_y \cdot B_x) \quad (3.16)$$

Therefore, equation (3.15) becomes:

$$|T| = \int (K \cdot \vec{B} / \mu_0 \cdot \vec{n}) ds \quad (3.17)$$

In all solutions, a circular integration path is chosen in the center of the airgap for different rotor positions as shown in figure-3.33. This path of integration, in ANSYS, is circular about the origin and the number of nodes used to define this path is chosen to be 360; it means that the angle between nodes is one degree. It is worth mentioning that the torque in this method is in N.m/m. Therefore the resultant torque is calculated by multiplying the obtained result with stack length. However in FLUX2D, it is easier to get the torque without defining an integration path since the rotor is considered as one region. Also during definition of the physical problem, FLUX2D asks the user to define the stack length. So the torque value obtained is the final value of the static torque and there is no need to do some calculations to consider the stack length.

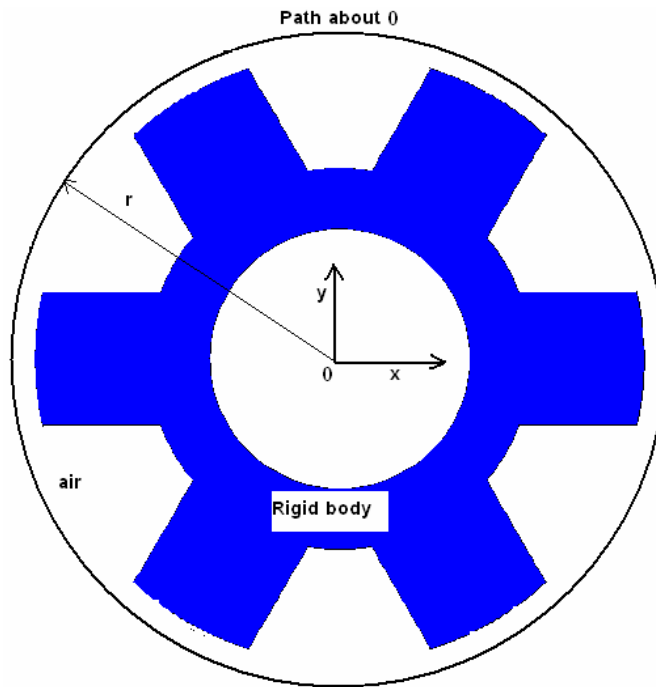


Figure 3. 33 Path of integration around a rigid body for torque calculation

### 3.6.5 Flux Linkage Calculations:

Nodal magnetic potential ( $A_z$ ) is available in both ANSYS and FLUX2D postprocessing phase.  $A_z$  can also be used to visualize the flux lines. In this work, two methods have been used to perform flux linkage calculations. It is found that their results are the same.

#### *Method A:*

Between any two nodes in the model, the flux passing between the nodes can be calculated by the following equation:

$$\Phi = \oint \bar{A} \cdot d\bar{l} \quad (3.18)$$

In this case the integration is carried out following a closed loop extending into the z direction since  $A_z$  has no component in the x direction. Contribution to the integral part of the contour along x direction is zero. If a unit length of magnetic core is considered in the z direction, it may be concluded that flux through the stator teeth as seen from figure-3.34, can be calculated from the equation:

$$\Phi_2 = (A_1 - A_2) \quad (3.19)$$

where;

$A_1$  is the magnetic vector potential of node number 1 in figure-3.34

$A_2$  is the magnetic vector potential of node number 2 in figure-3.34

$\Phi_2$  is flux per pole per turn.

The flux linkage per phase (Wb.turns) maybe calculated from the equation:

$$\psi = (2 * N) * \Phi * L \quad (3.20)$$

where;

$L$  is the stack length

$N$  is the number of turns

On the other hand flux leakage may be assumed to be:

$$\text{Leakage flux} = (2 * \Phi_1) - \Phi_2 \quad (3.21)$$

where  $\Phi_1$  is the flux through surface shown in figure-3.33. Leakage fluxes can be seen on  $A_z$  graphs.

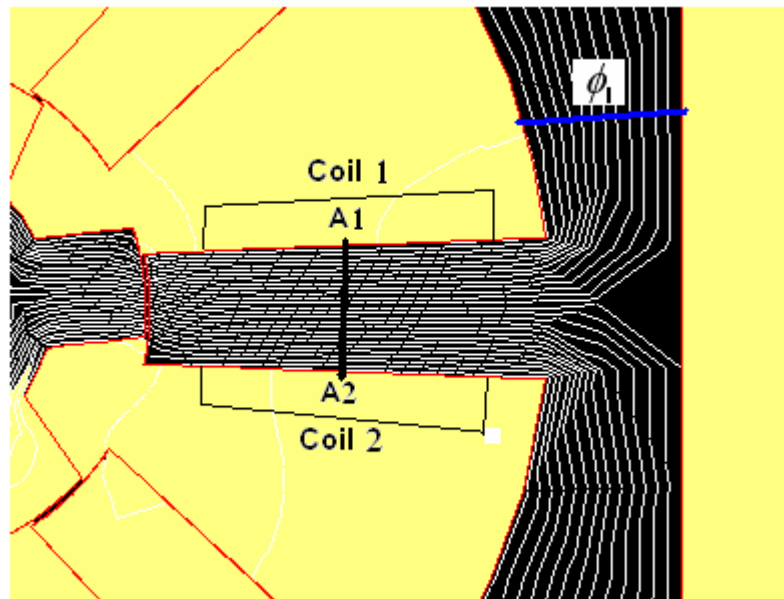


Figure 3.34 Calculation of Flux per pole

Using this method, it is assumed that leakage flux will not be contained through the integration path, if the nodes on the edges of the slot are chosen. But, it is very difficult to predict where leakage flux deviates from the slot region. Another assumption, explained as the second method aims averaging the linkage flux values calculated between different node patterns placed on the coils.

***Method B:***

A second method recommended by Prof. Jack is also tested. For this purpose a macro file is written to find average magnetic flux density over a coil.

In this approach flux can be calculated from:

$$\text{Flux linkage / pole/turn} = \Phi = A_1 - A_2 \quad (3.22)$$

where,

$A_1$  is the average flux of coil number 1

$A_2$  is the average flux of coil number 2.

Note that this method is similar to method 1. The only difference in this case is that an average node potential is considered for the calculations. In this study both are found to give almost identical results.

It is worth to point out that the macro file written for this purpose traces the following steps:

- 1- From ANSYS magnetic field solution find nodal magnetic vector potential  $A_i$  for every node on coil 1 (figure-3.35).
- 2- From ANSYS magnetic field solution find nodal magnetic vector potential  $A_i$  for every node on coil 2 (figure-3.35).
- 3- Find average magnetic vector potential of coil 1 from:

$$A_1 = \frac{\sum A_i}{n} \quad (3.23)$$

where  $i = 1, \dots, n$  is the node number.

- 4- find average magnetic vector potential of coil 2 from:

$$A_2 = \frac{\sum A_i}{n} \quad (3.24)$$

- 5- Then,

$$\text{Flux linkage / pole/turn} = \Phi = A_1 - A_2 \quad (3.25)$$

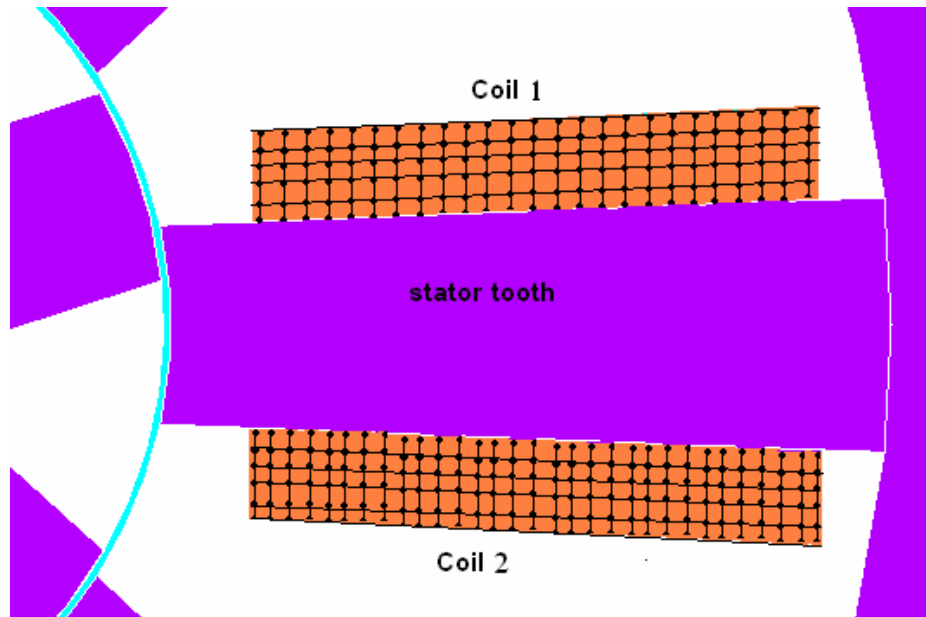


Figure 3. 35 Nodes of excited coils

### **3.7 Conclusion**

In this chapter, the developed model for permeance and Force Calculations has been well introduced and built by using two FEA softwares. For the aim of investigating the model, five steps were performed, that is; the mesh has been studied and chosen well to give accurate results, the solution criteria as well. Then an investigation of coil excitation has also been performed and it is found that the coil excitation equals to the summation of MMF drop on C-core of the model and MMF drop on the teeth and the airgap. In addition, the MMF drop on the core is negligible, thus adding the core has no effect on the desired value of excitation. The next step was investigating the model by contour plots as a preliminary check for whether the boundary condition was defined properly. Finally, ANSYS has been used to compare its results with that of FLUX2D; the percentage error was low.

The author has also discussed how he obtained the data; tooth flux density, normalized permeance, tangential force and normal force. Besides, the flux linkage and static torque computations are also explained in this chapter as a base for chapter four, where the author is going to discuss the model verification, and for chapter 5 where the normalized data will be introduced.

## **CHAPTER 4**

### **FEA VERIFICATION**

#### **4.1 Outline**

For the aim of verification the normalized data, which will be introduced in chapter five, the author will first compare analytically calculated permeance data available in the literature [20] with his numerical solutions. Secondly, he is going to solve two test switch reluctance motors (two dimensional solutions) for obtaining torque-position and flux linkage-position characteristics by using finite element method. Measurements of static torque and flux linkage of the test motors are available. Hence, a comparison between measurements and FEA results can be performed. In addition, just to check whether the results are reliable, the author used two softwares based on FEA (FLUX2D & ANSYS) to be sure that each problem has been defined well without any mistake.

#### **4.2 Comparison of Analytically Calculated Permeance with Numerical Computations:**

In their work, Mukherji K.C. and Neville S. [20] calculated numerical values for the permeance per tooth pitch between two identically slotted surfaces when the teeth are aligned and when they are out of alignment, for a range of normalized tooth and slot widths. This work was based on analysis by F. W. Carter, whose name is universally associated with analytical work, involving conformal transformation, on the airgap field in electrical machines. The work that makes his name familiar to machine designers through Carter's coefficient was extended later by him with the treatment of an infinite iron surface with regular rectangular slots, infinitely deep, facing another smooth infinite iron surface, where a uniform MMF is maintained across the airgap between



these two equipotential surfaces, or, equivalently, of two such equipotential surfaces both slotted identically, and with the teeth of one exactly opposite the identical teeth on the other. It is important to point out that in the problem dealt with by Carter in Mukherji's work the teeth are assumed to be infinitely permeable.

Mukherji and Neville introduced the data in the form of graphs. The first graph represents the data for minimum magnetic permeance which is computed from unaligned position (OUT position). The second graph represents the data for maximum magnetic permeance which is computed from the aligned position (IN position). They calculated normalized permeance for both IN and OUT position covering the following range:

$s/g$  ranges from 0.1 to 20, and

$t/g$  ranges from 0.0 to 10

where 's' stands for slot width, 't' for tooth width and 'g' for airgap width. Figure-4.1 and figure-4.2 show the two positions of alignment, IN and OUT position, respectively. It is worth mentioning that in OUT position the tooth in one side is in the center of the other side. In addition, both figures have identical slotting in both sides.

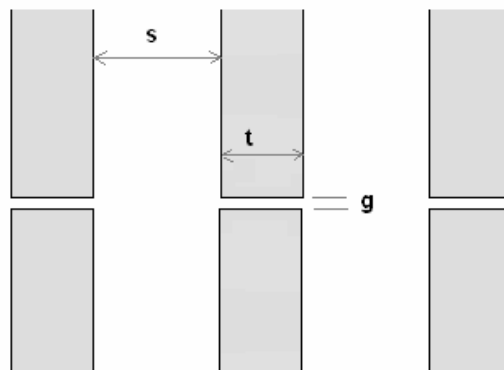


Figure 4. 1 IN Position Alignment

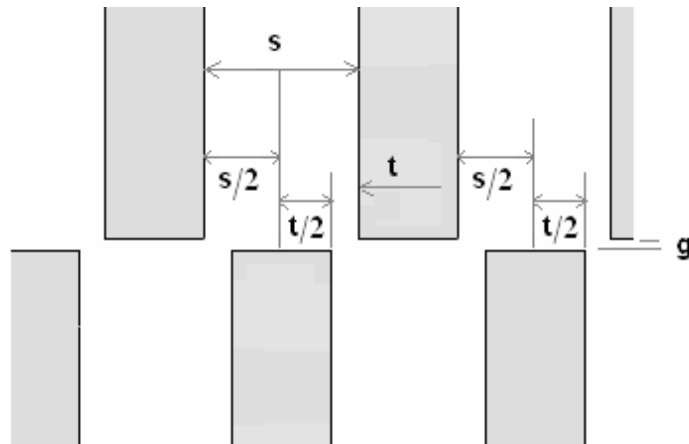


Figure 4. 2 OUT Position Alignment

In this work, the author built eight geometries having dimensions taken from the graphs of Mukherji in his paper. Table-4.1 shows these points; four points for IN position and four points for OUT position, where  $\lambda$  stands for tooth pitch which is equal to summation of slot width and tooth width. These points are in terms of the airgap length; therefore, the author chose a value of 0.5 mm for the airgap. This value is suitable for FLUX2D; especially for the mesh since the dimensions of meshing elements are measured in mm and the allowable length for an element can not be less than 0.003 mm. This means that if  $g$  is chosen as 3 mm, then the user must place many rows of elements in the airgap to have fairly accurate results. On the other hand, if  $g$  is chosen as 0.02, the user will not only have a difficulty in meshing the problem, but also a large number of elements will be required for the whole problem, hence the time of solutions will increase significantly.

Table 4. 1 Data points chosen for IN & OUT positions (g = 0.5mm)

Point	Position	t/g	s/g	$\lambda$
1	IN	6.4	20	13.2
2		6.8	1.6	4.2
3		7.2	7.0	7.1
4		8.8	8.0	8.4
5	OUT	4.0	4.0	4.0
6		6.0	4.0	5.0
7		6.4	2.8	4.6
8		7.2	6.0	6.6

The geometry of the model, which is introduced in chapter 3 section 3.3 and shown in figure-3.2, is used to solve for the points shown in table-4.1. However, since Mukherji assumed that the teeth are infinitely permeable, the author defined a material, in FLUX2D, having a relative permeability,  $\mu_r$ , of  $10000 * \mu_0^{-1}$ , which can be considered as infinitely permeable. Air is defined to have a relative permeability of one.

According to mesh, since here we don't have identical slotting, the author redefined the mesh in such away that it must be finer than the mesh defined for the model shown in chapter 3. But the mesh distribution in the airgap should be studied carefully as it is the region where the field changes rapidly and chosen as 0.5 mm which is larger than the airgap lengths chosen by Ertan [11]. For this aim, two mesh strategies has been performed. First, the author assigned four rows of elements in the airgap region to match the mesh definition used for the model of normalized data and he obtained the data of magnetic permeance. Second, he assigned six rows of elements in the airgap and also he set the number of elements dividing a tooth to be 600 elements. As an illustration to second mesh, figure-4.3 shows element distribution in the airgap between two aligned teeth for dimensions corresponding to case-4 shown in table-4.1, where:

$$t/g = 8.8,$$

$$s/g = 8.0,$$

$$g = 0.5 \text{ mm}$$

hence  $\lambda = 8.4$

$d = 40 * g$  , where  $d$  is the tooth depth (the reason behind choosing  $40 * g$  (see Fig-4.6) is to eliminate the slot effect and can be considered as sufficiently deep as concluded by Ertan [11]).

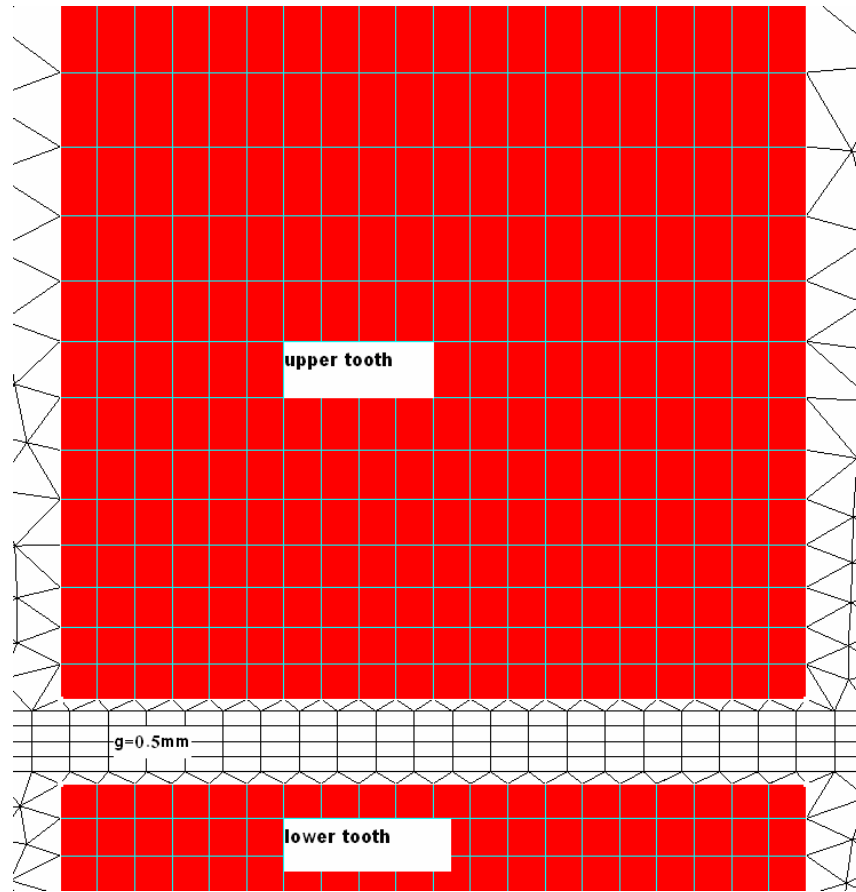


Figure 4. 3 Distribution of elements in airgap and in half of the upper tooth depth.

Again, as clarified in chapter three, Dirichlet condition is assigned to the shell surrounding the model to ensure that there will be no flux exiting the shell. According to the solution criterion is also set to  $1e-5$ .

However, since the problem is linearized (constant very large permeability), any current value can be given to the coil for each solution just to compute the normalized permeance for the corresponding geometry. After solving the problem, contour plots were obtained as a preliminary check. Figure-4.4 and figure-4.5 show the contour plots for IN position and OUT position respectively. As seen from the symmetry of the contour plots in both figures, it ensures that there is no problem in the definition of the boundary condition. Moreover, it can be said that the mesh distributions in the teeth are identical to each other.

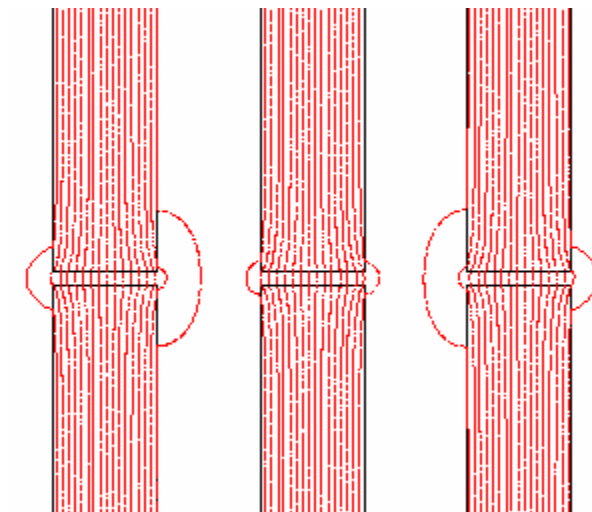


Figure 4. 4 Flux contours for IN position ( $t/g = 8.8$ ,  $s/g = 8.0$ )

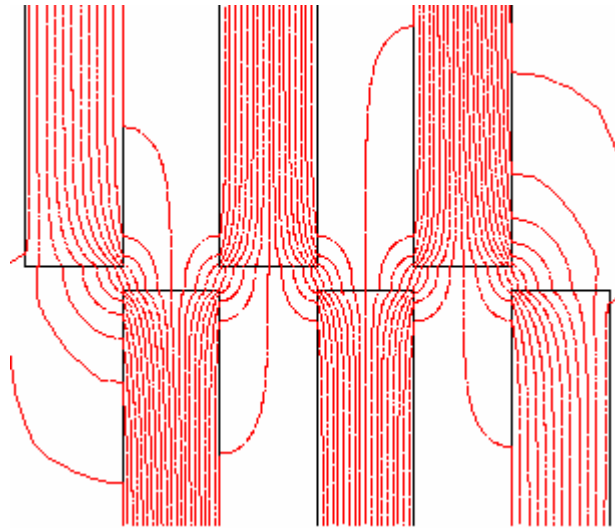


Figure 4. 5 Flux contours for OUT position ( $t/g = 8.8$ ,  $s/g = 8.0$ )

In addition, the author has investigated the model by checking the MMF drop as explained in chapter three (section 3.5.3). For this aim, two paths were drawn in C-core; the first path starts from the center of the mid tooth and ends in the center of the opposite tooth as shown in figure-4.6. The second path starts from the center of a slot and ends in the center of the opposite slot. It is found that the drop on C-core comes to be not more than 0.231 Amp.turn when the coil is excited by 1200 Amp.turn. Although this is a very small value compared with the source, the author considered it through exciting the coil by 1200.23 Amp.turn which is equivalent to 1200 Amp.turn when the core is theoretically assumed to be infinitely permeable.

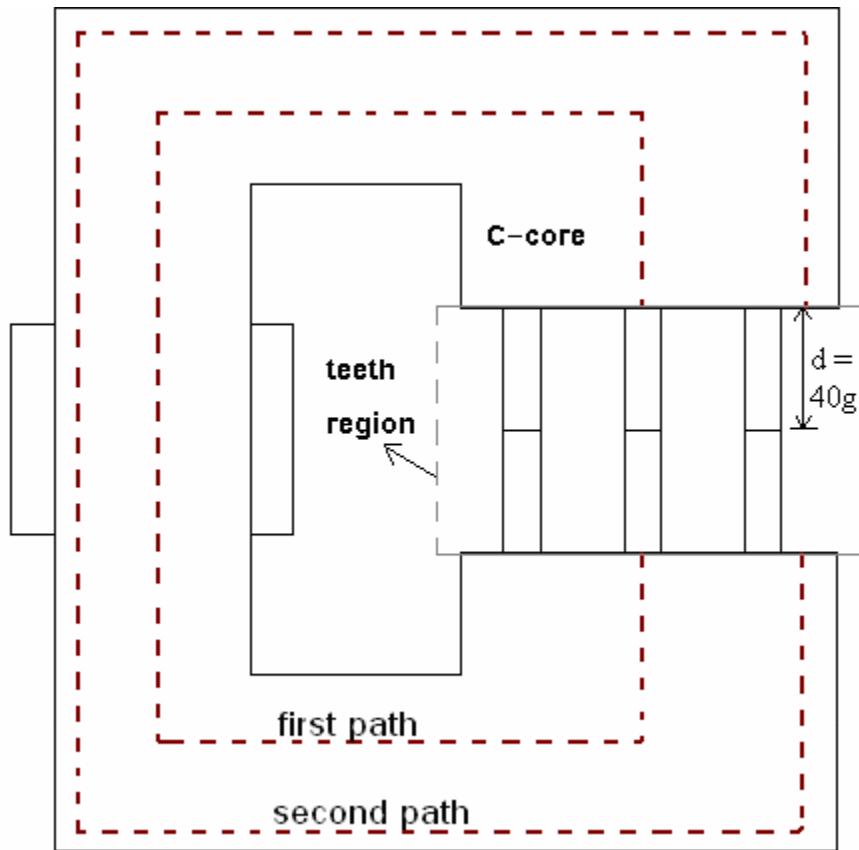


Figure 4. 6 Investigating the MMF drop on C-core

Table-4.2 shows the results obtained by FLUX2D and compared with the calculations of Mukherji. Where;

- $\mathbf{X}$  : relative position between the upper teeth and lower teeth, here only two position were considered; IN and OUT position.
- $\mathbf{B}_t$  : tooth flux density in Tesla. (tooth pitch flux / tooth area).
- $\mathbf{P}_n$  : normalized permeance obtained from the graphs of Mukherji.
- $\mathbf{P}_n^*$  : normalized permeance obtained from FLUX2D using the mesh described in chapter three section 3.4.2.2.
- $\mathbf{P}_n^{**}$  : normalized permeance obtained from FLUX2D using the mesh described in 4.2.

**ERR** : percentage error and is equal to  $(P_n - P_n^*)/P_n * 100\%$

In chapter three, sections 3.6.1 and 3.6.2 show how the author calculated the tooth flux density and the normalized permeance.

Table 4. 2 Normalized permeance results ( $P_n^*$  for FLUX2D)

Point	X	t/g	s/g	$\lambda$	$B_t(T)$	$P_n$	$P_n^*$	$P_n^{**}$	ERR
1	IN	6.4	20	13.2	3.981	0.340	0.3391	0.3394	0.26%
2		6.8	1.6	4.2	3.428	0.920	0.9224	0.9225	0.26%
3		7.2	7.0	7.1	4.421	0.640	0.6383	0.6386	0.27%
4		8.8	8.0	8.4	3.685	0.640	0.6395	0.6395	0.08%
5	OUT	4.0	4.0	4.0	3.376	0.560	0.5572	0.5575	0.50%
6		6.0	4.0	5.0	3.216	0.640	0.6380	0.6383	0.31%
7		6.4	2.8	4.6	3.607	0.780	0.7771	0.7772	0.37%
8		7.2	6.0	6.6	3.212	0.500	0.4981	0.4983	0.38%

The MMF assigned to the coil is 1200.23 Amp.turn for all solutions. From the table, it can be seen that the normalized permeance obtained from FLUX2D, either using the mesh described in chapter three or the one described in this section, is the same. This is probably because of two main reasons; first, the problem dealt with here consists of two materials having a linear relationship between B and H. Second, the mesh in the airgap region described in chapter three is highly acceptable; hence, it can be used to obtain the normalized data. However, the author just tried to calculate permeance using finer mesh in the airgap region to investigate the mesh described in chapter three and to consider the point that we have larger gap here. But, to be systematic and since the results are almost identical, he used the mesh described in chapter three. On the other hand, looking to the percentage error in table-4.2, it can be seen that FEA results meets Muhkerji's calculations. This means that the model is built and defined properly. In addition, the finite element method can be used as a tool on which the author can



depend to solve for the model described in chapter three where the teeth are assumed to have specific BH curve.

According to time of solutions in this section taking into account that the computer used has a CPU speed of 2.13 GHz and 2.0 GB RAM, it is ranging from 40 seconds to 50 seconds. Generally the solution time here is less than that mentioned in chapter three section 3.5. This is because of two reasons; first, the teeth here are smaller in dimensions than that used to obtain the normalized data. Second, the materials used in this section have linear BH characteristic, thus the solution can be done with fewer number of iterations.

### **4.3 Solutions of Test Motors**

In this section, two switch reluctance motors are solved by using two FEA-based softwares; FLUX2D and ANSYS. The aim of solutions is to calculate static torque of the motors when one phase is excited and to calculate the flux linkage per pole as a function of rotor position. The computations of torque and flux linkage from field solutions are described in sections 3.6.4 and 3.6.5 respectively. Later on, the author will introduce and compare the results in terms of rotor position with the measurements.

#### **4.3.1 Test motor 2 (SR2)**

##### **4.3.1.1 Specification of SR2**

The dimensions of the SR2, which has a rated current of 3A/pole, are given below in table-4.3, and the whole motor structure is shown in figure-4.7:

Table 4. 3 Dimensions of SR2

<b>Dimensions</b>	<b>Value</b>
Rotor outer diameter, $Dr$	38.6 mm
Stator outer length (thicker part)	120.4 mm
Stator outer length (thinner part)	111.4 mm
Stator core inner diameter	99.99 mm
Stator pole tip width, $ts$	8.4 mm
Tapering angle	2.2 degrees
Rotor tooth width, $tr$	8.35 mm
Airgap length, $g$	0.325 mm
Rotor tooth depth, $hr$	7.2 mm
Stator pole depth, $hs$	34.37 mm
Shaft diameter, $Dsh$	16.5 mm
Core length	40.4mm

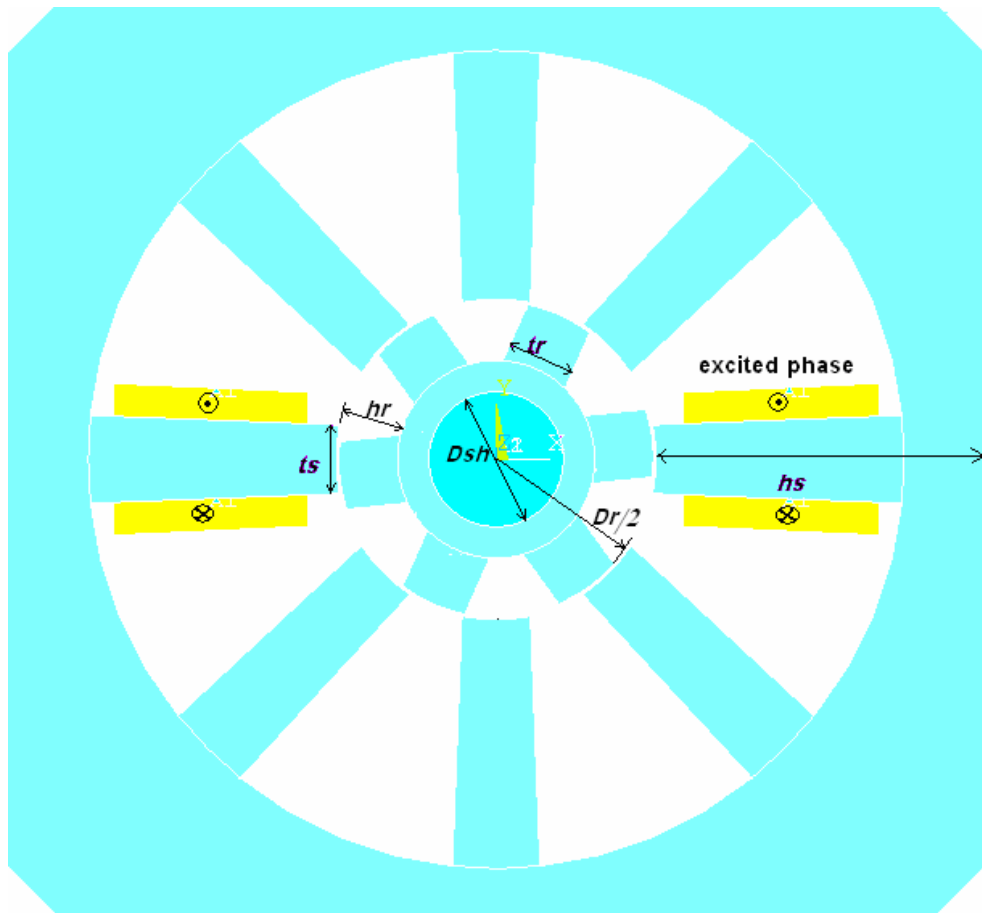


Figure 4. 7 SR2 Geometry

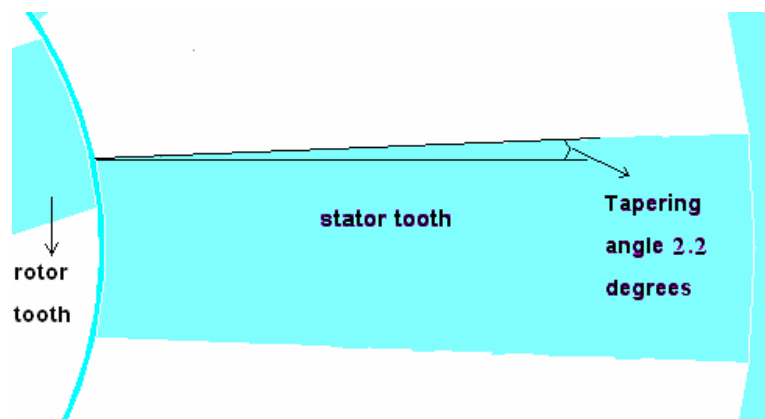


Figure 4. 8 Tapering angle of the stator tooth

In step motors, a phase can be defined by the set of coils which are excited separately for applying a specific pattern of excitation. As pointed in figure-4.7, the yellow regions stand for the set of coils that forms a phase. This phase is the one that is going to be excited for all solutions at three levels of excitations; 1 A, 2 A and 3A. In general, the number of discrete positions in which the specific pattern of excitation can be established relative to the stator structure equals to the number of phases and denoted by 'q'. When excitation sequence is changed, the rotor moves by an angular displacement which is termed as 'step angle',  $\alpha$ . The step angle of an SRM is determined by the number of teeth on the rotor and stator and the number of phases. It can be calculated by the following equation:

$$\alpha = \frac{2\pi}{q.N_r} \quad (4.1)$$

where  $N_r$  denotes the number of poles.

So for SR2, the number of phases is 4 and the number of poles is 6. Then:

$$\alpha = \frac{360}{4 * 6} = 15^0 \quad (4.2)$$

In addition, the rotor tooth pitch,  $RTP$ , over which the torque curve of the motor is periodic, is:

$$RTP = n * \alpha = 4 * 15 = 60^0 \quad (4.3)$$

In this work, the author will solve for several rotor positions. These positions are expressed in terms of normalized position,  $X_n$ , as given in the following equation:

$$Position = X_n * \frac{RTP}{2} = X_n * 30^0 \quad (4.4)$$

where  $X_n$  ranges from 0.0 to 1.0. However, the author only solved the two test motors for  $X_n=0.0$  (IN position), 0.2, 0.4, 0.6, 0.8, and 1.0(OUT position).

#### 4.3.1.2 Mesh of SR2 in ANSYS

Distribution of mesh must be done carefully taking into account that a dense mesh must be placed in the airgap region. Also, enough mesh distribution should be given to two teeth which correspond to the excited phase while other teeth have less distribution to save time. It is important to point that the element type chosen for mesh strategy is Higher-order PLANE53. PLANE53 models 2-D (planar and axisymmetric) magnetic fields. The element is defined by 8 nodes and has up to 4 degrees of freedom per node: z component of the magnetic vector potential ( $A_z$ ), time-integrated electric scalar potential (VOLT), electric current (CURR), and electromotive force (EMF).

PLANE53 is based on the magnetic vector potential formulation and is applicable to the following low-frequency magnetic field analyses: magnetostatics, eddy currents (AC time harmonic and transient analyses), voltage forced magnetic fields (static, AC time harmonic and transient analyses), and electromagnetic-circuit coupled fields (static, AC time harmonic and transient analyses). The element has nonlinear magnetic capability for modeling B-H curves or permanent magnet demagnetization curves. Figure-4.9 shows the nodes on the elements of this type.

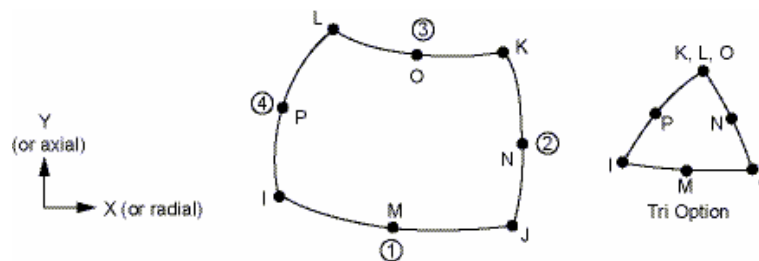


Figure 4. 9 Higher-order Element PLANE53

PLANE53 is also available in FLUX. In both of ANSYS and FLUX, using this type of elements has a technical advantage; i.e. the author used this type of element to increase the number of nodes instead of increasing the number of elements where a difficulty in controlling the distribution of elements in the airgap region can be faced.

Figure-4.10 shows the complete, meshed geometry of SR2. As seen in the figure, the air gap is meshed by very small elements while back core of stator has the largest elements. The author has meshed the teeth corresponding to phase A, which is going to be excited, by more elements than the other teeth.

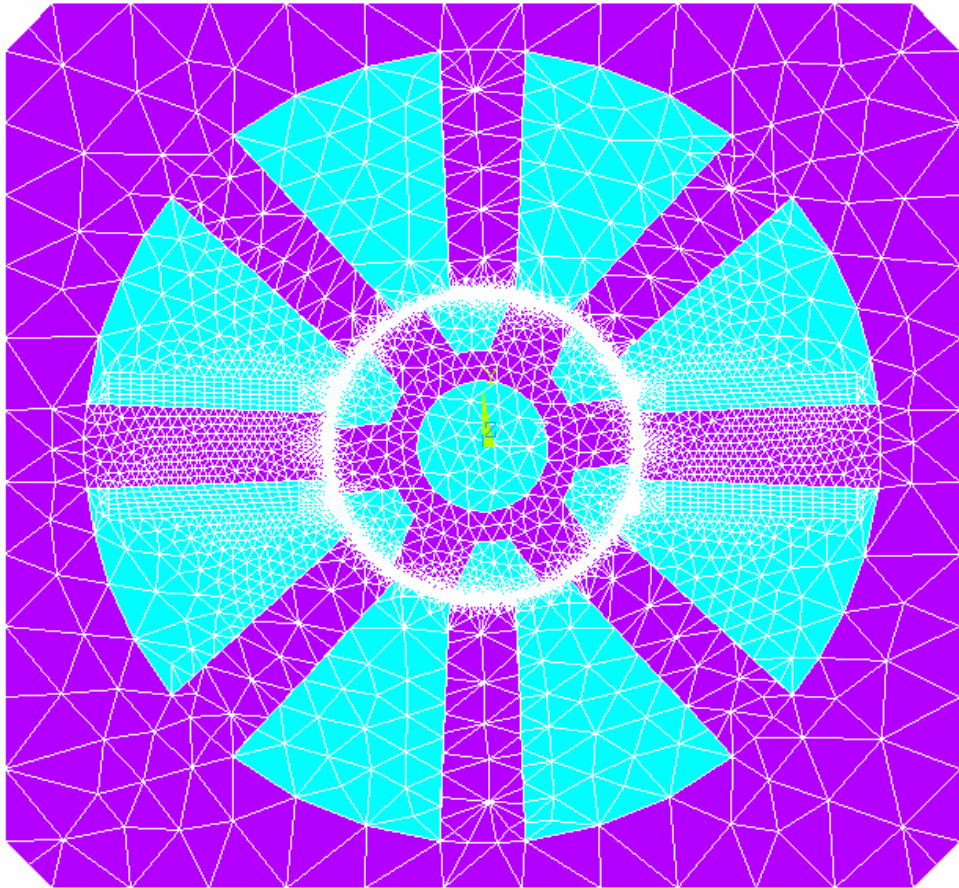


Figure 4. 10 Mesh distribution of SR2 at 6 degrees (Normalized position = 0.2).

In table-4.4, mesh information of the whole model is summarized. As mentioned in chapter 3, the time of solution is proportional to the number of elements. So, 40000 nodes is a reasonable choice for such a motor.

Table 4. 4 Mesh information

Total Number of Nodes-ANSYS	40000
Total Number of Nodes-FLUX	41500
Type of elements	PLANE53
Rows of elements in the airgap	3

Mesh distribution in the airgap is very important and must be dense as much as possible. However, three rows of elements were used to mesh the airgap region from PLANE53 type which gives us five rows of nodes inside the region. Figure-4.11 and figure-4.12 show element and nodes distribution, respectively, in the airgap region.

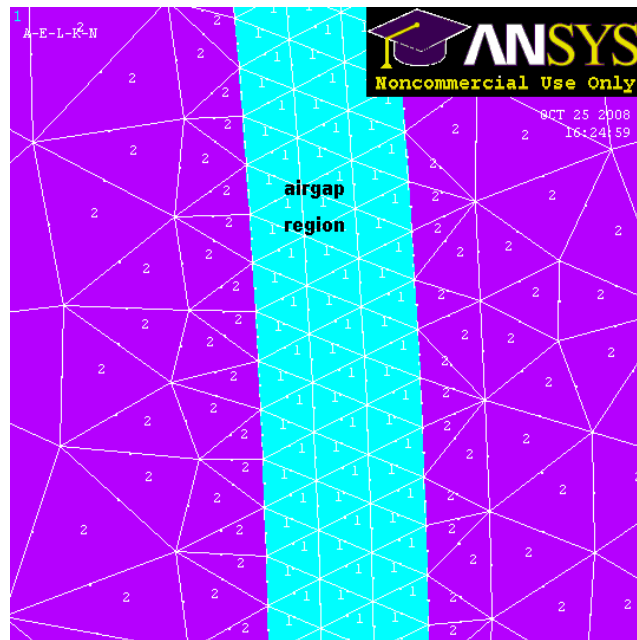


Figure 4. 11 Element ddistribution in the airgap region (three rows) at rotor position of 6 deg.

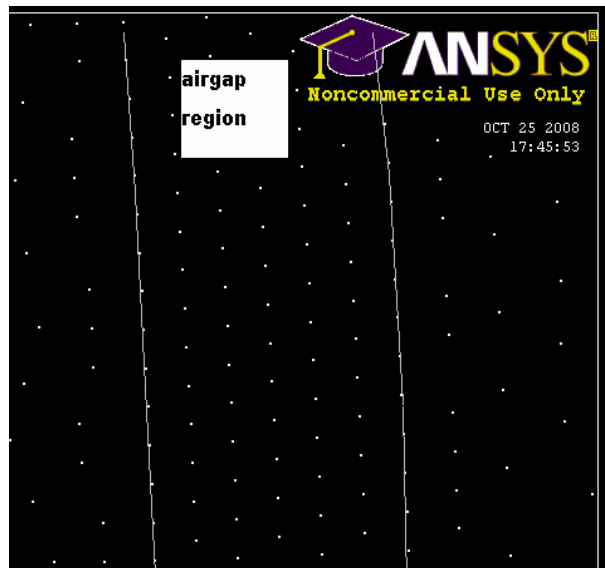


Figure 4. 12 Nodes distribution in the airgap region (five rows of nodes) at rotor position of 6 deg.



#### 4.3.1.3 Shifting the Rotor

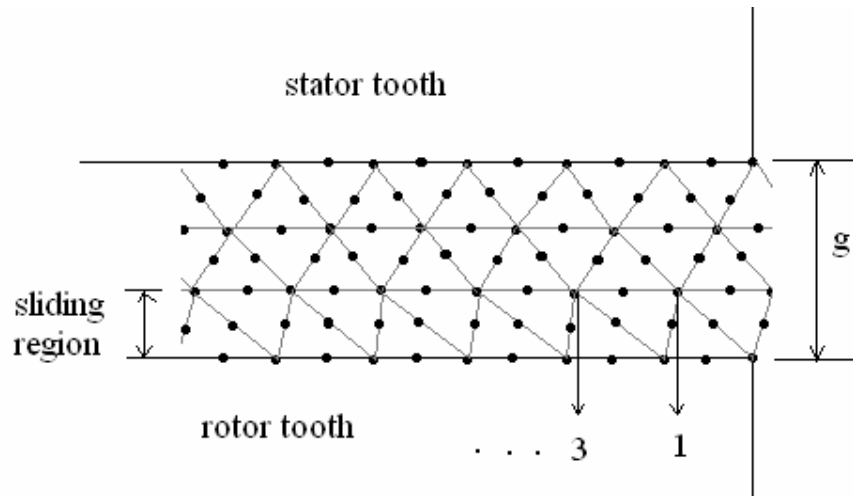
To modify any point in the geometry, the mesh must be erased completely, otherwise it is impossible to do any geometric modification in the model. This is mainly because of the fact that once the user finishes meshing a problem, the elements then represent the hard model. This means that original points and lines that the geometry consists of becomes useless in terms of finite element analysis.

The author needs to solve SR2 for different rotor positions. Hence, it is not logical to redraw the whole geometry to obtain another rotor position. And someone perhaps may suggest to redraw the rotor only while getting the geometry of stator from previous solutions through some techniques available in the FEA tool. However, both cases waste time. The author has succeeded to quickly obtain another rotor position as follows:

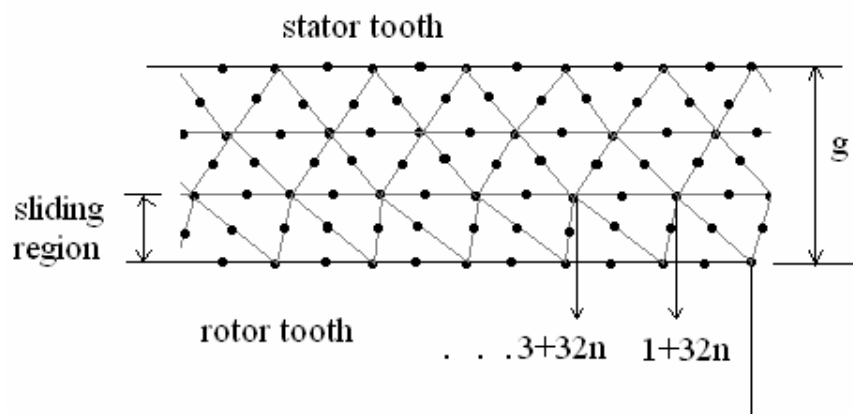
While drawing the geometry of the motor at zero position, he defined two coordinate systems; one for the stator geometry and the other for rotor geometry. Rotor coordinate system is defined as a polar type. By this definition, the user can easily change the angle of this coordinate; consequently, all the points and lines corresponding to the rotor will also shift at the same angle of rotation. Once the new position is obtained, the user has to mesh the model again.

According to the mesh, the author has divided the airgap region into three equal regions, and each line surrounding these regions, including exterior lines, is assigned 960 elements resulting into 160 elements per tooth pitch. To show that mesh doesn't change when shifting the region, consider figure-4.13a, this figures shows a portion from stator tooth and rotor tooth at aligned position and the airgap between them. Two arbitrary nodes are chosen and assigned the numbers 1 and 3. It is worth mentioning that the different positions are sought to be 0.0 (IN), 0.2, 0.4, 0.6, 0.8, and 1.0 (OUT). That is, they are five positions, and since these positions are fractions of the rotor tooth pitch then, in terms of nodes, the difference between any two successive positions will be  $160/5 = 32$  nodes. So when a different position is sought, the corresponding rotor nodes

in figure-4.13a will move to form new elements with  $1+32n$ ,  $3+32n\dots$  as shown in figure-4.13b, where  $n$  stands for the position number starting from 1 for aligned to 5 for OUT position. Hence no change will be obtained in the positions of the nodes inside the sliding regions. As a result, the mesh is identical for all positions.



(a) nodes distribution at rotor position-1



(b) nodes distribution at rotor position-2

Figure 4. 13 Nodes distribution at two different rotor positions.

#### 4.3.1.4 Definition of Physical Problem

Once the geometry of the model is built, definition of the physical problem comes as the next step. Definition of the physical problem includes application of boundary condition, loading, and definition of materials.

Firstly, for the exterior nodes of the motor (exterior boundary of the stator) flux parallel boundary conditions are applied. It means that the parallel component of the magnetic vector potential is defined as zero. It is supposed that only one phase is excited at the time of analysis. Loading includes also excitation; in this stage one needs to define current excitation. Figure-4.14 shows the right set of coils for phase A that is going to be excited. Here, according to the coils, one can set the desired Magneto Motive Force (MMF) by one of the following choices offered by Flux2D and no difference in results for which one we choose:

- Total Value option assigns current value to the region (equivalent to one turn). As an example, to excite phase A with 3A, the value must be  $3 \times 320 = 960$  A which can be applied to each coil side if this option is used.
- Density option assigns amperes/mm<sup>2</sup> to the region. Current density can be calculated by the following equation:

$$J = \frac{N * I}{t_d * t_c} \quad (4.5)$$

where  $t_d$  (=24.66mm) is the length of the region where the conductors are to be placed,  $t_c$  (=4.0mm) is the width of that region as shown in figure- 4.14.

In this study, excitation level will be at 1A, 2A, and 3A. The corresponding current density values are shown in table-4.5. In ANSYS the user has only the second option; loading as density.

Table 4. 5 Excitation Levels

I	$J$ (A/m <sup>2</sup> )
1 A	3.2441e6
2 A	6.4883e6
3 A	9.7324e6

- Ampere Turns option assigns both of current and number of turns of the coil for the corresponding region from an external circuit.

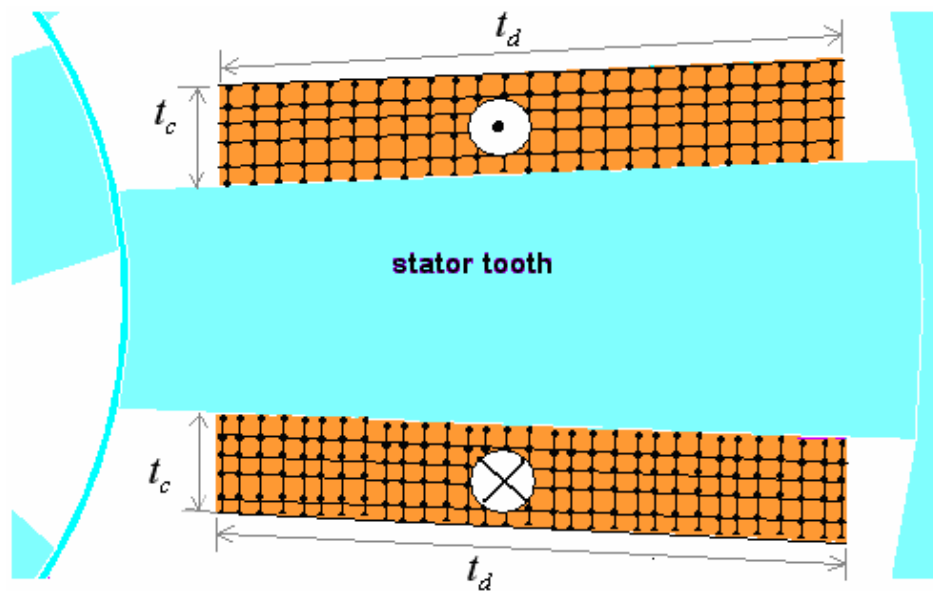


Figure 4. 14 Right coil set of phase A

It is worth mentioning here that the stator and rotor have been given the BH-curve shown in table-3.1, section 3.4.3 of chapter 3. Other regions; slots, airgap, shaft, are defined as Vacuum with a relative permeability of 1.

After definition of physical problem, the model is ready to be solved.

#### 4.3.1.5 Solution Criteria in ANSYS:

Figure-4.15 shows the solution criteria set for all solutions. The magnetic vector potential (MVP) formulation in ANSYS is defined to have 5 which is the number of ramp substeps. The convergence tolerance is set to be 1e-5 with 30 iterations as a maximum allowable number of iterations. The convergence tolerance is given by:

$$\delta A_j = - \left| \frac{\partial^2 F}{\partial A_i \partial A_j} \right|_{A+\delta A}^{-1} \left| \frac{\partial F}{\partial A_i} \right|_A \quad (4.6)$$

where,  $A$  is the magnetic vector potential,

$i$  and  $j$  are integers varying from 1 to the number of grid points  $N$ , and

$F$  is the energy functional and given by:

$$F = \int_v \left( \int_0^B H \cdot dB \right) dv - \int_v \left( \int_0^{A_z} J \cdot dA \right) dv \quad (4.7)$$

where:

$\nu$  is the reluctivity (inverse of permeability) ,

$H$  is the field intensity vector,

$B$  is the flux density vector,

$\bar{J}$  is the current density vector,

$A_z$  is the z-component of magnetic vector potential.

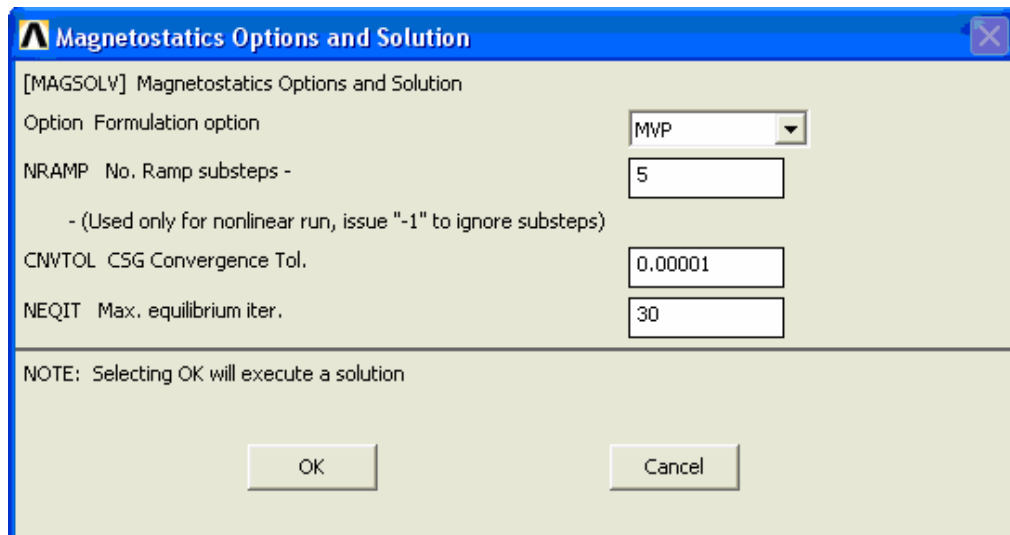


Figure 4. 15 Solution Criteria.

#### 4.3.1.6 Contour Plots

As stated in chapter 3, the best way to quickly understand and to check the reliability of the results of finite element analysis is to obtain a contour of the calculated potential. The contour plot shows whether the desired boundary conditions have been properly applied or not. Figure-4.16 shows the two dimensional flux lines (contour plots) for 3A excitation at a position of 18 degrees or 0.6 as a normalized position. From the figure, it can be noticed that there is no mistake done in the definition of physical problem. Figure-4.17 shows the color distribution of the flux density. It is obvious that the maximum value of flux density doesn't exceed 2 Tesla, but only in the corners of the pole teeth tips.

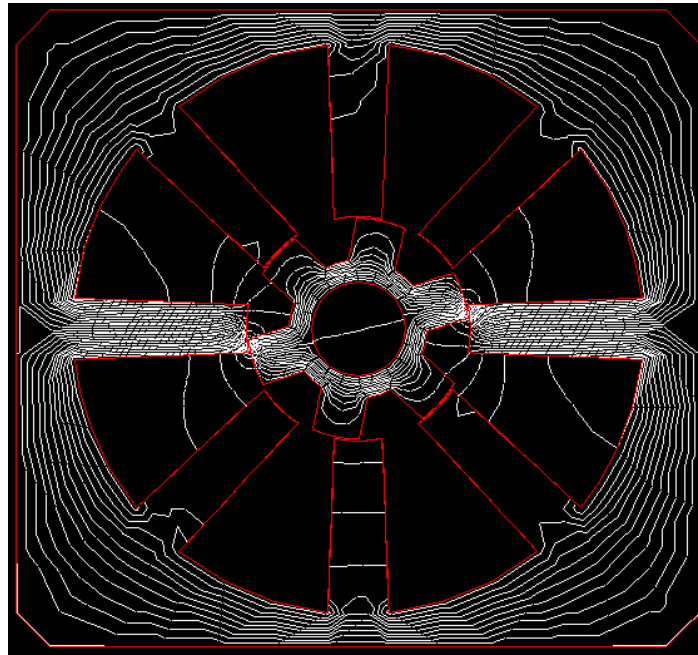


Figure 4. 16 2D Contour Plots for 3A excitation at  $X_n = 0.6$

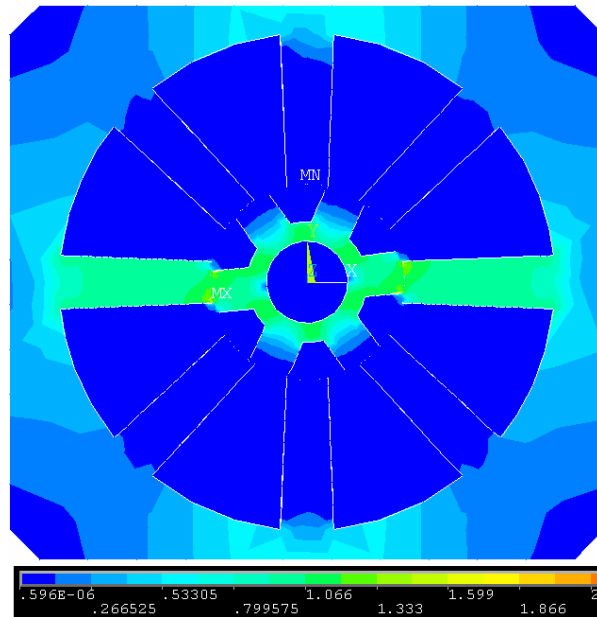


Figure 4. 17 Flux density for 3A excitation at  $X_n = 0.2$

### 4.3.1.7 ANSYS Results Compared with Measurements of SR2

Tables 4.6 and 4.7 show the results obtained by ANSYS for static torque and the measured static torque of SR2 (N.m). However, since the measured static torque results have different form of normalized position to that obtained by ANSYS, it is better to extract the measured static torque for the normalized positions: 0.0, 0.2, 0.4, 0.6, 0.8 and 1.0 so as to calculate the percentage error between measurements and ANSYS results. Table-4.7 also shows the extracted static torque for these positions. In tables 4.8, 4.9 and 4.10, the percentage error is shown and calculated by equation-4.8. In the same manner, the author extracted flux linkage measurements, shown in table-4.11, in terms of normalized position similar to that used in ANSYS. Tables 4.12, 4.13 and 4.14 show the percentage error between extracted flux linkage from measurements and ANSYS results. In section 3.6, the author explained how he calculated static torque and flux linkage data. Figure-4.18 and 4.19 show the results on graphs to better recognize matching between measured data and ANSYS results.

$$ERR\% = \frac{Measured - Numerical}{Measured} * 100\% \quad (4.8)$$

Table 4. 6 Static Torque Numerical Results of SR2 (in N.m)

X <sub>n</sub>	ANSYS 1A	ANSYS 2A	ANSYS 3A
0	0	0	0
0.2	0.226	0.597	0.820
0.4	0.249	0.888	1.48
0.6	0.255	0.925	1.679
0.8	0.240	0.791	1.390
1	0	0	0



Table 4. 7 Extracting static torque of SR2 from measurements (in N.m)

X <sub>n</sub>	Meas'd 1A	Meas'd 2A	Meas'd 3A
0.000	0.000	0.000	0.000
0.111	0.133	0.330	0.444
<b>0.2</b>	<b>0.185</b>	<b>0.525</b>	<b>0.748</b>
0.222	0.202	0.571	0.806
0.333	0.258	0.781	1.181
<b>0.4</b>	<b>0.270</b>	<b>0.842</b>	<b>1.375</b>
0.444	0.271	0.876	1.455
0.556	0.289	0.903	1.569
<b>0.6</b>	<b>0.278</b>	<b>0.905</b>	<b>1.588</b>
0.611	0.281	0.901	1.587
0.667	0.288	0.872	1.550
0.722	0.260	0.809	1.453
0.778	0.185	0.645	1.240
<b>0.8</b>	<b>0.167</b>	<b>0.582</b>	<b>1.150</b>
0.889	0.069	0.208	0.482
0.944	0.046	0.110	0.202
1.000	0.000	0.000	0.000

Table 4.8 Static torque measurements and ANSYS results for SR2 at 1A

X <sub>n</sub>	Measured 1A	ANSYS 1A	ERR%
0	0	0	0.0
0.2	0.185	0.226	-22.2
0.4	0.27	0.249	7.8
0.6	0.278	0.255	8.3
0.8	0.167	0.240	-43.7
1	0	0	0.0

Table 4. 9 Static torque measurements and ANSYS results for SR2 at 2A

Xn	Measured 2A	ANSYS 2A	ERR%
0	0	0	0.0
0.2	0.525	0.597	-13.7
0.4	0.842	0.888	-5.5
0.6	0.905	0.925	-2.2
0.8	0.582	0.791	-35.9
1	0	0	0.0

Table 4. 10 Static torque measurements and ANSYS results for SR2 at 3A

X <sub>n</sub>	Measured 3A	ANSYS 3A	ERR%
0	0	0	0.0
0.2	0.748	0.820	-9.6
0.4	1.375	1.48	-7.6
0.6	1.588	1.679	-5.7
0.8	1.15	1.390	-20.9
1	0	0	0.0

Table 4. 11 Measured Flux linkage of SR2 (in Web.turn)

X <sub>n</sub>	Meas'd 1A	Meas'd 2A	Meas'd 3A
0.000	0.299	0.425	0.468
0.111	0.284	0.411	0.455
0.222	0.261	0.393	0.443
0.333	0.23	0.368	0.43
0.444	0.195	0.335	0.405
0.556	0.169	0.296	0.37
0.611	0.153	0.274	0.348
0.667	0.139	0.251	0.328
0.722	0.122	0.23	0.305
0.778	0.108	0.21	0.286
0.889	0.092	0.183	0.263
0.944	0.087	0.175	0.257
1.000	0.083	0.165	0.251

Table 4. 12 Flux linkage Measurements and ANSYS results of SR2 at 1A

$X_n$	Measured 1A	ANSYS 1A	ERR%
0	0.299	0.269	10.0
0.2	0.267	0.248	7.1
0.4	0.208	0.196	5.8
0.6	0.157	0.141	10.2
0.8	0.102	0.085	16.7
1	0.083	0.065	21.7

Table 4. 13 Flux linkage Measurements and ANSYS results of SR2 at 2A

$X_n$	Measured 2A	ANSYS 2A	ERR%
0	0.425	0.398	6.4
0.2	0.398	0.383	3.8
0.4	0.348	0.327	6.0
0.6	0.279	0.242	13.3
0.8	0.202	0.169	16.3
1	0.165	0.129	21.8

Table 4. 14 Flux linkage Measurements and ANSYS results of SR2 at 3A

$X_n$	Measured 3A	ANSYS 3A	ERR%
0	0.468	0.440	6.0
0.2	0.446	0.421	5.6
0.4	0.417	0.380	8.9
0.6	0.353	0.309	12.5
0.8	0.280	0.239	14.6
1	0.251	0.194	22.7

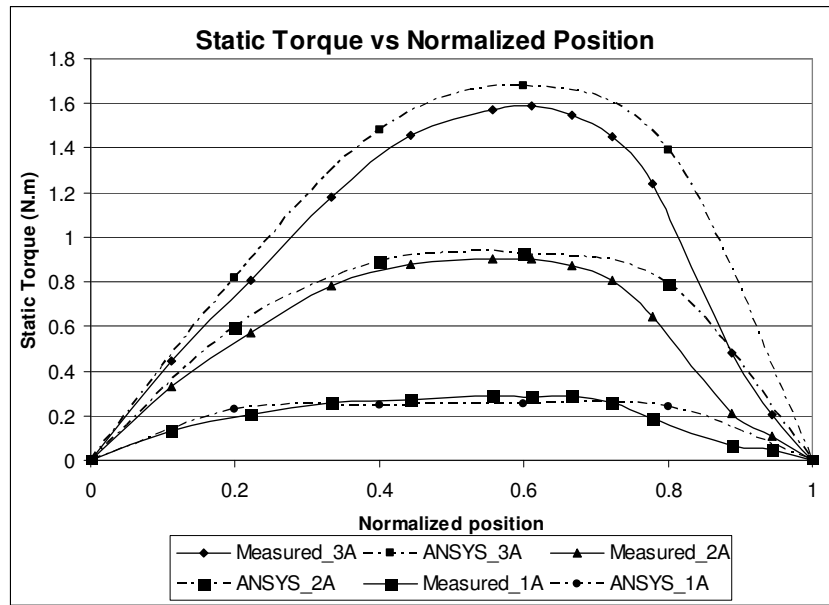


Figure 4.18 Static Torque vs Normalized Position of SR2

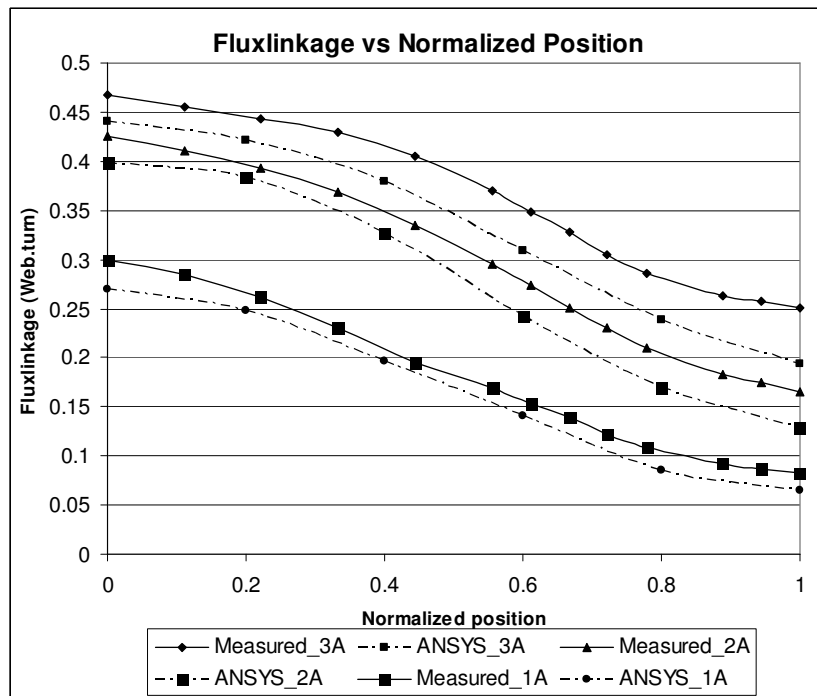


Figure 4.19 Flux linkage vs Normalized Position of SR2

As seen from the figures, there is a difference between measurements and ANSYS results and it is mainly because of errors in how the measurements were taken. In addition, it is obvious that the error increases as the rotor moves from IN position to OUT position direction. In other words, the error is largest nearly at a normalized position of 0.8 and 1.0. This error is possibly because it was not possible to fix the rotor position accurately for these two measurements.

Another important reason that contributes to have a noticeable error is that the solutions performed in this study are two dimensional. This means that the end leakage effect is neglected in these solutions. The result of ignoring the end leakage effect can be seen obviously from the flux linkage data where the all the results of ANSYS solutions are less than the measured flux linkage data. However, to include the end leakage effect, in section 4.3.1.9 the author will use a software tool developed by Goynük.

#### **4.3.1.8 Flux2D Results compared ANSYS Results:**

The author used FLUX2D software to obtain numerical solutions for SR2. The procedure of defining a problem in FLUX2D is introduced in details for the main model in chapter three. It is also the same procedure in ANSYS; the author meshed SR2 to have almost identical mesh especially in the airgap region and teeth. The same boundary condition is also applied. The BH-curve shown in table-3.1 is used to define the material property for stator and rotor in FLUX2D. However, in FLUX2D it is easier to obtain the static torque and flux linkage data. Tables 4.15-4.17 and tables 4.18-4.20 show, respectively, numerical results of static torque and flux linkage as a function of normalized position for both ANSYS and FLUX2D. Also the percentage error, which is calculated by equation 4.9, is included in the tables and the curves of measurements are redrawn in figures 4.20 and 4.21 to well compare them with FLUX2D results.

$$ERR\% = \frac{ANSYS_{Result} - FLUX_{Result}}{ANSYS_{Result}} * 100\% \quad (4.9)$$

Table 4. 15 ANSYS and FLUX2D Static torque Results at 1A

X <sub>n</sub>	ANSYS 1A	FLUX2D 1A	ERR%
0	0	0	0.0
0.2	0.226	0.218	3.5
0.4	0.249	0.254	-2.0
0.6	0.255	0.260	-2.0
0.8	0.240	0.234	2.5
1	0	0	0.0

Table 4. 16 ANSYS and FLUX2D Static torque Results at 2A

X <sub>n</sub>	ANSYS 2A	FLUX2D 2A	ERR%
0	0	0	0.0
0.2	0.597	0.580	2.8
0.4	0.888	0.893	-0.6
0.6	0.925	0.946	-2.3
0.8	0.791	0.803	-1.5
1	0	0	0.0

Table 4. 17 ANSYS and FLUX2D Static torque Results at 3A

X <sub>n</sub>	ANSYS 3A	FLUX2D 3A	ERR%
0	0	0	0.0
0.2	0.820	0.813	0.9
0.4	1.480	1.465	1.0
0.6	1.679	1.712	-2.0
0.8	1.390	1.416	-1.9
1	0	0	0.0

Table 4. 18 ANSYS and FLUX2D Flux linkage Results at 1A

$X_n$	ANSYS 1A	FLUX2D 1A	ERR%
0	0.269	0.270	-0.4
0.2	0.248	0.246	0.8
0.4	0.196	0.197	-0.5
0.6	0.141	0.144	-2.1
0.8	0.085	0.088	-3.5
1	0.065	0.067	-3.1

Table 4. 19 ANSYS and FLUX2D Flux linkage Results at 2A

$X_n$	ANSYS 2A	FLUX2D 2A	ERR%
0	0.398	0.403	-1.3
0.2	0.383	0.385	-0.5
0.4	0.327	0.328	-0.3
0.6	0.242	0.243	-0.4
0.8	0.169	0.171	-1.2
1	0.129	0.132	-2.3

Table 4. 20 ANSYS and FLUX2D Flux linkage Results at 3A

$X_n$	ANSYS 3A	FLUX2D 3A	ERR%
0	0.440	0.442	-0.5
0.2	0.421	0.422	-0.2
0.4	0.380	0.383	-0.8
0.6	0.309	0.313	-1.3
0.8	0.239	0.242	-1.3
1	0.194	0.197	-1.5

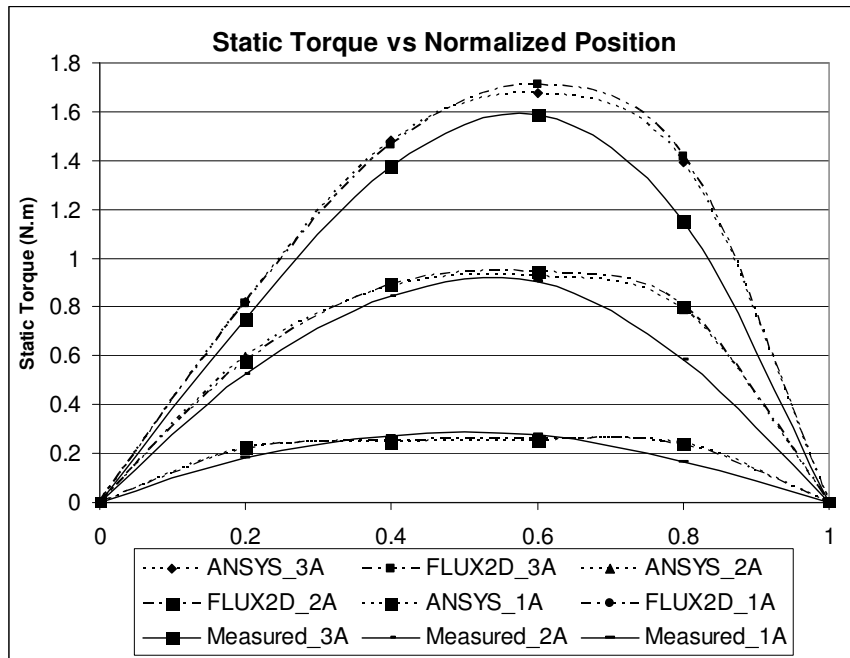


Figure 4. 20 Static Torque vs Normalized Position of SR2 (ANSYS & Flux2D)

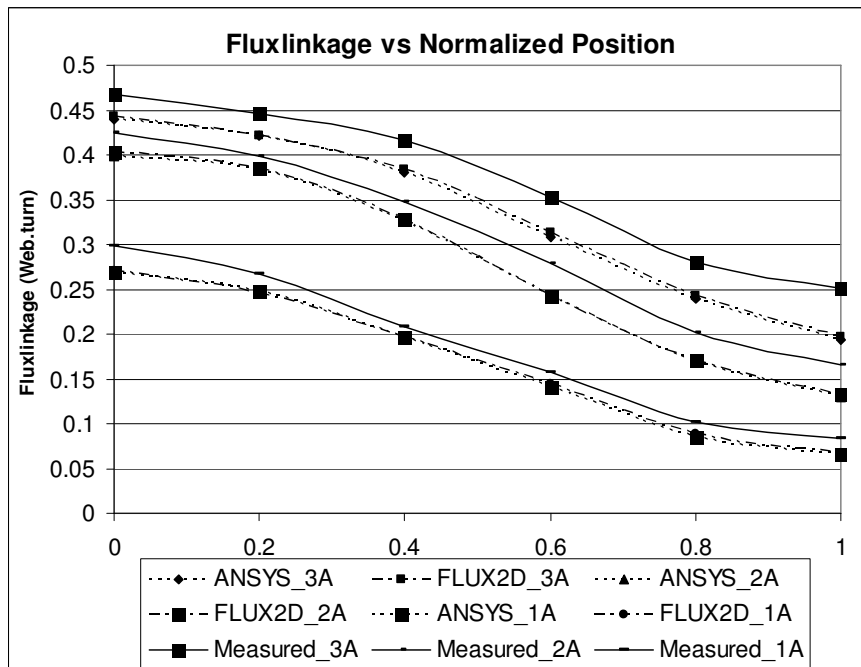


Figure 4. 21 Flux linkage vs Normalized Position of SR2 (ANSYS & Flux2D)



From this comparison, we can see that the percentage error between ANSYS and FLUX2D results is generally very small. This comparison assures us about the reliability of both ANSYS and FLUX2D results.

#### 4.3.1.9 Flux linkage prediction including End leakage effect.

One should remember that the author is solving two dimensional problems. This means that end leakage effect is not included in the results. A Software package developed by Goynük [21] is used to predict flux linkage data of SR2 and to include end leakage flux. Tables 4.21-4.23 show the measured flux linkage and both of ANSYS and FLUX2D predictions. The percentage error is also included and taken as the ratio of the difference between measured flux linkage and numerical results including endleakage correction to the measured value. Figures from 4.22 to 4.27 show the results for different rotor positions and excitation levels after including the end leakage effect.

Table 4. 21 Prediction of Flux linkage of SR2 at 1A including endleakage correction

$X_n$	Meas- ured 1A	ANSYS 2D 1A	ANSYS +endlkg 1A	FLUX 2D 1A	FLUX +endlkg 1A	ANSYS %ERR	FLUX %ERR
0	0.299	0.269	0.2693	0.270	0.2703	9.93	9.60
0.2	0.267	0.248	0.2517	0.246	0.2497	5.73	6.48
0.4	0.208	0.196	0.2021	0.197	0.2031	2.84	2.36
0.6	0.157	0.141	0.1550	0.144	0.1583	1.27	-0.83
0.8	0.102	0.085	0.1000	0.088	0.1035	1.96	-1.47
<b>1</b>	0.083	0.065	0.0885	0.067	0.0912	-6.63	-9.88

Table 4. 22 Prediction of Flux linkage of SR2 at 2A including endleakage correction

$X_n$	Meas- ured 2A	ANSYS 2D 2A	ANSYS +endlkg 2A	FLUX 2D 2A	FLUX +endlkg 2A	ANSYS %ERR	FLUX %ERR
0	0.425	0.398	0.3984	0.403	0.4034	6.26	5.08
0.2	0.398	0.383	0.388	0.385	0.3900	2.51	2.01
0.4	0.348	0.327	0.3377	0.328	0.3387	2.96	2.67
0.6	0.279	0.242	0.2671	0.243	0.2682	4.27	3.87
0.8	0.202	0.169	0.198	0.171	0.2003	1.98	0.84
<b>1</b>	0.165	0.129	0.1725	0.132	0.1765	-4.55	-6.97

Table 4. 23 Prediction of Flux linkage of SR2 at 3A including endleakage correction

$X_n$	Meas- ured 3A	ANSYS 2D 3A	ANSYS +endlkg 3A	FLUX 2D 3A	FLUX +endlkg 3A	ANSYS %ERR	FLUX %ERR
0	0.468	0.440	0.4404	0.442	0.4424	5.90	5.47
0.2	0.446	0.421	0.4262	0.422	0.4272	4.44	4.22
0.4	0.417	0.380	0.3922	0.383	0.3953	5.95	5.20
0.6	0.353	0.309	0.344	0.313	0.3485	2.55	1.27
0.8	0.280	0.239	0.2789	0.242	0.2824	0.39	-0.86
<b>1</b>	0.251	0.194	0.2545	0.197	0.2584	-1.39	-2.95

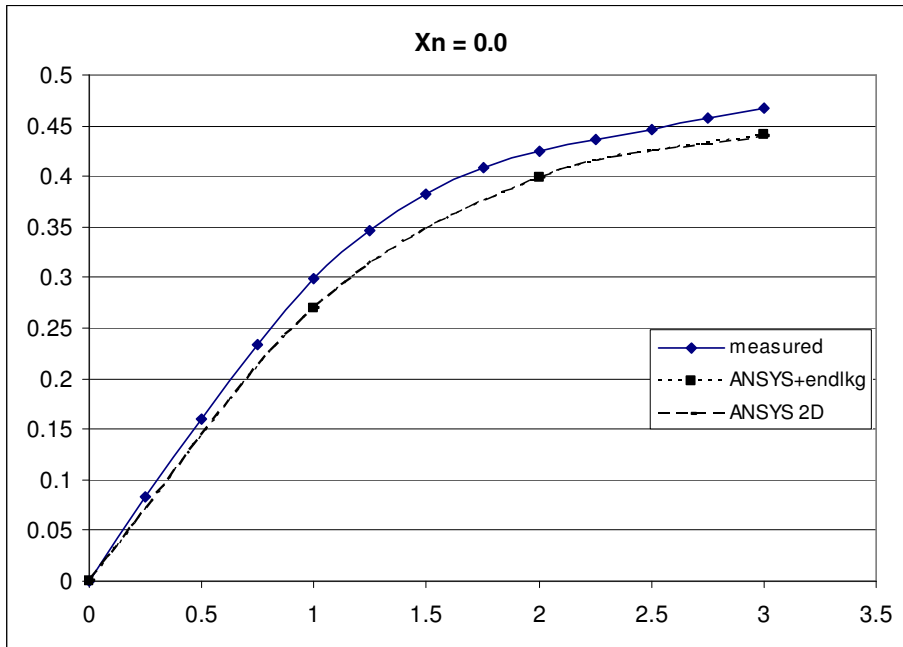


Figure 4. 22 Flux linkage (web. turn) against Current for Xn = 0.

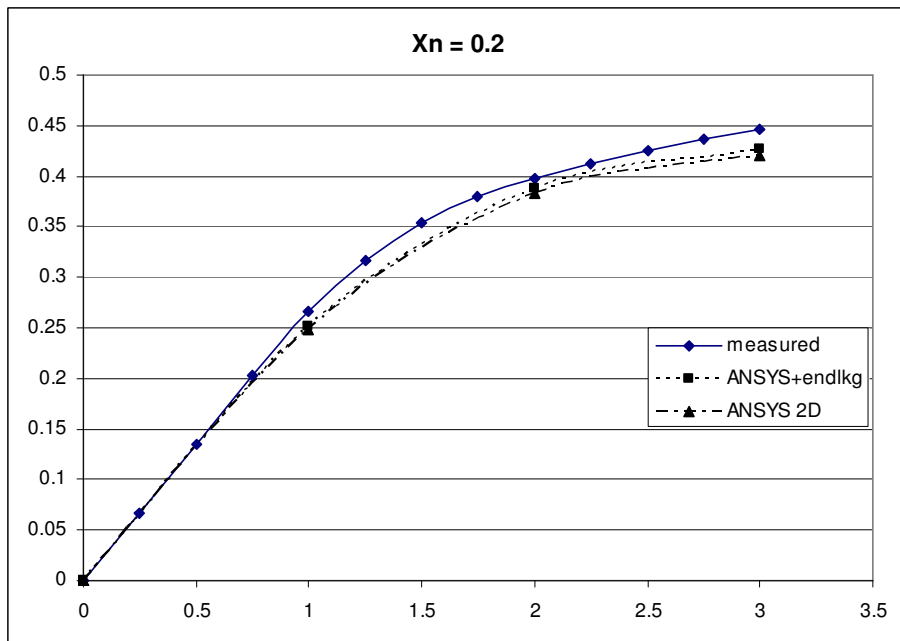


Figure 4. 23 Flux linkage (web. turn) against Current for Xn = 0.2.

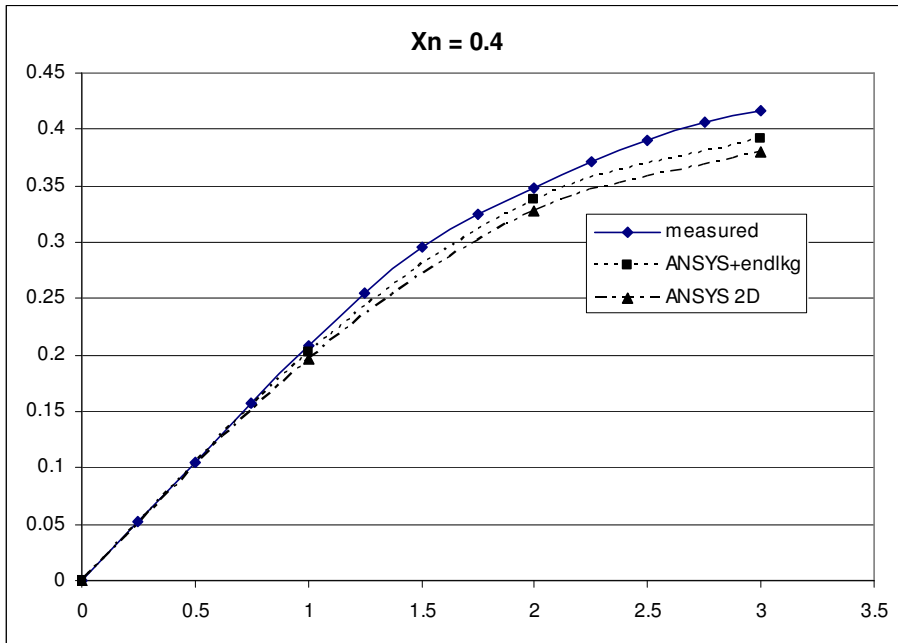


Figure 4. 24 Flux linkage (web. turn) against Current for  $X_n = 0.4$ .

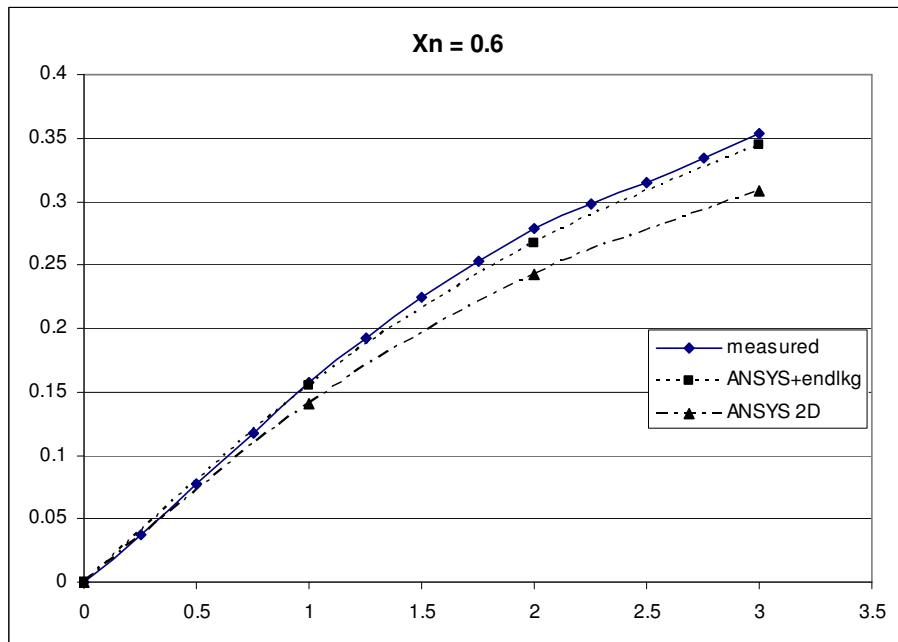


Figure 4. 25 Flux linkage (web. turn) against Current for  $X_n = 0.6$ .

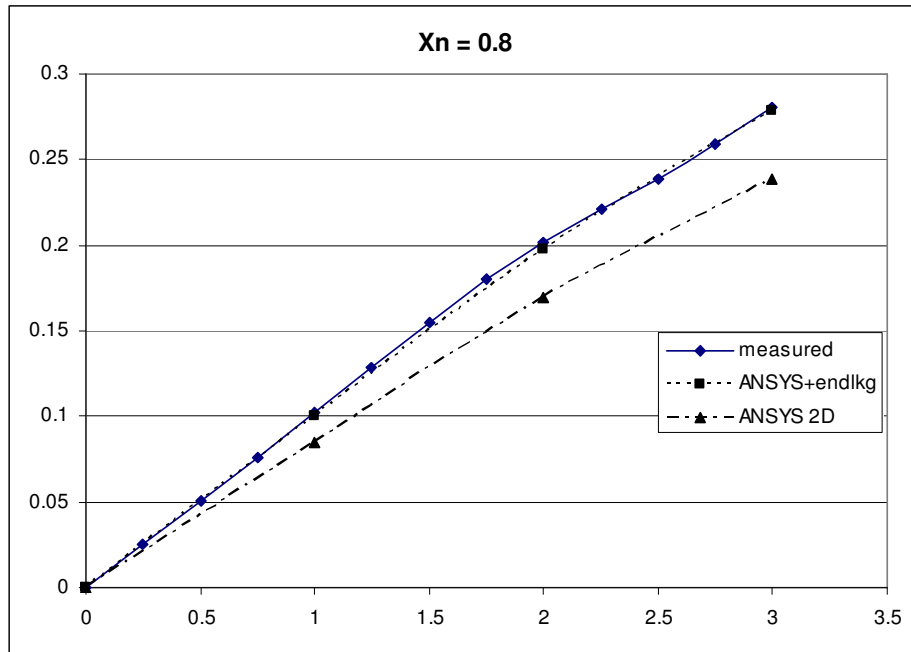


Figure 4. 26 Flux linkage (web. turn) against Current for  $X_n = 0.8$ .

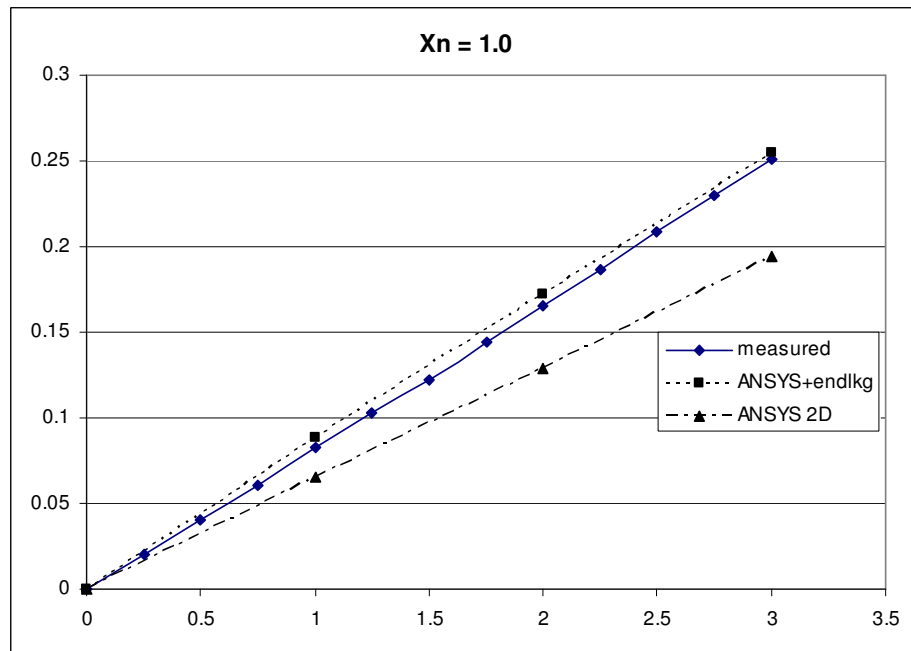


Figure 4. 27 Flux linkage (web. turn) against Current for  $X_n = 1$ .

In tables 4.21 to 4.23, the percentage error is reduced when the end leakage is included. Not only a reduction in the difference is obtained, but also the results of numerical solutions in some position are matching the measured flux linkage. The important conclusion here is that numerical solutions are convenient to depend on when solving a similar problem as the model introduced in chapter three.

## **4.3.2 SR1 Model**

### **4.3.2.1 SR1 Geometry**

Table-4.24 shows the dimensions of the second test motor, SR1, which has a rated current of 6A and 300 turns per phase ( $J = 7.44e6 \text{ A/m}^2$  for 4A). Figure-4.28 shows SR1 as modeled in ANSYS. In the previous sections, the author explained in details how he built the model of SR2, mesh, boundary conditions... The same procedure is followed to solve for SR1. In other words, the same BH-curve shown in table-3.1 is used. Dirichlet boundary condition is applied. Solution convergence, which is defined by equation 4.6, is set to be  $1e-5$  for SR1. In addition, the technique of shifting the rotor discussed in section 4.3.1.3 is also followed here, then after meshing the motor, dirichlet boundary condition is applied so that no flux exits from the domain.

Table 4. 24 dimensions of SR1[22]

Dimensions of SR1	Unit in mm
Rotor outer diameter, $d_o$	70
Rotor inner diameter, $d_i$	35
Stator outer diameter, $D_s$	135
Back Core thickness, $Y_b$	11
Stator pole width, $t_s$	8.5
Rotor tooth width, $t_r$	10
Airgap length, $g$	0.25
Rotor tooth depth, $h_r$	17.5
Stator pole depth, $h_s$	21.4
Core length, $L_c$	91.5
Coil length, $t_c$	12.8
Coil width, $t_d$	12.6

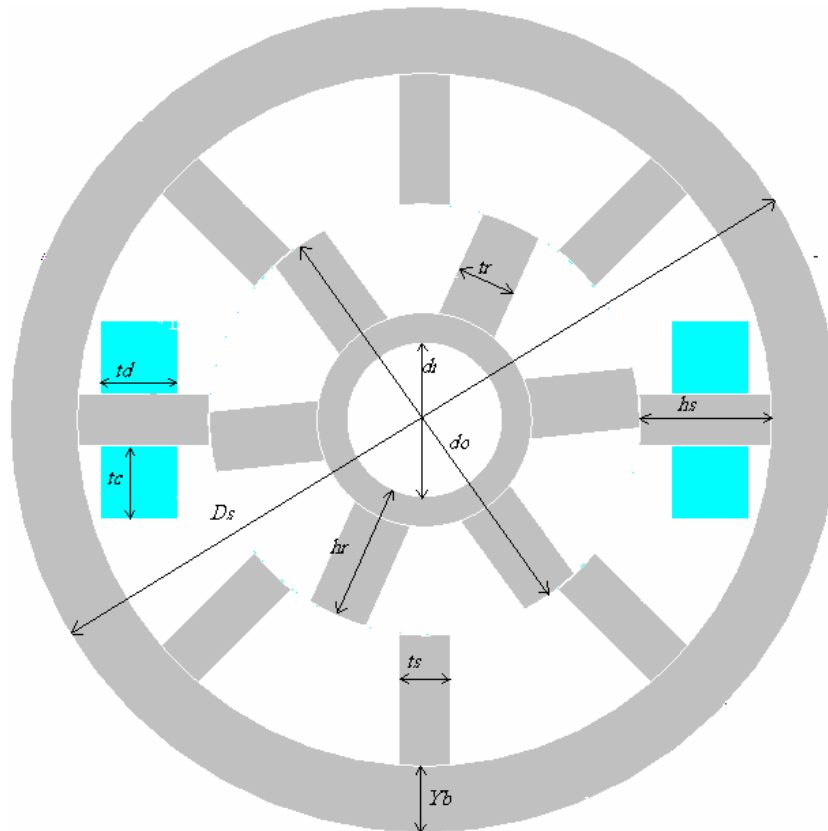


Figure 4. 28 SR1 Geometry at 6degrees (normalized position is 0.2)

#### **4.3.2.2 Mesh of SR1**

Figure-4.29 shows the complete, meshed geometry of SR1 using PLANE53 type discussed in section 4.3.1.2. The total number of nodes is 46,000. As seen in the figure, the air gap is meshed by very small elements while back core of stator has the largest elements. As seen from Figure-4.30 which shows the distribution of nodes in the airgap, five rows of nodes are placed in this region as performed in SR2. In addition, the author has meshed the teeth corresponding to phase A which is going to be excited with more elements than that for the other teeth.



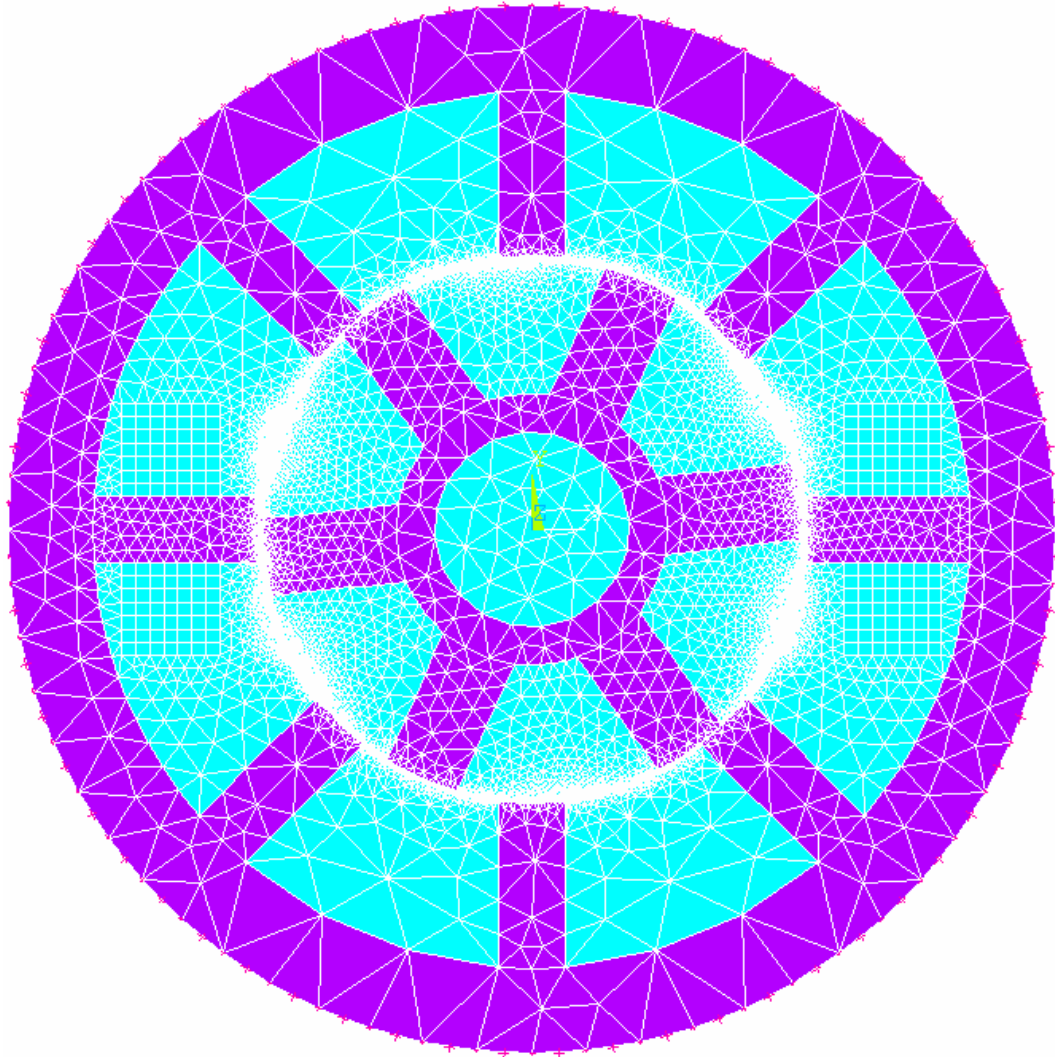


Figure 4. 29 Mesh of SR1 at 6degrees (normalized position is 0.2)

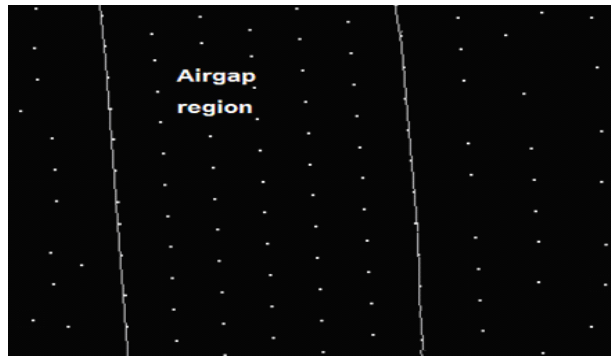


Figure 4. 30 Nodes distribution in the airgap region of SR1.

#### 4.3.2.3 Numerical Results of SR1:

The author has obtained the results of SR1 by solving at three levels of excitation; 4A, 3A and 2A in accordance with reference [22]. Solutions are obtained using both ANSYS and FLUX. Tables 4.25-4.27 show static torque results versus normalized position,  $X_n$ . Measured values and percentage error in prediction is also included in the table and calculated by using equation 4.8. In chapter three section 3.4.6, the author explained how he obtained motor torque. Figure-4.31 shows static torque-position curves for measurements and ANSYS only since as seen from the tables, the difference between numerical results obtained from ANSYS and FLUX is small and can't be seen when drawn together in the same graph. It is worth mentioning here that the time of solution was ranging between 45 and 53 seconds in both ANSYS and FLUX.

Table 4. 25 Static torque measurements and ANSYS results for SR1 at 2A

$X_n$	Measured 2A	ANSYS 2A	ERR%	FLUX 2A	ERR%
0	0	0	0.0	0	0.0
0.2	1.870	2.015	-7.8	1.988	-6.3
0.4	5.200	4.952	4.8	4.991	4.0
0.6	5.500	5.123	6.9	5.201	5.4
0.8	1.250	1.873	-49.8	1.885	-50.8
1	0	0	0.0	0	0.0

Table 4. 26 Static torque measurements and ANSYS results for SR1 at 3A

$X_n$	Measured 3A	ANSYS 3A	ERR%	FLUX 3A	ERR%
0	0	0	0.0	0	0.0
0.2	3.500	4.105	-17.3	4.214	-20.4
0.4	8.500	9.054	-6.5	9.150	-7.6
0.6	7.625	9.120	-19.6	9.250	-21.3
0.8	2.250	3.010	-33.8	3.055	-35.8
1	0	0	0.0	0	0.0

Table 4. 27 Static torque measurements and ANSYS results for SR1 at 4A

$X_n$	Measured 4A	ANSYS 4A	ERR%	FLUX 4A	ERR%
0	0	0	0.0	0	0.0
0.2	5.000	5.600	-12	5.650	-13.0
0.4	11.870	12.410	-4.5	12.480	-5.1
0.6	12.870	13.800	-7.2	13.950	-8.4
0.8	4.000	4.892	-22.3	4.960	-24.0
1	0	0	0.0	0	0.0

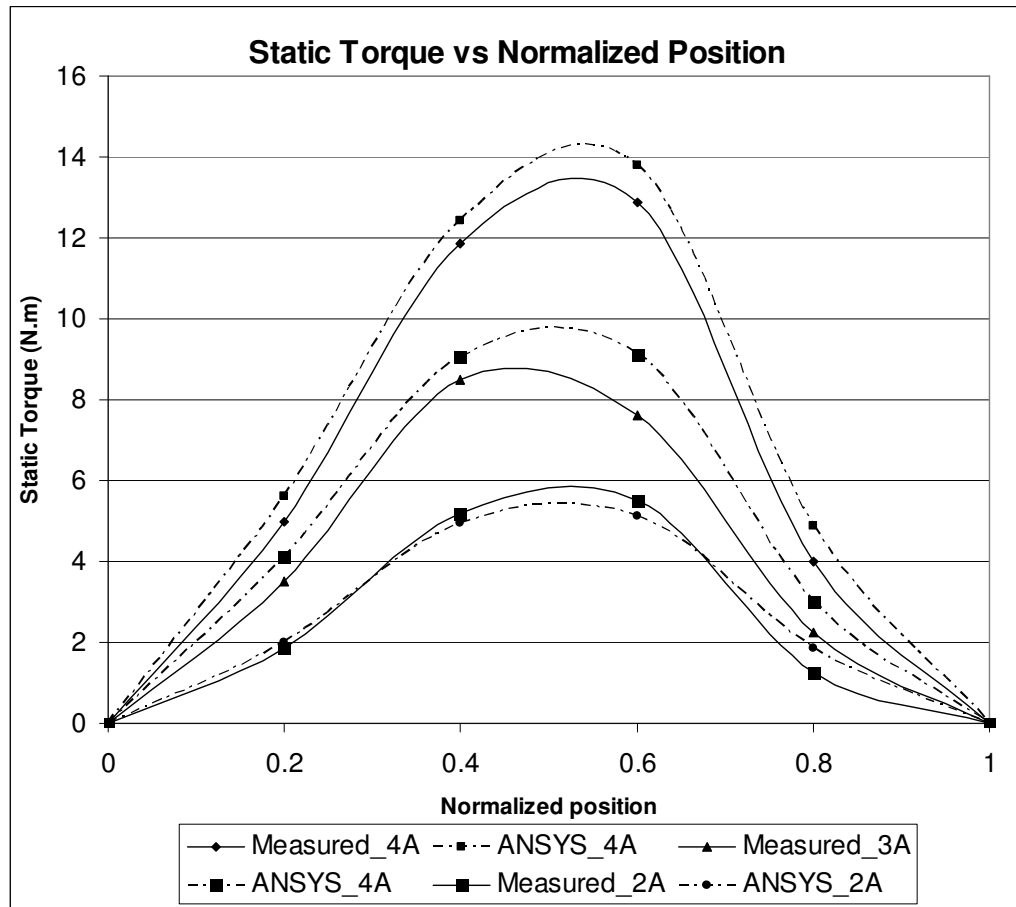


Figure 4. 31 Static Torque vs Normalized position for SR1 (4A).

As seen from figure-4.31, there is a difference between measured static torque and numerical results. In addition, percentage error increases as the rotor moves from IN position to the OUT position. This is probably because of the same reasons mentioned at the end of section 4.3.1.7.

The author also obtained fluxlinkage-position data as shown in tables 4.28-4.30 and drawn in figure-4.32 both for Measurements and ANSYS solutions.

Table 4. 28 Flux linkage Measurements and ANSYS results of SR1 at 2A

$X_n$	Measured 2A	ANSYS 2A	ERR%	FLUX 2A	ERR%
0	0.835	0.821	1.7	0.820	1.8
0.2	0.760	0.738	2.9	0.736	3.2
0.4	0.515	0.501	2.7	0.499	3.1
0.6	0.180	0.182	-1.1	0.180	0
0.8	0.120	0.110	8.3	0.109	9.2
1	0.100	0.095	5.0	0.092	8.0

Table 4. 29 Flux linkage Measurements and ANSYS results of SR1 at 3A

$X_n$	Measured 3A	ANSYS 3A	ERR%	FLUX 3A	ERR%
0	0.900	0.878	2.4	0.876	2.7
0.2	0.825	0.806	2.3	0.801	3.0
0.4	0.610	0.59	3.3	0.584	4.3
0.6	0.280	0.265	5.4	0.261	6.8
0.8	0.175	0.165	5.7	0.162	7.4
1	0.150	0.137	8.7	0.135	10.0

Table 4. 30 Flux linkage Measurements and ANSYS results of SR1 at 4A

$X_n$	Measured 4A	ANSYS 4A	ERR%	FLUX 4A	ERR%
0	0.938	0.915	2.5	0.913	2.7
0.2	0.875	0.835	4.6	0.831	5.0
0.4	0.675	0.659	2.4	0.655	2.9
0.6	0.380	0.351	7.6	0.347	8.7
0.8	0.230	0.218	5.2	0.215	6.5
1	0.190	0.174	8.4	0.173	8.9

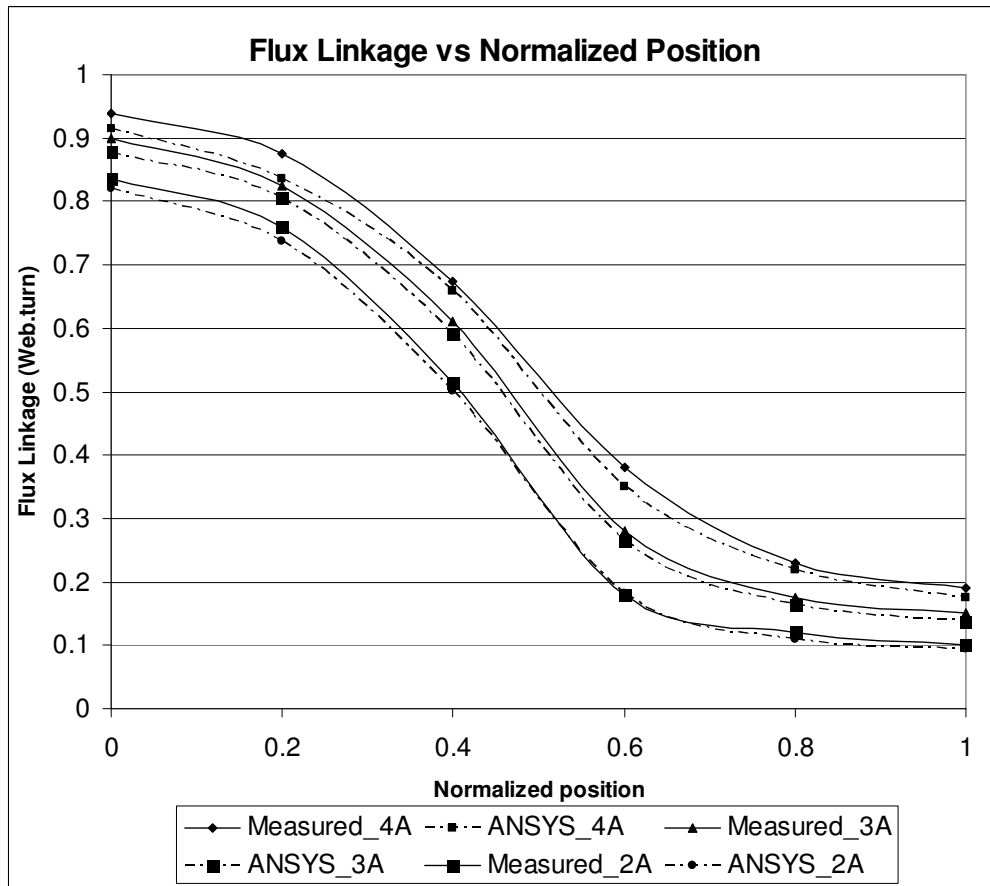


Figure 4. 32 Flux linkage vs Normalized position of SR1

By looking to tables 4.28-30 and comparing the results of ANSYS and FLUX, one can recognize that there is a very small difference between them, hence it is enough to include one of them in figure-4.32. However, there is a noticeable difference between numerical results and measurements. This difference is mainly, first, because of the errors while performing the experiments to take the flux linkage data. Second, the numerical solutions performed here is two-dimensional solutions, this means that the end leakage flux is not included. So, the same Software package developed by Goynük [21] is used to predict the end leakage flux. Table-4.31 includes the endleakage predictions together with the percentage error which is defined as shown in equation 4.10. Figure-4.33 shows the data introduced in table-4.31 in the form of graphs.

$$ERR\% = \frac{Measured - ANSYS_{ENDLKG}}{Measured} * 100\% \quad (4.10)$$

Table 4. 31 Prediction of Flux linkage of SR1 including endleakage correction

$X_n$	ANSYS +endlkg 2A	%ERR 2A	ANSYS +endlkg 3A	%ERR 3A	ANSYS +endlkg 4A	%ERR 4A
0	0.822	1.56	0.879	2.33	0.917	2.24
0.2	0.739	2.76	0.809	1.94	0.842	3.78
0.4	0.505	1.94	0.598	1.97	0.659	2.37
0.6	0.183	-1.67	0.272	2.86	0.371	2.37
0.8	0.116	3.33	0.171	2.29	0.227	1.30
<b>1</b>	0.102	-2.0	0.152	-1.33	0.181	4.74

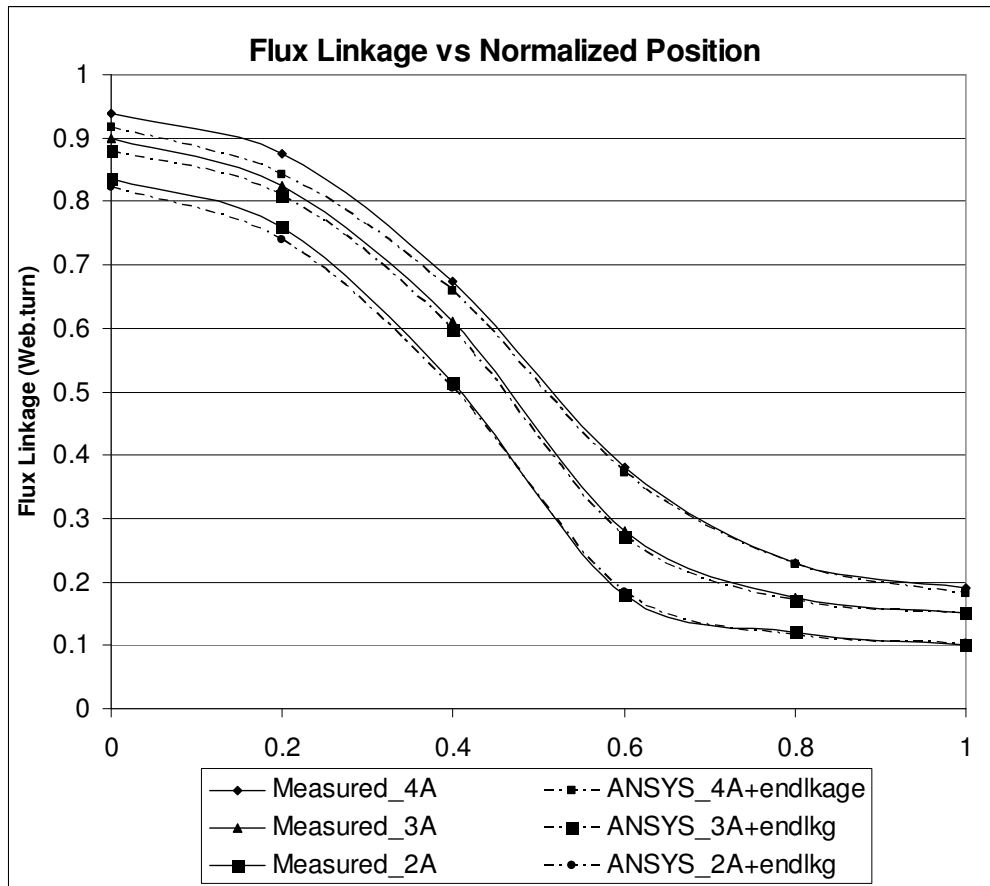


Figure 4. 33 Flux linkage vs Normalized position SR1 Including end effect.

From table-4.17, it is clear that the percentage error, including end leakage flux is less than that for the results of two dimensional solutions. Here it can be seen that end leakage flux is increasing as the rotor moves from aligned position to OUT position.

By this section, the author has completed the analysis of two test motors; SR2 and SR1 and obtained static torque and flux linkage data for both of them. These test motors have been analyzed by ANSYS-11.0 and FLUX-8.1 as a way to verify the model introduced in chapter 3 to show that numerical results can be reliable.



#### 4.4 Conclusion

In this chapter the author has tested accuracy of finite element results by, first, comparison of analytically calculated permeance with numerical computations. The results of finite element analysis match precisely the analytically calculated permeance. Second, the author has solved the magnetic field for two test motors. The torque-position and inductance vs position characteristics of these test motors are predicted from the field solution results. Next torque and inductance measurement results on these two motors [11], [21], are compared with computed results. It is found that the general shape of the torque curves is well predicted. However, error in predictions are found to reach large values especially at large displacement positions where measuring the torque is very position sensitive. Inductance predictions are found to be quite accurate especially when the FE results are corrected for end winding effect.

As a result, it can be stated that the FE solution can be reliably used for the computation of force and induction comparison of doubly-salient magnetic circuits.

## CHAPTER 5

### TABLE OF NORMALIZED DATA

#### 5.1 Introduction

The purpose of this thesis is to produce a set of normalized normal force, tangential force, and permeance variation data. As discussed earlier, using this data it is expected that designers will be able to analyze a given switch reluctance motor to obtain its torque-position curve for a chosen current level or they can obtain permeance-current-position curves. It is shown earlier that such data can be used to predict torque-speed curve of a given doubly salient motor [21]. In chapter three of this thesis a model is developed by means of which such data can be produced. In the following chapter, i.e. ch.4, the model and finite element software used for producing the data is tested against analytically obtained permeance for doubly salient structures. Also predictions of force and permeance are made for two test motors and compared with experimental data to assure that the model and the solution approach can be reliably used for predicting force and permeance variation.

In this chapter, normal force, tangential force, and permeance variation against position and current is generated and presented. The range of the data is as follows:

$\lambda/g$  : 40, 70, 100, 150, 200 and 250

at  $t/\lambda$  : 0.3, 0.4 and 0.5

$X_n$  : 0.0(IN), 0.2, 0.4, 0.6, 0.8, and 1.0 (OUT).

The maximum excitation level in the simulations is chosen so that tooth flux density levels that may be encountered in practice are covered. The applied MMF for each solution may be found in the tables presented.

## 5.2 Table of Normalized Data

In chapter 3, the author has introduced the model used to generate the normalized data. The length of the model is chosen to be one meter, and the tooth pitch ( $\lambda$ ) is set to be 17.2 mm. This data is presented in Table 5.1 and the data for  $\lambda/g = 40$  is also plotted on figures 5.1 to 5.16. FLUX 8.1 is mainly used to solve the model for a range of dimensions and excitation levels as presented in the table. ANSYS 11.0 is also used to verify the results of FLUX and it is found that the difference in the results is no more than one percent as stated in section 3.5.5.

For each solution presented in the table the MMF (in Amp.turn) is specified and the following parameters are calculated:

The tangential force,  $F_t$ , acting on the centered tooth (in Newton),

The normal force,  $F_n$ , acting on the centered tooth (in Newton),

The normalized permeance,  $P_n$ , for a tooth pitch,

The tooth flux density,  $B_t$ , (in Tesla).

This set of normalized data will be applied to the software package, developed by Goynük [21], to predict static torque curves and flux linkage curves as a function of position and excitation level for the test motors presented in chapter four. After then, these predictions will be compared with the results of numerical solutions.

Table 5. 1 Normalized Data

$\lambda/g = 40, t/\lambda = 0.3, X_n = \text{IN}$				
$N^*I$	$F_t$	$F_n$	$P_n$	$B_t$
302	0	1610	0.361	1.062
481	0	3185	0.319	1.495
825	0	4410	0.221	1.774
1235	0	5210	0.161	1.938

$\lambda/g = 40, t/\lambda = 0.3, X_n = 0.4$				
$N^*I$	$F_t$	$F_n$	$P_n$	$B_t$
302	112.1	676	0.220	0.648
481	282.6	1630	0.212	0.993
825	722.6	3016	0.182	1.465
1235	1068.3	3710	0.143	1.723

$\lambda/g = 40, t/\lambda = 0.4, X_n = \text{IN}$				
$N^*I$	$F_t$	$F_n$	$P_n$	$B_t$
302	0	2120	0.457	1.008
481	0	4450	0.416	1.461
825	0	6280	0.289	1.744
1235	0	7425	0.211	1.905

$\lambda/g = 40, t/\lambda = 0.4, X_n = 0.4$				
$N^*I$	$F_t$	$F_n$	$P_n$	$B_t$
302	108.3	1186	0.3144	0.694
481	273.9	2904	0.3092	1.086
825	680.1	5203	0.2514	1.515
1235	1036.4	6086	0.1900	1.714

$\lambda/g = 40, t/\lambda = 0.5, X_n = \text{IN}$				
$N^*I$	$F_t$	$F_n$	$P_n$	$B_t$
302	0	2640	0.552	0.975
481	0	5740	0.512	1.439
825	0	8170	0.357	1.721
1235	0	9710	0.261	1.883

$\lambda/g = 40, t/\lambda = 0.5, X_n = 0.4$				
$N^*I$	$F_t$	$F_n$	$P_n$	$B_t$
302	108.3	1689	0.4135	0.730
481	272.5	4140	0.406	1.142
825	648.4	7338	0.3225	1.555
1235	994.9	8486	0.239	1.728

$\lambda/g = 40, t/\lambda = 0.3, X_n = 0.2$				
$N^*I$	$F_t$	$F_n$	$P_n$	$B_t$
302	102.9	1173	0.302	0.890
481	249.6	2767	0.292	1.367
825	427.2	4220	0.213	1.711
1235	594.2	5595	0.159	1.910

$\lambda/g = 40, t/\lambda = 0.3, X_n = 0.6$				
$N^*I$	$F_t$	$F_n$	$P_n$	$B_t$
302	102.1	176	0.136	0.4
481	249.5	423	0.134	0.631
825	625.1	1031	0.13	1.04
1235	1085.6	1794	0.121	1.458

$\lambda/g = 40, t/\lambda = 0.4, X_n = 0.2$				
$N^*I$	$F_t$	$F_n$	$P_n$	$B_t$
302	101.8	1683	0.398	0.879
481	247.6	3985	0.385	1.354
825	425.8	6110	0.281	1.690
1235	585.2	7375	0.209	1.880

$\lambda/g = 40, t/\lambda = 0.4, X_n = 0.6$				
$N^*I$	$F_t$	$F_n$	$P_n$	$B_t$
302	111.7	694	0.234	0.516
481	276.7	1674	0.229	0.806
825	732.9	3160	0.198	1.194
1235	1247.2	4256	0.168	1.511

$\lambda/g = 40, t/\lambda = 0.5, X_n = 0.2$				
$N^*I$	$F_t$	$F_n$	$P_n$	$B_t$
302	100.4	2185	0.494	0.873
481	244.6	5216	0.479	1.347
825	424.2	8020	0.348	1.680
1235	604.7	9665	0.258	1.860

$\lambda/g = 40, t/\lambda = 0.5, X_n = 0.6$				
$N^*I$	$F_t$	$F_n$	$P_n$	$B_t$
302	106.1	1205	0.335	0.591
481	268.1	2939	0.329	0.925
825	709.3	5407	0.274	1.322
1235	1175.8	6603	0.217	1.566

Table 5.1 Cont'd

$\lambda g = 40, t/\lambda = 0.3, X_n = 0.8$				
$N^*I$	$F_t$	$F_n$	$P_n$	$B_t$
302	19.48	46.5	0.099	0.292
481	49.40	119	0.099	0.465
825	144.6	351	0.099	0.800
1235	318.4	781	0.0987	1.190

$\lambda g = 70, t/\lambda = 0.3, X_n = IN$				
$N^*I$	$F_t$	$F_n$	$P_n$	$B_t$
175	0	1580	0.332	0.991
220	0	2400	0.327	1.226
470	0	4330	0.206	1.653
707	0	5060	0.149	1.800

$\lambda g = 40, t/\lambda = 0.4, X_n = 0.8$				
$N^*I$	$F_t$	$F_n$	$P_n$	$B_t$
302	95.2	178	0.151	0.333
481	234.2	435	0.15	0.5265
825	601.8	1106	0.1459	0.878
1235	1093.7	2066	0.1398	1.260

$\lambda g = 70, t/\lambda = 0.4, X_n = IN$				
$N^*I$	$F_t$	$F_n$	$P_n$	$B_t$
175	0	1610	0.428	0.957
220	0	3210	0.422	1.188
470	0	6050	0.272	1.635
707	0	7080	0.197	1.776

$\lambda g = 40, t/\lambda = 0.5, X_n = 0.8$				
$N^*I$	$F_t$	$F_n$	$P_n$	$B_t$
302	93.5	710	0.258	0.455
481	236.2	1712	0.253	0.711
825	613.5	3276	0.222	1.070
1235	993.3	4544	0.192	1.389

$\lambda g = 70, t/\lambda = 0.5, X_n = IN$				
$N^*I$	$F_t$	$F_n$	$P_n$	$B_t$
175	0	2600	0.523	0.937
220	0	4020	0.517	1.163
470	0	7790	0.338	1.624
707	0	9130	0.244	1.763

$\lambda g = 40, t/\lambda = 0.3, X_n = OUT$				
$N^*I$	$F_t$	$F_n$	$P_n$	$B_t$
302	0	37	0.092	0.272
481	0	95	0.092	0.433
825	0	278	0.092	0.742
1235	0	624	0.092	1.111

$\lambda g = 70, t/\lambda = 0.3, X_n = 0.2$				
$N^*I$	$F_t$	$F_n$	$P_n$	$B_t$
175	66.7	1153	0.267	0.796
220	105.4	1810	0.266	1.000
470	308	4315	0.195	1.565
707	440	5030	0.143	1.728

$\lambda g = 40, t/\lambda = 0.4, X_n = OUT$				
$N^*I$	$F_t$	$F_n$	$P_n$	$B_t$
302	0	59	0.123	0.272
481	0	150	0.123	0.433
825	0	443	0.123	0.742
1235	0	987	0.122	1.107

$\lambda g = 70, t/\lambda = 0.4, X_n = 0.2$				
$N^*I$	$F_t$	$F_n$	$P_n$	$B_t$
175	66.3	1680	0.364	0.814
220	104.8	2640	0.363	1.022
470	295.7	6130	0.262	1.571
707	417.3	7180	0.191	1.723

$\lambda g = 40, t/\lambda = 0.5, X_n = OUT$				
$N^*I$	$F_t$	$F_n$	$P_n$	$B_t$
302	0	330	0.210	0.371
481	0	790	0.207	0.583
825	0	1885	0.197	0.950
1235	0	3240	0.183	1.318

$\lambda g = 70, t/\lambda = 0.5, X_n = 0.2$				
$N^*I$	$F_t$	$F_n$	$P_n$	$B_t$
175	68	2261	0.467	0.836
220	107	3562	0.466	1.049
470	291	7973	0.328	1.579
707	406	9334	0.238	1.723

Table 5.1 Cont'd

$\lambda g = 70, t/\lambda = 0.3, X_n = 0.4$				
$N^*I$	$F_t$	$F_n$	$P_n$	$B_t$
175	71.5	645	0.180	0.536
220	112.9	1010	0.179	0.671
469	462.5	2725	0.148	1.180
707	810.0	3380	0.119	1.439

$\lambda g = 70, t/\lambda = 0.3, X_n = 0.8$				
$N^*I$	$F_t$	$F_n$	$P_n$	$B_t$
175	7.5	16	0.0586	0.175
220	18.5	35	0.0585	0.274
470	53.8	102	0.0584	0.468
707	121.2	230	0.0583	0.703

$\lambda g = 70, t/\lambda = 0.4, X_n = 0.4$				
$N^*I$	$F_t$	$F_n$	$P_n$	$B_t$
175	69.7	1172	0.277	0.621
220	110.2	1843	0.276	0.779
470	447.1	4983	0.221	1.328
707	749.6	5776	0.168	1.507

$\lambda g = 70, t/\lambda = 0.4, X_n = 0.8$				
$N^*I$	$F_t$	$F_n$	$P_n$	$B_t$
175	62.9	104	0.0980	0.219
275	151.4	245	0.0977	0.343
470	371.8	582	0.0941	0.566
707	660.0	1032	0.0900	0.813

$\lambda g = 70, t/\lambda = 0.5, X_n = 0.4$				
$N^*I$	$F_t$	$F_n$	$P_n$	$B_t$
175	71	1746	0.379	0.679
220	112	2748	0.379	0.852
470	428	7132	0.293	1.409
707	696	8181	0.216	1.561

$\lambda g = 70, t/\lambda = 0.5, X_n = 0.8$				
$N^*I$	$F_t$	$F_n$	$P_n$	$B_t$
175	66	671	0.204	0.365
275	161	1570	0.200	0.563
470	420	2828	0.171	0.820
707	725	3621	0.144	1.040

$\lambda g = 70, t/\lambda = 0.3, X_n = 0.6$				
$N^*I$	$F_t$	$F_n$	$P_n$	$B_t$
175	65.4	102	0.089	0.265
275	156.1	239	0.088	0.412
470	388.6	571	0.085	0.679
707	698.5	1010	0.081	0.971

$\lambda g = 70, t/\lambda = 0.3, X_n = \text{OUT}$				
$N^*I$	$F_t$	$F_n$	$P_n$	$B_t$
175	0	11	0.054	0.161
220	0	20	0.054	0.203
470	0	91	0.054	0.433
707	0	208	0.054	0.652

$\lambda g = 70, t/\lambda = 0.4, X_n = 0.6$				
$N^*I$	$F_t$	$F_n$	$P_n$	$B_t$
175	71.2	648	0.188	0.420
275	176.4	1533	0.184	0.650
470	466.2	2743	0.156	0.934
707	833.1	3448	0.129	1.163

$\lambda g = 70, t/\lambda = 0.4, X_n = \text{OUT}$				
$N^*I$	$F_t$	$F_n$	$P_n$	$B_t$
175	0	19	0.073	0.163
220	0	31	0.073	0.205
470	0	143	0.073	0.439
707	0	342	0.073	0.660

$\lambda g = 70, t/\lambda = 0.5, X_n = 0.6$				
$N^*I$	$F_t$	$F_n$	$P_n$	$B_t$
175	71	1206	0.290	0.520
275	173	2857	0.285	0.801
470	452	5084	0.232	1.117
707	808	6021	0.181	1.310

$\lambda g = 70, t/\lambda = 0.5, X_n = \text{OUT}$				
$N^*I$	$F_t$	$F_n$	$P_n$	$B_t$
175	0	197	0.141	0.251
220	0	307	0.140	0.314
470	0	1090	0.132	0.638
707	0	1890	0.125	0.902

Table 5.1 Cont'd

$\lambda/g = 100, t/\lambda = 0.3, X_n = \text{IN}$				
$N^*I$	$F_t$	$F_n$	$P_n$	$B_t$
125	0	1580	0.317	0.966
200	0	3310	0.287	1.398
350	0	4380	0.190	1.617
525	0	5050	0.136	1.744

$\lambda/g = 100, t/\lambda = 0.3, X_n = 0.4$				
$N^*I$	$F_t$	$F_n$	$P_n$	$B_t$
125	51.2	612	0.157	0.479
200	131	1494	0.154	0.751
350	365	2657	0.127	1.071
525	649	3203	0.101	1.288

$\lambda/g = 100, t/\lambda = 0.4, X_n = \text{IN}$				
$N^*I$	$F_t$	$F_n$	$P_n$	$B_t$
125	0	2100	0.412	0.940
200	0	4500	0.377	1.377
350	0	6080	0.251	1.604
525	0	6980	0.180	1.726

$\lambda/g = 100, t/\lambda = 0.4, X_n = 0.4$				
$N^*I$	$F_t$	$F_n$	$P_n$	$B_t$
125	52.1	1142	0.253	0.578
200	132	2795	0.248	0.907
350	355	4927	0.195	1.248
525	625	5676	0.148	1.415

$\lambda/g = 100, t/\lambda = 0.5, X_n = \text{IN}$				
$N^*I$	$F_t$	$F_n$	$P_n$	$B_t$
125	0	2620	0.506	0.925
200	0	5700	0.467	1.365
350	0	7790	0.312	1.597
525	0	8930	0.223	1.714

$\lambda/g = 100, t/\lambda = 0.5, X_n = 0.4$				
$N^*I$	$F_t$	$F_n$	$P_n$	$B_t$
125	51.4	1663	0.349	0.637
200	130	4094	0.342	1.000
350	339	7061	0.263	1.345
525	565	8051	0.193	1.483

$\lambda/g = 100, t/\lambda = 0.3, X_n = 0.2$				
$N^*I$	$F_t$	$F_n$	$P_n$	$B_t$
125	49.4	1120	0.246	0.748
200	122	2720	0.239	1.165
350	254	4390	0.176	1.504
525	372	5080	0.129	1.652

$\lambda/g = 100, t/\lambda = 0.3, X_n = 0.6$				
$N^*I$	$F_t$	$F_n$	$P_n$	$B_t$
125	47.5	74	0.066	0.201
200	118	178	0.066	0.319
350	304	430	0.063	0.539
525	546	744	0.060	0.772

$\lambda/g = 100, t/\lambda = 0.4, X_n = 0.2$				
$N^*I$	$F_t$	$F_n$	$P_n$	$B_t$
125	50.5	1642	0.340	0.777
200	123	3963	0.330	1.207
350	237	6143	0.237	1.518
525	340	7134	0.173	1.657

$\lambda/g = 100, t/\lambda = 0.4, X_n = 0.6$				
$N^*I$	$F_t$	$F_n$	$P_n$	$B_t$
125	52.3	618	0.163	0.373
200	135	1508	0.160	0.584
350	369	2675	0.131	0.838
525	661	3252	0.106	1.021

$\lambda/g = 100, t/\lambda = 0.5, X_n = 0.2$				
$N^*I$	$F_t$	$F_n$	$P_n$	$B_t$
125	51.2	2162	0.434	0.793
200	124	5193	0.421	1.229
350	227	7874	0.298	1.523
525	321	9165	0.216	1.657

$\lambda/g = 100, t/\lambda = 0.5, X_n = 0.6$				
$N^*I$	$F_t$	$F_n$	$P_n$	$B_t$
125	54.1	1151	0.261	0.476
200	136.3	2822	0.256	0.748
350	374	4978	0.203	1.037
525	681	5760	0.156	1.195

Table 5.1 Cont'd

$\lambda g = 100, t/\lambda = 0.3, X_n = 0.8$				
$N^*I$	$F_t$	$F_n$	$P_n$	$B_t$
125	4.0	9.5	0.041	0.125
200	10	21	0.041	0.201
350	33	66	0.041	0.351
525	74.5	149	0.041	0.525

$\lambda g = 150, t/\lambda = 0.3, X_n = IN$				
$N^*I$	$F_t$	$F_n$	$P_n$	$B_t$
90	0	1750	0.301	0.991
150	0	3540	0.257	1.411
250	0	4350	0.172	1.570
380	0	4950	0.121	1.682

$\lambda g = 100, t/\lambda = 0.4, X_n = 0.8$				
$N^*I$	$F_t$	$F_n$	$P_n$	$B_t$
125	47	74	0.073	0.166
200	119	179	0.072	0.264
350	311	440	0.070	0.446
525	563	775	0.067	0.642

$\lambda g = 150, t/\lambda = 0.4, X_n = IN$				
$N^*I$	$F_t$	$F_n$	$P_n$	$B_t$
90	0	2330	0.394	0.972
150	0	4820	0.341	1.400
250	0	5960	0.228	1.559
380	0	6790	0.160	1.669

$\lambda g = 100, t/\lambda = 0.5, X_n = 0.8$				
$N^*I$	$F_t$	$F_n$	$P_n$	$B_t$
125	49.8	620	0.174	0.318
200	128	1510	0.171	0.499
350	255	2692	0.142	0.724
525	633	3285	0.117	0.897

$\lambda g = 150, t/\lambda = 0.5, X_n = IN$				
$N^*I$	$F_t$	$F_n$	$P_n$	$B_t$
90	0	2910	0.487	0.960
150	0	6100	0.423	1.391
250	0	7570	0.283	1.553
380	0	8650	0.200	1.662

$\lambda g = 100, t/\lambda = 0.3, X_n = OUT$				
$N^*I$	$F_t$	$F_n$	$P_n$	$B_t$
125	0	7	0.038	0.116
200	0	16	0.038	0.186
350	0	50	0.038	0.326
525	0	116	0.038	0.489

$\lambda g = 150, t/\lambda = 0.3, X_n = 0.2$				
$N^*I$	$F_t$	$F_n$	$P_n$	$B_t$
90	38.3	1240	0.227	0.748
150	102	3080	0.216	1.182
250	200	4500	0.159	1.453
380	304	5110	0.114	1.587

$\lambda g = 100, t/\lambda = 0.4, X_n = OUT$				
$N^*I$	$F_t$	$F_n$	$P_n$	$B_t$
125	0	12	0.052	0.118
200	0	34	0.052	0.189
350	0	98	0.052	0.331
525	0	220	0.052	0.497

$\lambda g = 150, t/\lambda = 0.4, X_n = 0.2$				
$N^*I$	$F_t$	$F_n$	$P_n$	$B_t$
90	37.3	1820	0.320	0.790
150	98.6	4460	0.301	1.238
250	178	6190	0.251	1.473
380	267	7170	0.154	1.606

$\lambda g = 100, t/\lambda = 0.5, X_n = OUT$				
$N^*I$	$F_t$	$F_n$	$P_n$	$B_t$
125	0	142	0.107	0.195
200	0	345	0.105	0.309
350	0	832	0.101	0.517
525	0	1430	0.095	0.731

$\lambda g = 150, t/\lambda = 0.5, X_n = 0.2$				
$N^*I$	$F_t$	$F_n$	$P_n$	$B_t$
90	38	2400	0.413	0.816
150	98	5820	0.386	1.268
250	168	7850	0.271	1.484
380	244	9110	0.194	1.613



Table 5.1 Cont'd

$\lambda g = 150, t/\lambda = 0.3, X_n = 0.4$				
$N^*I$	$F_t$	$F_n$	$P_n$	$B_t$
90	41	667	0.139	0.458
150	111	1700	0.134	0.734
250	273	2620	0.106	0.969
380	496	3050	0.083	1.146

$\lambda g = 150, t/\lambda = 0.3, X_n = 0.8$				
$N^*I$	$F_t$	$F_n$	$P_n$	$B_t$
90	2.1	4.4	0.028	0.091
150	5.8	9.1	0.028	0.152
250	17	26	0.028	0.253
380	40	71	0.027	0.385

$\lambda g = 150, t/\lambda = 0.4, X_n = 0.4$				
$N^*I$	$F_t$	$F_n$	$P_n$	$B_t$
90	39.5	1270	0.234	0.576
150	108	2900	0.223	0.919
250	264	4880	0.171	1.173
380	478	5560	0.127	1.320

$\lambda g = 150, t/\lambda = 0.4, X_n = 0.8$				
$N^*I$	$F_t$	$F_n$	$P_n$	$B_t$
90	38	55	0.052	0.128
150	101	141	0.051	0.211
250	236	310	0.050	0.341
380	428	543	0.048	0.496

$\lambda g = 150, t/\lambda = 0.5, X_n = 0.4$				
$N^*I$	$F_t$	$F_n$	$P_n$	$B_t$
90	39	1850	0.327	0.646
150	107	4660	0.312	1.026
250	254	7000	0.235	1.286
380	446	7980	0.170	1.419

$\lambda g = 150, t/\lambda = 0.5, X_n = 0.8$				
$N^*I$	$F_t$	$F_n$	$P_n$	$B_t$
90	39	684	0.151	0.298
150	108	1720	0.145	0.478
250	267	2640	0.117	0.641
380	485	3100	0.093	0.778

$\lambda g = 150, t/\lambda = 0.3, X_n = 0.6$				
$N^*I$	$F_t$	$F_n$	$P_n$	$B_t$
90	37	54	0.047	0.156
150	99	136	0.047	0.257
250	231	300	0.045	0.414
380	417	520	0.043	0.600

$\lambda g = 150, t/\lambda = 0.3, X_n = \text{OUT}$				
$N^*I$	$F_t$	$F_n$	$P_n$	$B_t$
90	0	3.5	0.027	0.084
150	0	9	0.026	0.141
250	0	24	0.026	0.234
380	0	61	0.026	0.356

$\lambda g = 150, t/\lambda = 0.4, X_n = 0.6$				
$N^*I$	$F_t$	$F_n$	$P_n$	$B_t$
90	40	677	0.144	0.354
150	111	1710	0.138	0.567
250	273	2620	0.110	0.752
380	498	3060	0.086	0.898

$\lambda g = 150, t/\lambda = 0.4, X_n = \text{OUT}$				
$N^*I$	$F_t$	$F_n$	$P_n$	$B_t$
90	0	5.5	0.035	0.086
150	0	16	0.035	0.144
250	0	43	0.035	0.239
380	0	99	0.035	0.363

$\lambda g = 150, t/\lambda = 0.5, X_n = 0.6$				
$N^*I$	$F_t$	$F_n$	$P_n$	$B_t$
90	40.8	1280	0.239	0.472
150	112	3230	0.229	0.753
250	274	4910	0.176	0.967
380	506	5600	0.132	1.098

$\lambda g = 150, t/\lambda = 0.5, X_n = \text{OUT}$				
$N^*I$	$F_t$	$F_n$	$P_n$	$B_t$
90	0	106	0.078	0.153
150	0	272	0.077	0.253
250	0	598	0.074	0.403
380	0	1040	0.069	0.578

Table 5.1 Cont'd

$\lambda g = 200, t/\lambda = 0.3, X_n = \text{IN}$				
$N^*I$	$F_t$	$F_n$	$P_n$	$B_t$
70	0	1790	0.290	0.988
110	0	3380	0.253	1.357
190	0	4220	0.165	1.523
270	0	4760	0.123	1.623

$\lambda g = 200, t/\lambda = 0.3, X_n = 0.4$				
$N^*I$	$F_t$	$F_n$	$P_n$	$B_t$
70	34	693	0.129	0.441
110	82	1590	0.125	0.670
190	211	2560	0.097	0.898
270	352	2870	0.077	1.019

$\lambda g = 200, t/\lambda = 0.4, X_n = \text{IN}$				
$N^*I$	$F_t$	$F_n$	$P_n$	$B_t$
70	0	2390	0.381	0.974
110	0	4590	0.336	1.352
190	0	5750	0.218	1.515
270	0	6510	0.164	1.614

$\lambda g = 200, t/\lambda = 0.4, X_n = 0.4$				
$N^*I$	$F_t$	$F_n$	$P_n$	$B_t$
70	31	1310	0.222	0.567
110	78	3000	0.214	0.860
190	200	4760	0.161	1.118
270	334	5340	0.124	1.226

$\lambda g = 200, t/\lambda = 0.5, X_n = \text{IN}$				
$N^*I$	$F_t$	$F_n$	$P_n$	$B_t$
70	0	2990	0.472	0.966
110	0	5810	0.419	1.347
190	0	7790	0.272	1.510
270	0	8250	0.204	1.609

$\lambda g = 200, t/\lambda = 0.5, X_n = 0.4$				
$N^*I$	$F_t$	$F_n$	$P_n$	$B_t$
70	32	1920	0.314	0.642
110	78	4370	0.301	0.970
190	194	6790	0.222	1.234
270	319	7660	0.170	1.342

$\lambda g = 200, t/\lambda = 0.3, X_n = 0.2$				
$N^*I$	$F_t$	$F_n$	$P_n$	$B_t$
70	32	1280	0.216	0.737
110	75	2900	0.208	1.113
190	166	4500	0.153	1.412
270	228	4940	0.114	1.503

$\lambda g = 200, t/\lambda = 0.3, X_n = 0.6$				
$N^*I$	$F_t$	$F_n$	$P_n$	$B_t$
70	33	43	0.037	0.127
110	77	98	0.037	0.198
190	184	229	0.036	0.331
270	301	366	0.034	0.453

$\lambda g = 200, t/\lambda = 0.4, X_n = 0.2$				
$N^*I$	$F_t$	$F_n$	$P_n$	$B_t$
70	31	1880	0.307	0.786
110	73	4190	0.292	1.175
190	146	6150	0.207	1.438
270	197	6870	0.155	1.533

$\lambda g = 200, t/\lambda = 0.4, X_n = 0.6$				
$N^*I$	$F_t$	$F_n$	$P_n$	$B_t$
70	32	703	0.133	0.340
110	79	1610	0.128	0.516
190	209	2560	0.100	0.693
270	351	2880	0.080	0.791

$\lambda g = 200, t/\lambda = 0.5, X_n = 0.2$				
$N^*I$	$F_t$	$F_n$	$P_n$	$B_t$
70	32	2480	0.399	0.815
110	72	5460	0.377	1.211
190	135	7720	0.261	1.450
270	184	8690	0.196	1.547

$\lambda g = 200, t/\lambda = 0.5, X_n = 0.6$				
$N^*I$	$F_t$	$F_n$	$P_n$	$B_t$
70	33	1330	0.227	0.464
110	80	3030	0.218	0.702
190	207	4780	0.165	0.914
270	348	5370	0.128	1.011

Table 5.1 Cont'd

$\lambda g = 200, t/\lambda = 0.3, X_n = 0.8$				
$N^*I$	$F_t$	$F_n$	$P_n$	$B_t$
70	2	2	0.021	0.071
110	4	5	0.021	0.112
190	11	15	0.021	0.193
270	22	31	0.021	0.275

$\lambda g = 250, t/\lambda = 0.3, X_n = IN$				
$N^*I$	$F_t$	$F_n$	$P_n$	$B_t$
55	0	1650	0.281	0.941
90	0	3370	0.246	1.345
160	0	4190	0.154	1.503
230	0	4760	0.115	1.607

$\lambda g = 200, t/\lambda = 0.4, X_n = 0.8$				
$N^*I$	$F_t$	$F_n$	$P_n$	$B_t$
70	30	44	0.041	0.104
110	70	101	0.040	0.162
190	177	236	0.039	0.271
270	296	378	0.038	0.373

$\lambda g = 250, t/\lambda = 0.4, X_n = IN$				
$N^*I$	$F_t$	$F_n$	$P_n$	$B_t$
55	0	2200	0.370	0.930
90	0	4570	0.326	1.339
160	0	5690	0.205	1.497
230	0	6480	0.152	1.600

$\lambda g = 200, t/\lambda = 0.5, X_n = 0.8$				
$N^*I$	$F_t$	$F_n$	$P_n$	$B_t$
70	34	710	0.139	0.284
110	81	1620	0.134	0.431
190	209	2570	0.105	0.585
270	346	2900	0.086	0.676

$\lambda g = 250, t/\lambda = 0.5, X_n = IN$				
$N^*I$	$F_t$	$F_n$	$P_n$	$B_t$
55	0	2760	0.459	0.923
90	0	5770	0.406	1.335
160	0	7200	0.255	1.493
230	0	8200	0.190	1.595

$\lambda g = 200, t/\lambda = 0.3, X_n = OUT$				
$N^*I$	$F_t$	$F_n$	$P_n$	$B_t$
70	0	2	0.019	0.065
110	0	5	0.019	0.104
190	0	14	0.019	0.179
270	0	31	0.019	0.254

$\lambda g = 250, t/\lambda = 0.3, X_n = 0.2$				
$N^*I$	$F_t$	$F_n$	$P_n$	$B_t$
55	18	1190	0.208	0.698
90	51	2920	0.200	1.093
160	131	4500	0.142	1.384
230	191	4960	0.106	1.478

$\lambda g = 200, t/\lambda = 0.4, X_n = OUT$				
$N^*I$	$F_t$	$F_n$	$P_n$	$B_t$
70	0	3.4	0.026	0.067
110	0	8	0.026	0.106
190	0	24	0.026	0.183
270	0	50	0.026	0.260

$\lambda g = 250, t/\lambda = 0.4, X_n = 0.2$				
$N^*I$	$F_t$	$F_n$	$P_n$	$B_t$
55	17	1740	0.297	0.747
90	48	4180	0.283	1.158
160	114	6190	0.195	1.424
230	158	6850	0.144	1.510

$\lambda g = 200, t/\lambda = 0.5, X_n = OUT$				
$N^*I$	$F_t$	$F_n$	$P_n$	$B_t$
70	0	84	0.062	0.127
110	0	197	0.061	0.197
190	0	457	0.059	0.326
270	0	825	0.056	0.443

$\lambda g = 250, t/\lambda = 0.5, X_n = 0.2$				
$N^*I$	$F_t$	$F_n$	$P_n$	$B_t$
55	21	2300	0.387	0.777
90	54	5430	0.364	1.196
160	112	7730	0.246	1.436
230	153	8620	0.181	1.524

Table 5.1 Cont'd

$\lambda g = 250, t/\lambda = 0.3, X_n = 0.4$				
$N^*I$	$F_t$	$F_n$	$P_n$	$B_t$
55	22	649	0.123	0.410
90	61	1600	0.118	0.647
160	173	2550	0.089	0.864
230	297	2840	0.070	0.974

$\lambda g = 250, t/\lambda = 0.3, X_n = 0.8$				
$N^*I$	$F_t$	$F_n$	$P_n$	$B_t$
55	0.8	1.3	0.017	0.056
90	2.2	3.5	0.017	0.092
160	7	11	0.017	0.163
230	15	23	0.017	0.235

$\lambda g = 250, t/\lambda = 0.4, X_n = 0.4$				
$N^*I$	$F_t$	$F_n$	$P_n$	$B_t$
55	23	1230	0.214	0.537
90	61	3010	0.205	0.842
160	168	4740	0.149	1.089
230	285	5310	0.114	1.193

$\lambda g = 250, t/\lambda = 0.4, X_n = 0.8$				
$N^*I$	$F_t$	$F_n$	$P_n$	$B_t$
55	22	34	0.034	0.085
90	57	85	0.033	0.137
160	151	203	0.032	0.236
230	257	326	0.031	0.327

$\lambda g = 250, t/\lambda = 0.5, X_n = 0.4$				
$N^*I$	$F_t$	$F_n$	$P_n$	$B_t$
55	22	1790	0.304	0.611
90	59	4370	0.291	0.956
160	160	6740	0.207	1.210
230	271	7610	0.156	1.315

$\lambda g = 250, t/\lambda = 0.5, X_n = 0.8$				
$N^*I$	$F_t$	$F_n$	$P_n$	$B_t$
55	23	667	0.131	0.262
90	62	1630	0.126	0.413
160	173	2570	0.095	0.557
230	294	2860	0.076	0.639

$\lambda g = 250, t/\lambda = 0.3, X_n = 0.6$				
$N^*I$	$F_t$	$F_n$	$P_n$	$B_t$
55	22	33	0.031	0.104
90	57	83	0.031	0.168
160	150	200	0.030	0.288
230	253	320	0.028	0.399

$\lambda g = 250, t/\lambda = 0.3, X_n = \text{OUT}$				
$N^*I$	$F_t$	$F_n$	$P_n$	$B_t$
55	0	1.0	0.015	0.052
90	0	3.1	0.015	0.085
160	0	10	0.015	0.151
230	0	22	0.015	0.217

$\lambda g = 250, t/\lambda = 0.4, X_n = 0.6$				
$N^*I$	$F_t$	$F_n$	$P_n$	$B_t$
55	25	661	0.126	0.316
90	66	1620	0.121	0.497
160	179	2560	0.091	0.644
230	304	2850	0.072	0.753

$\lambda g = 250, t/\lambda = 0.4, X_n = \text{OUT}$				
$N^*I$	$F_t$	$F_n$	$P_n$	$B_t$
55	0	1.9	0.021	0.053
90	0	5.2	0.021	0.087
160	0	17	0.021	0.155
230	0	36	0.021	0.222

$\lambda g = 250, t/\lambda = 0.5, X_n = 0.6$				
$N^*I$	$F_t$	$F_n$	$P_n$	$B_t$
55	23	1250	0.218	0.439
90	63	3040	0.209	0.687
160	172	4760	0.152	0.889
230	295	5330	0.117	0.980

$\lambda g = 250, t/\lambda = 0.5, X_n = \text{OUT}$				
$N^*I$	$F_t$	$F_n$	$P_n$	$B_t$
55	0	65	0.052	0.104
90	0	163	0.051	0.168
160	0	392	0.049	0.286
230	0	628	0.047	0.392

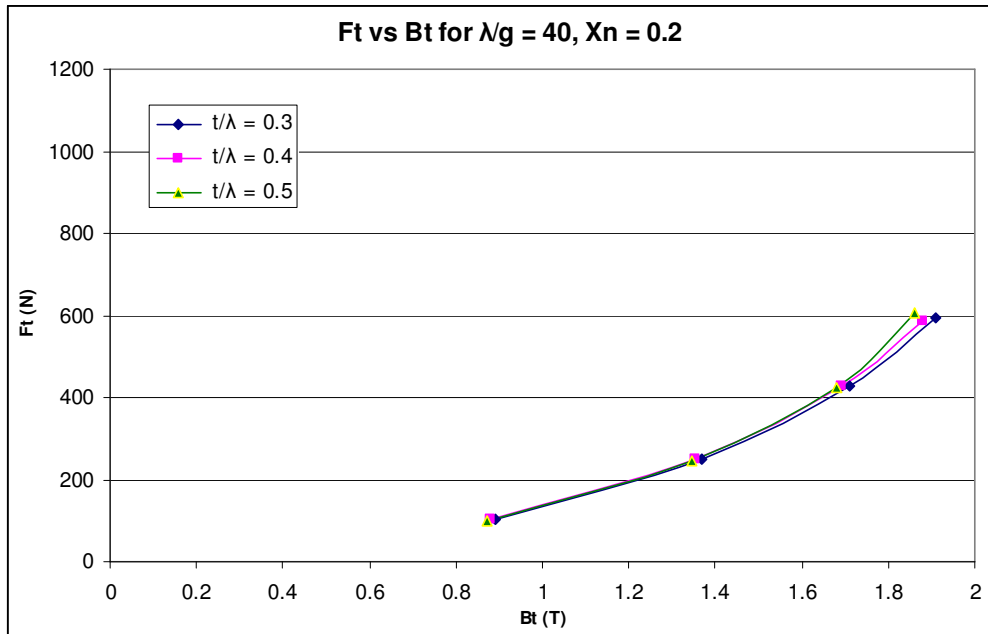


Figure 5. 1 Tangential force vs tooth flux density for  $\lambda/g = 40, X_n = 0.2$

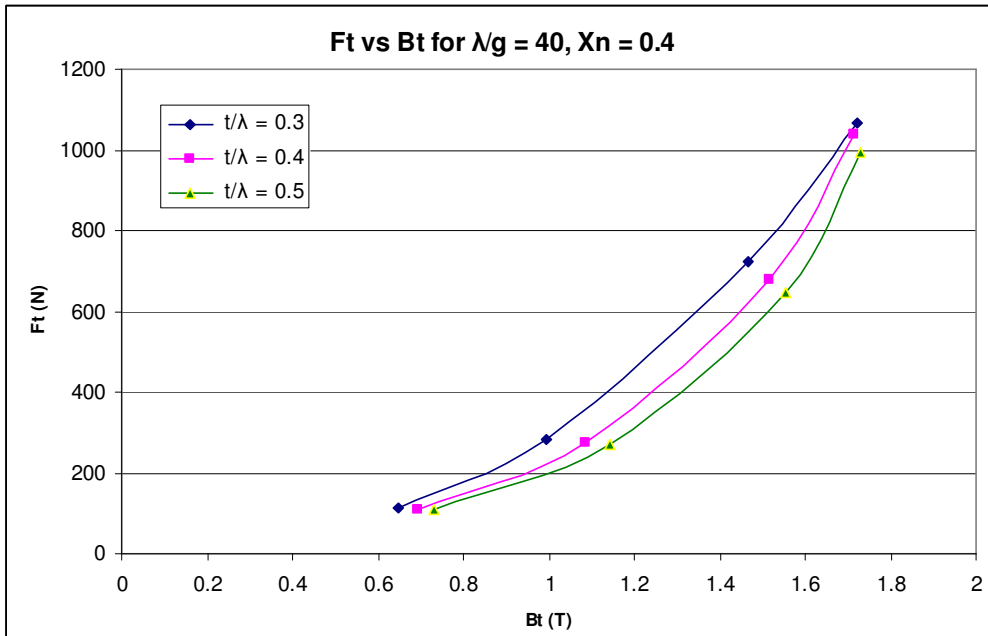


Figure 5. 2 Tangential force vs tooth flux density for  $\lambda/g = 40, X_n = 0.4$

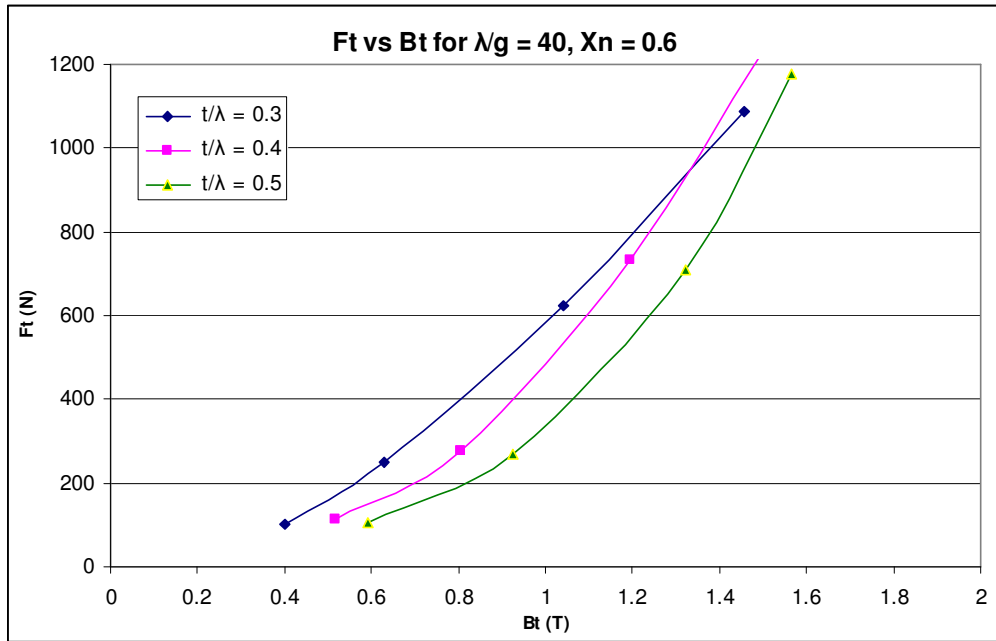


Figure 5. 3 Tangential force vs tooth flux density for  $\lambda/g = 40, X_n = 0.6$

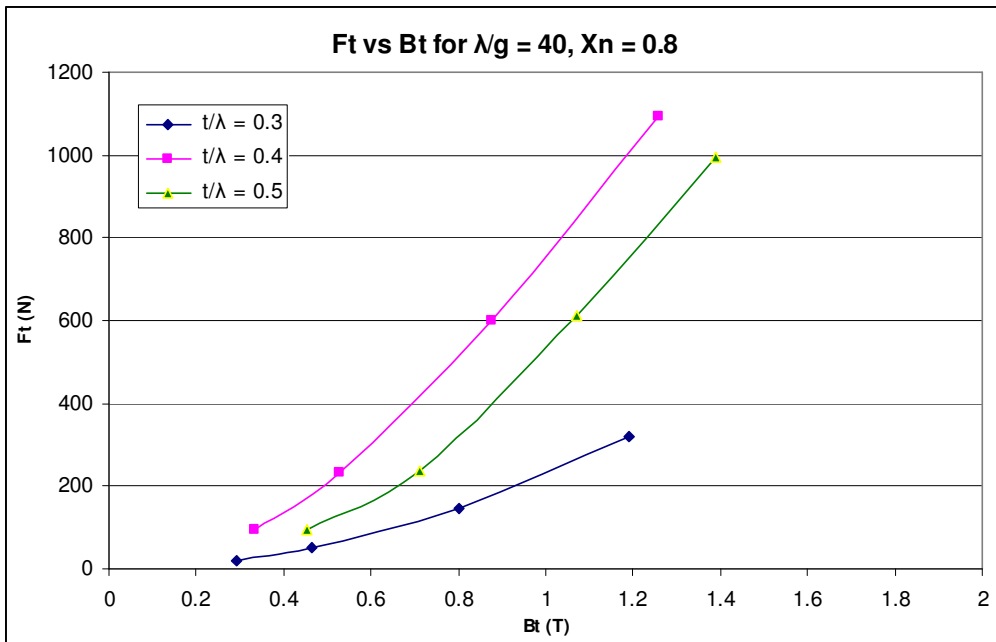


Figure 5. 4 Tangential force vs tooth flux density for  $\lambda/g = 40, X_n = 0.8$

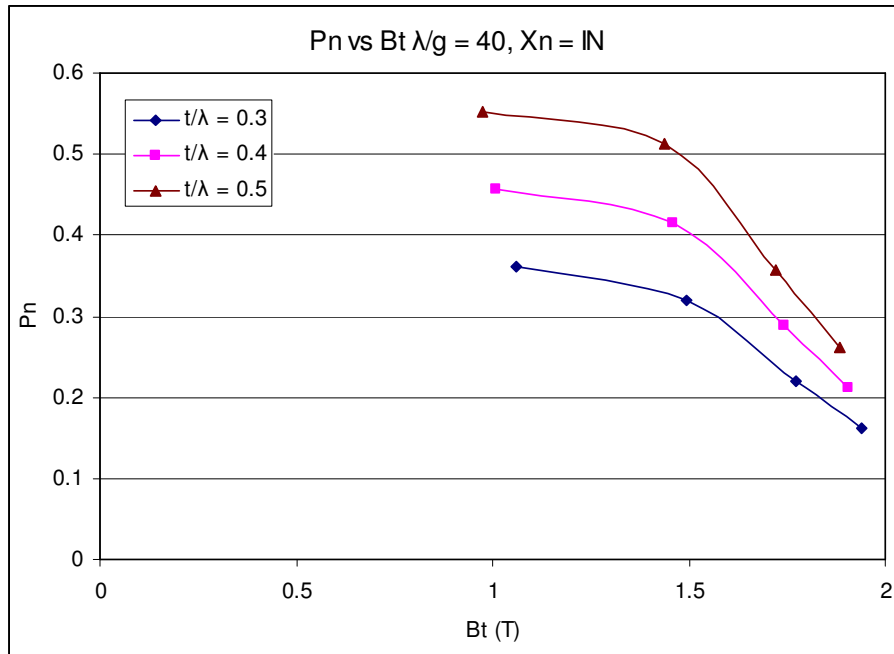


Figure 5. 5 Normalized Permeance vs tooth flux density for  $\lambda/g = 40$ ,  $X_n = 0.0$

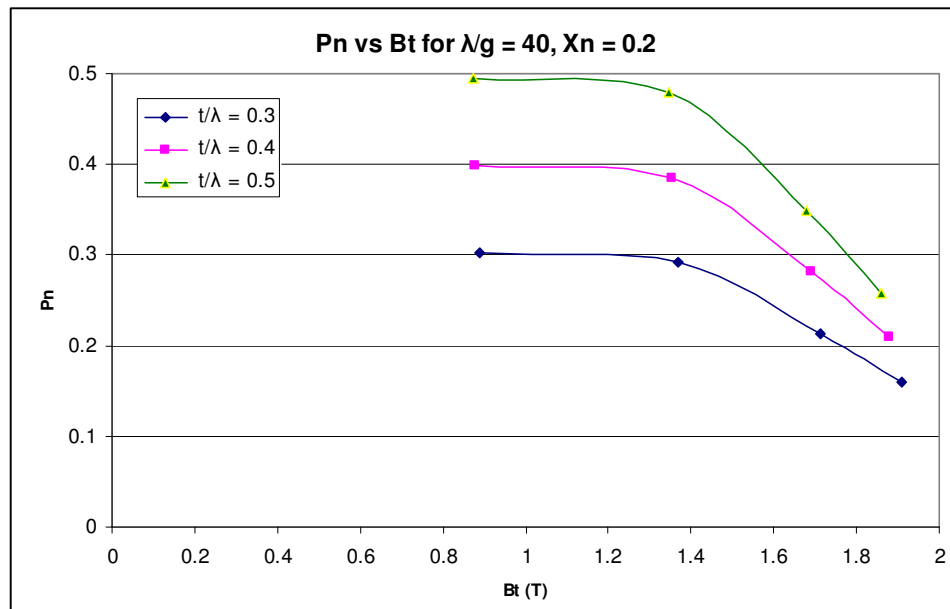


Figure 5. 6 Normalized Permeance vs tooth flux density for  $\lambda/g = 40$ ,  $X_n = 0.2$

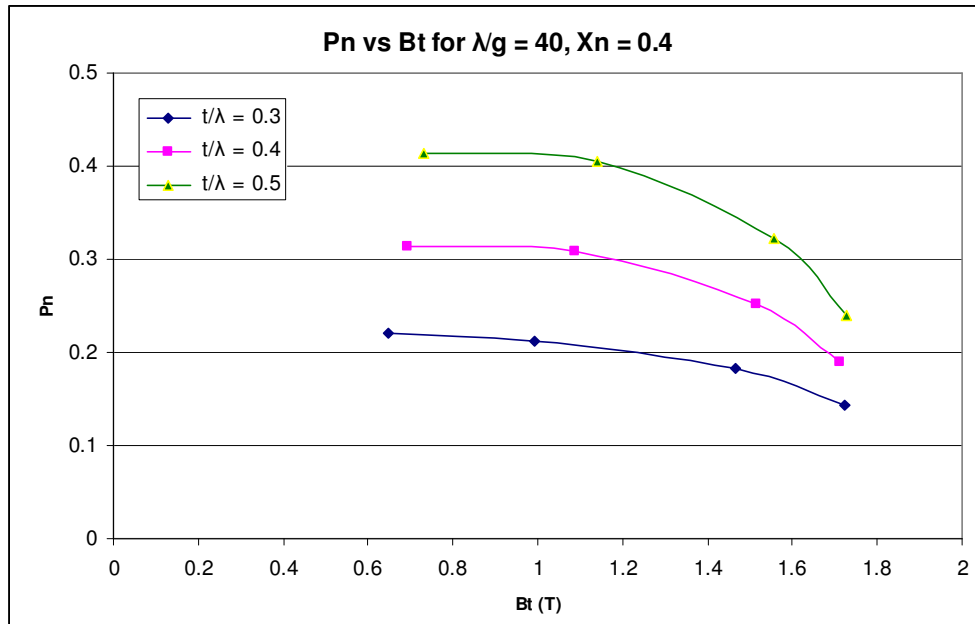


Figure 5. 7 Normalized Permeance vs tooth flux density for  $\lambda/g = 40, X_n = 0.4$

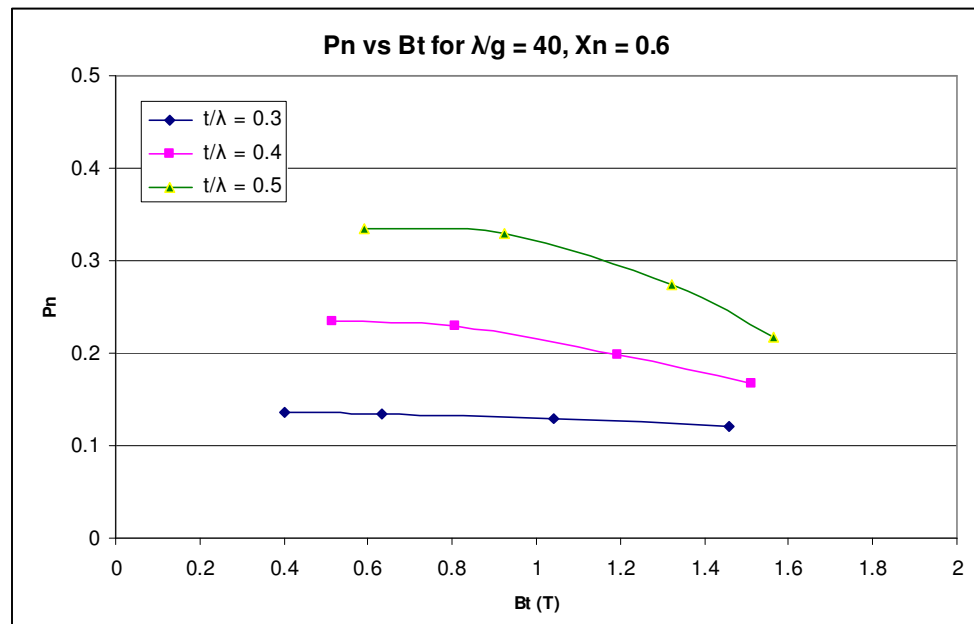


Figure 5. 8 Normalized Permeance vs tooth flux density for  $\lambda/g = 40, X_n = 0.6$



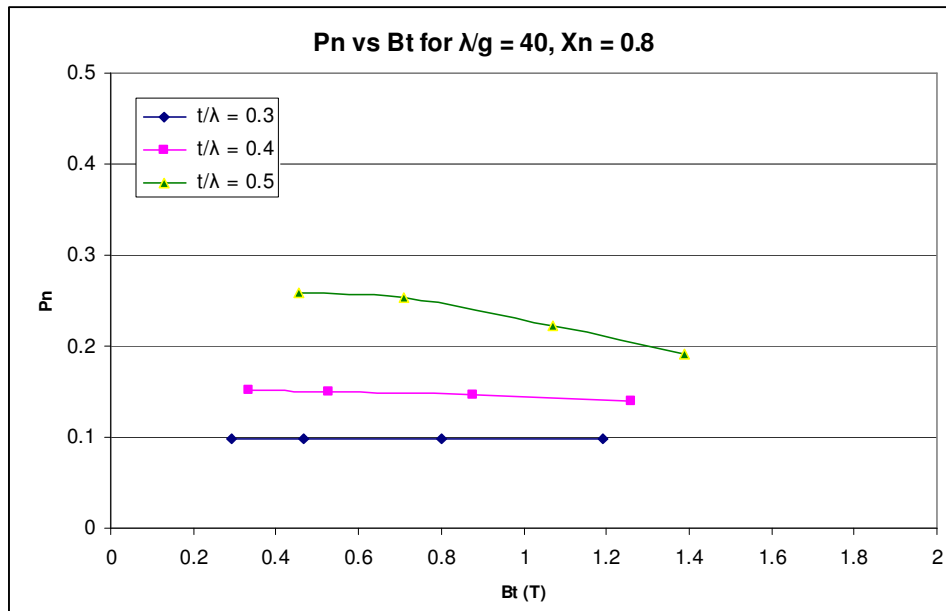


Figure 5. 9 Normalized Permeance vs tooth flux density for  $\lambda/g = 40, X_n = 0.8$

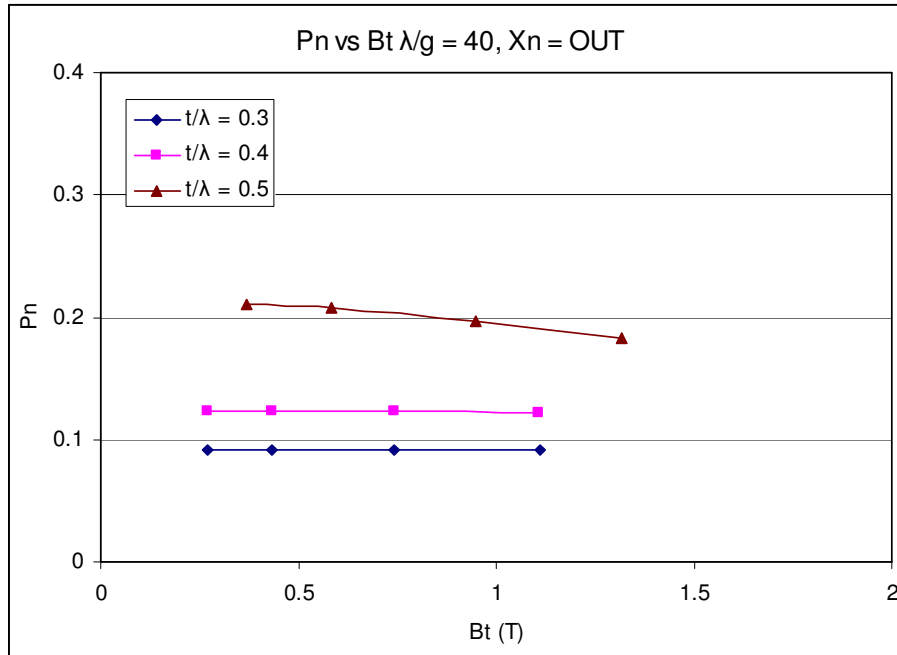


Figure 5. 10 Normalized Permeance vs tooth flux density for  $\lambda/g = 40, X_n = 1.0$

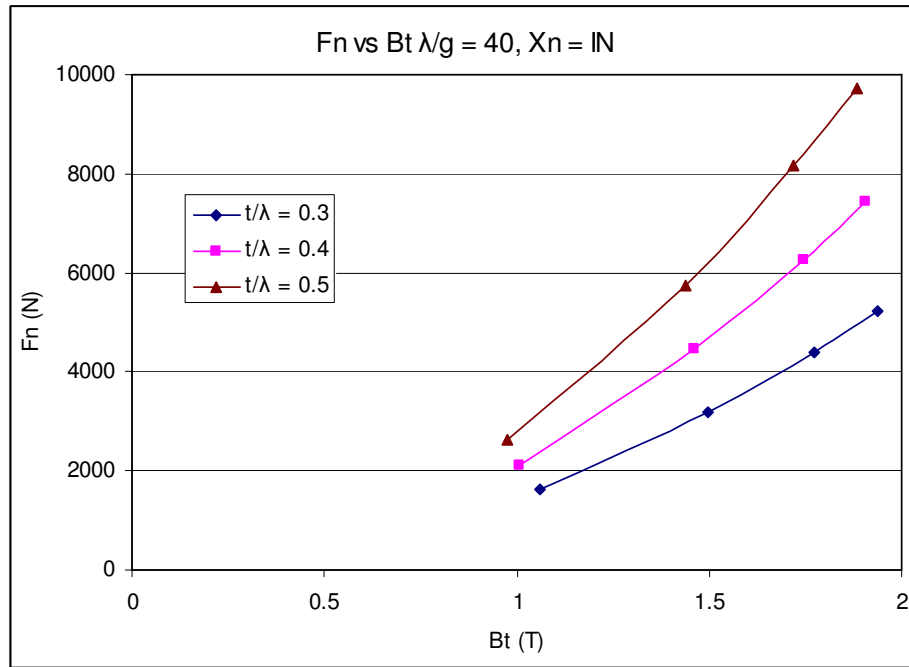


Figure 5. 11 Normal Force vs tooth flux density for  $\lambda/g = 40, X_n = 0.0$

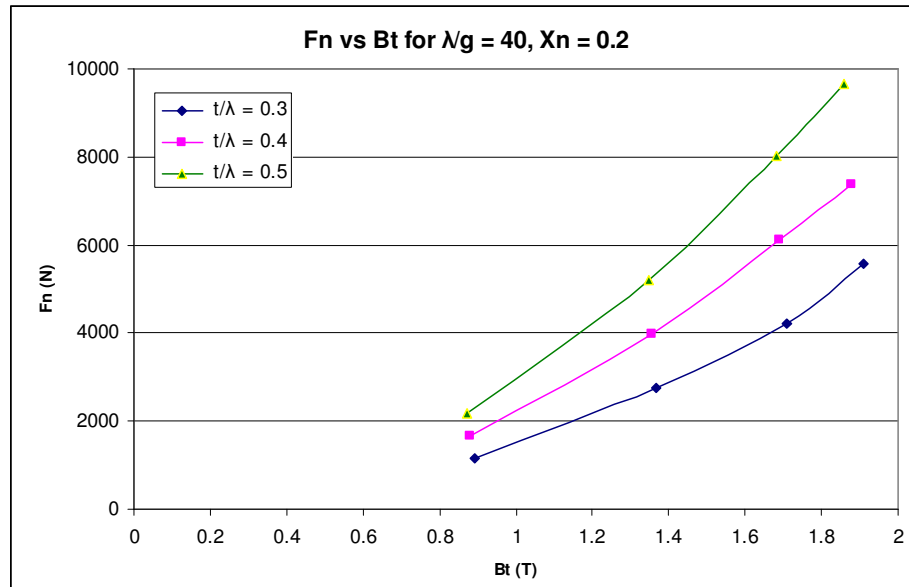


Figure 5. 12 Normal Force vs tooth flux density for  $\lambda/g = 40, X_n = 0.2$

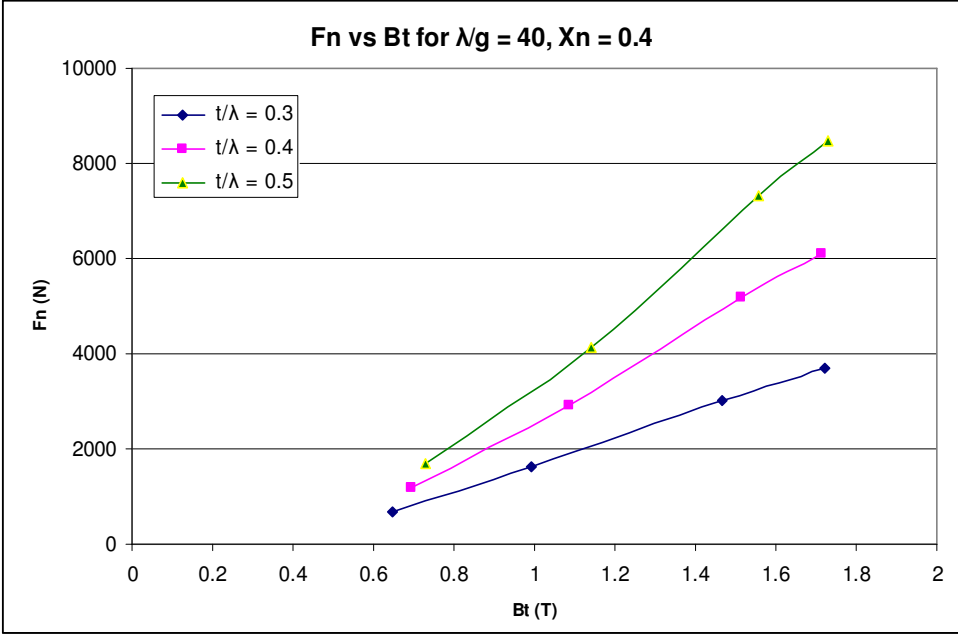


Figure 5. 13 Normal Force vs tooth flux density for  $\lambda/g = 40, X_n = 0.4$

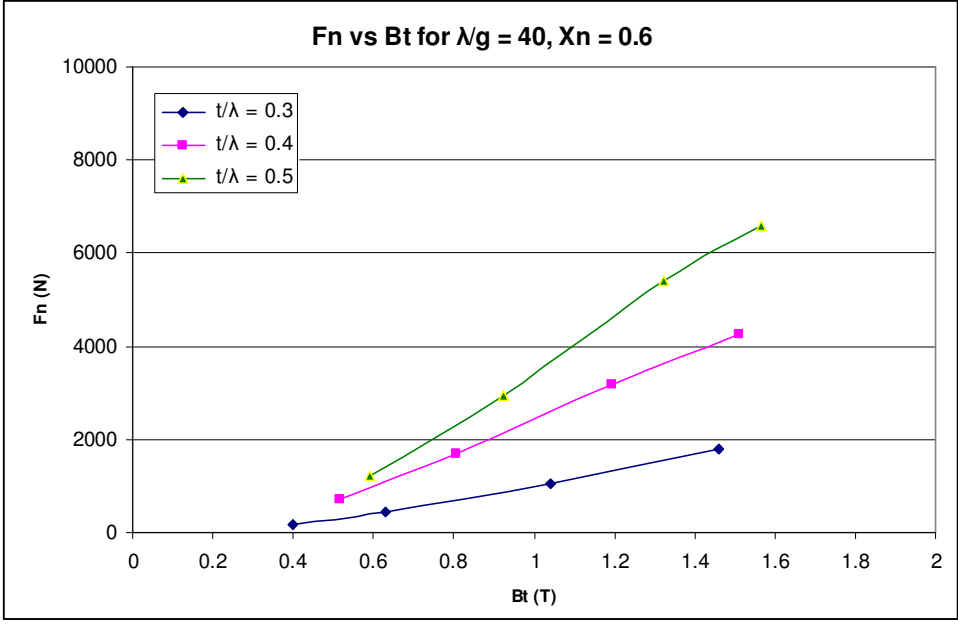


Figure 5. 14 Normal Force vs tooth flux density for  $\lambda/g = 40, X_n = 0.6$

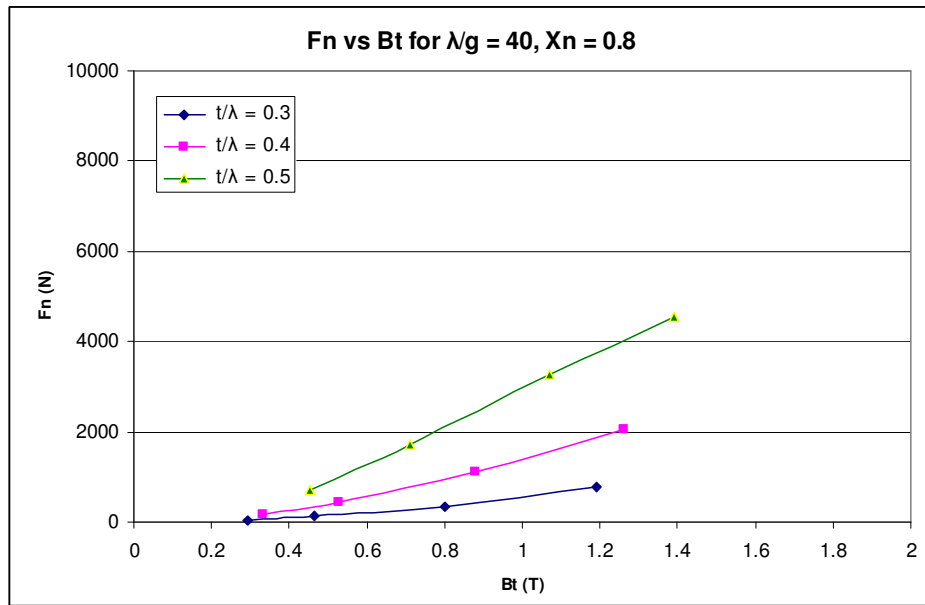


Figure 5. 15 Normal Force vs tooth flux density for  $\lambda/g = 40, X_n = 0.8$

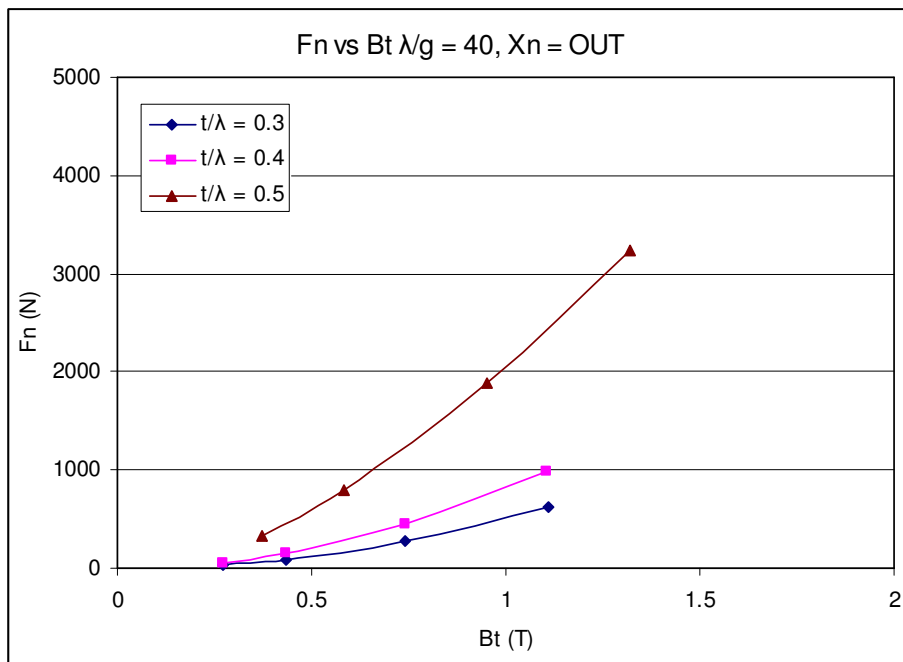


Figure 5. 16 Normal Force vs tooth flux density for  $\lambda/g = 40, X_n = 1.0$

### 5.3 Predictions Using Reference [21] for Test Motors

The obtained data is tested by applying the approach presented in [21]. This approach is based on the assumption that the tangential force contributions of individual pairs of teeth can be added to compute the torque produced by the motor. On the other hand, for the aim of determining the operating point, a particular position of rotor teeth is chosen and then the MMF drop on the back iron and teeth region is calculated. Bisection method is applied in order to calculate the operating point between teeth region and back iron (Figure 5.17). This calculation will lead to find the flux passing through the poles. After then, end-leakage correction is applied to generate the flux-linkage vs. current vs. position curve of the specified motor.

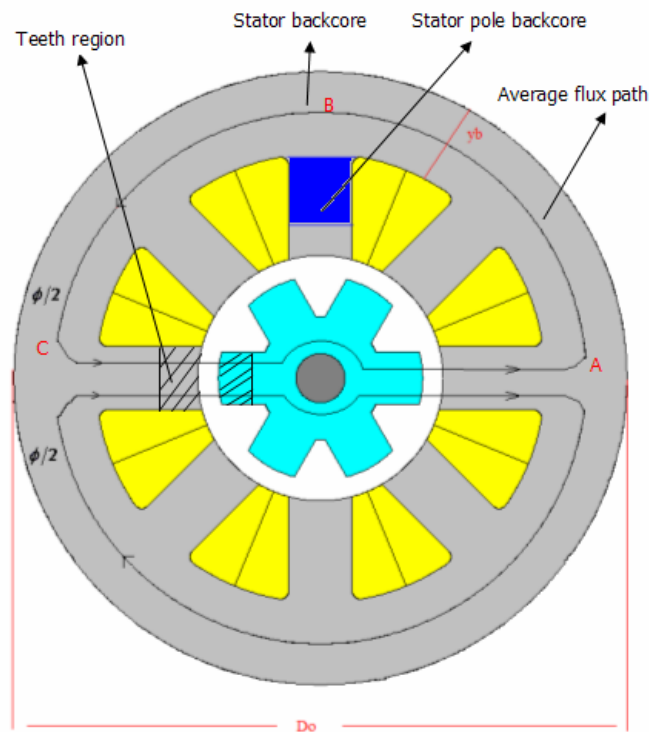


Figure 5. 17 Cross Section of a 8/6 Switched Reluctance Motor

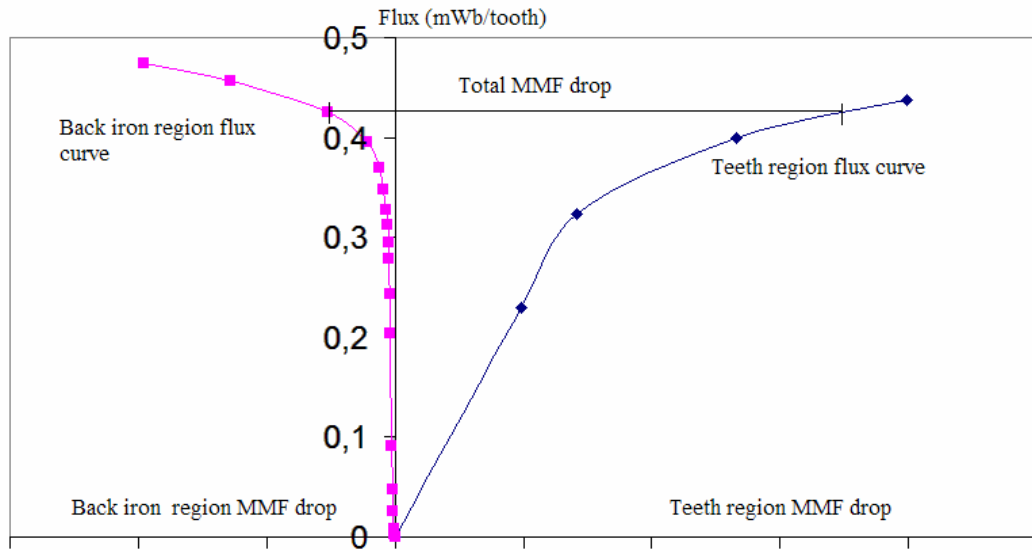


Figure 5. 18 Operating point determination

The software package developed in that approach is used to predict both static torque-position curves and flux linkage-position curves for SR1 and SR2. The software is used after entering the normalized data introduced in table-5.1. Figures from 5.19 to 5.22 show the predictions of flux linkage (with end-leakage correction) and static torque for SR2 and SR1 respectively. The percentage error between predicted and measured values is included in tables 5.2 to 5.5 and is calculated by using equation 5.1.

$$ERR\% = \frac{Measured - Predicted}{Measured} * 100\% \quad (5.1)$$

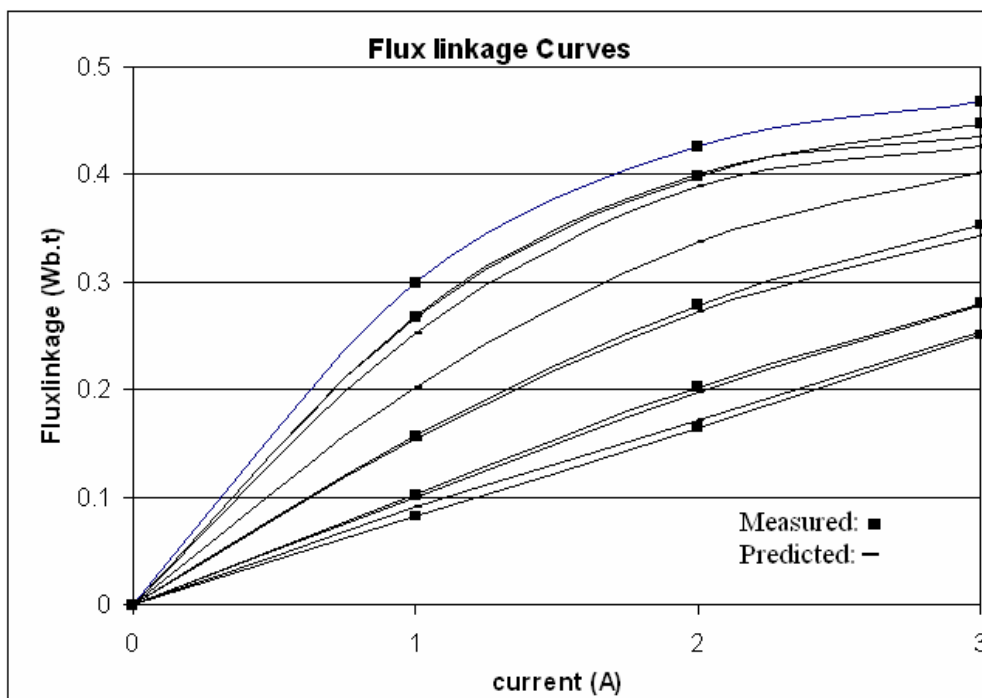


Figure 5. 19 Flux linkage predictions with endleakage correction for SR2

Table 5. 2 Measured and predicted flux linkage for SR2 with end-leakage correction (in Wb.t)

Xn = 0.0				Xn = 0.2			
I	Measured	Predicted	%ERR	I	Measured	Predicted	%ERR
1	0.299	0.268	10.4	1	0.267	0.252	5.6
2	0.425	0.400	5.9	2	0.398	0.388	2.5
3	0.468	0.435	7.1	3	0.446	0.425	4.7
Xn = 0.4				Xn = 0.6			
I	Measured	Predicted	%ERR	I	Measured	Predicted	%ERR
1	0.208	0.203	2.4	1	0.157	0.154	1.9
2	0.348	0.337	3.2	2	0.279	0.272	2.5
3	0.417	0.402	3.6	3	0.353	0.343	2.8
Xn = 0.8				Xn = 1.0			
I	Measured	Predicted	%ERR	I	Measured	Predicted	%ERR
1	0.102	0.100	2.0	1	0.083	0.090	-8.4
2	0.202	0.198	2.0	2	0.165	0.172	-4.2
3	0.28	0.278	0.7	3	0.251	0.254	-1.2

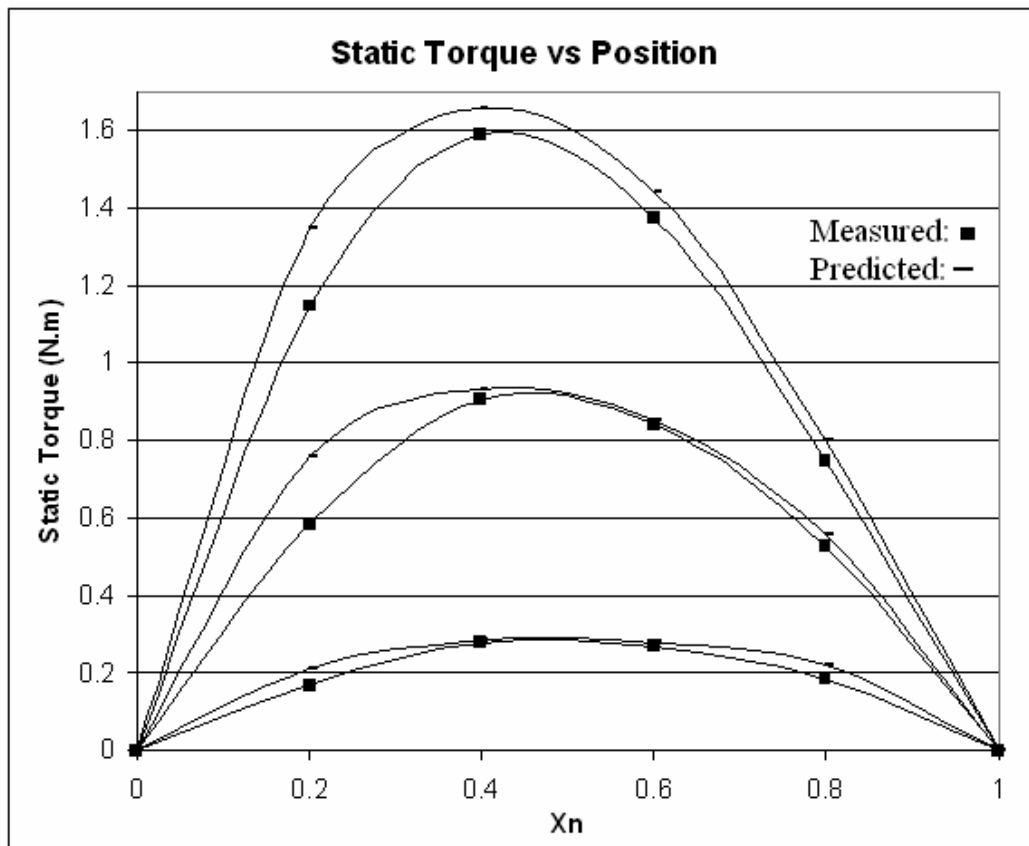


Figure 5. 20 Predictions of static torque characteristic for SR2

Table 5. 3 Measured and predicted static torque of SR2 (in N.m)

$X_n$	Measured 1A	Predicted 1A	%ERR 1A	Measured 2A	Predicted 2A	%ERR 2A	Measured 3A	Predicted 3A	%ERR 3A
0	0.0	0.0	0.0	0.0	0.0	0.0	0.0	0.0	0.0
0.2	0.185	0.210	-25.7	0.525	0.760	-30.6	0.748	1.35	-17.4
0.4	0.27	0.285	-2.5	0.842	0.933	-3.1	1.375	1.66	-4.5
0.6	0.278	0.278	-2.9	0.905	0.851	-1.1	1.588	1.44	-4.7
0.8	0.167	0.22	-18.9	0.582	0.559	-6.5	1.15	0.8	-6.9
1	0.0	0.0	0.0	0.0	0.0	0.0	0.0	0.0	0.0



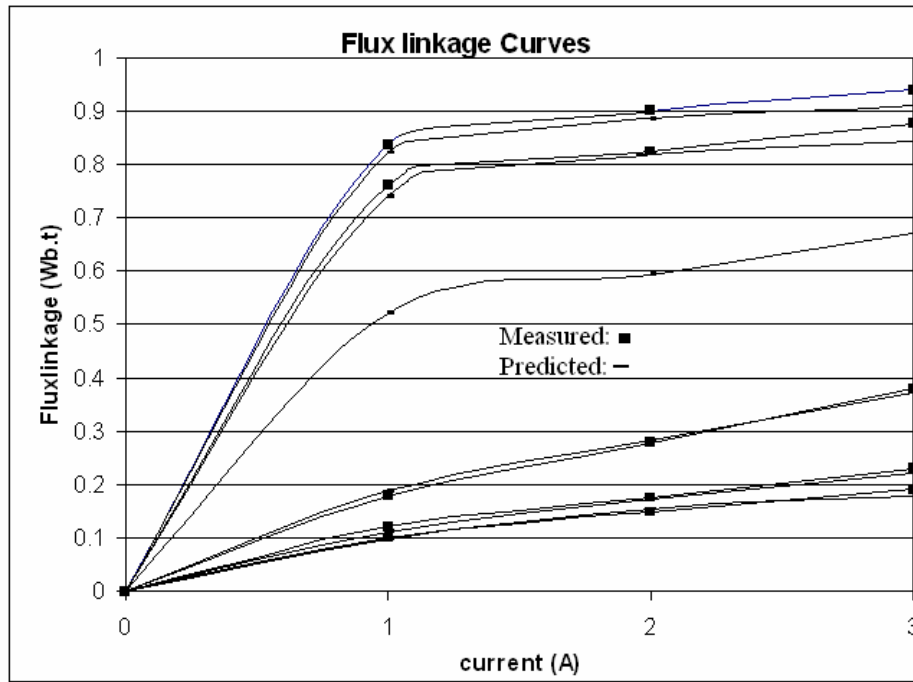


Figure 5. 21 Flux linkage predictions with endleakage correction for SR1

Table 5. 4 Measured and predicted flux linkage for SR1 with end-leakage correction (in Wb.t)

Xn = 0.0				Xn = 0.2			
I	Measured	Predicted	%ERR	I	Measured	Predicted	%ERR
2	0.835	0.82	1.8	2	0.76	0.74	2.6
3	0.9	0.884	1.8	3	0.825	0.817	1.0
4	0.938	0.91	3.0	4	0.875	0.841	3.9
Xn = 0.4				Xn = 0.6			
I	Measured	Predicted	%ERR	I	Measured	Predicted	%ERR
2	0.515	0.52	-1.0	2	0.18	0.188	-4.4
3	0.61	0.593	2.8	3	0.28	0.282	-0.7
4	0.675	0.671	0.6	4	0.38	0.372	2.1
Xn = 0.8				Xn = 1.0			
I	Measured	Predicted	%ERR	I	Measured	Predicted	%ERR
2	0.12	0.111	7.5	2	0.1	0.098	2.0
3	0.175	0.172	1.7	3	0.15	0.154	-2.7
4	0.23	0.222	3.5	4	0.19	0.178	6.3

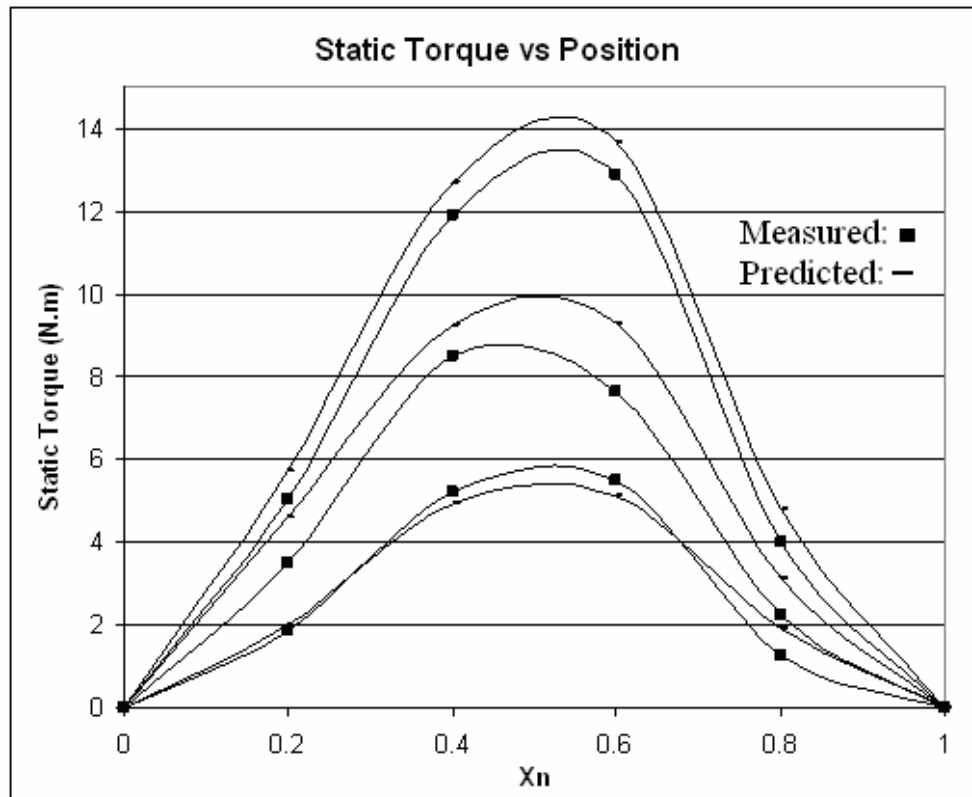


Figure 5. 22 Predictions of static torque characteristic for SR1

Table 5. 5 Measured and predicted static torque of SR1 (in N.m)

$X_n$	Measured 2A	Predicted 2A	%ERR 2A	Measured 3A	Predicted 3A	%ERR 3A	Measured 4A	Predicted 4A	%ERR 4A
0	0.0	0.0	0.0	0.0	0.0	0.0	0.0	0.0	0.0
0.2	1.870	2.02	-8.0	3.500	4.6	-31.4	5.00	5.70	-14
0.4	5.200	4.9	5.8	8.500	9.25	-8.8	11.87	12.70	-7.0
0.6	5.500	5.1	7.2	7.625	9.3	-21.9	12.87	13.65	-6.0
0.8	1.250	1.9	-52	2.250	3.1	-37.8	4.00	4.80	-22
1	0.0	0.0	0.0	0.0	0.0	0.0	0.0	0.0	0.0

It is obvious that the percentage error in the flux linkage, as well as static torque, predictions for both SR1 and SR2 match the results of finite element solutions presented in chapter four. In other words, results of finite element solutions match the predictions obtained by reference [21] where the set of normalized data is used.

In table-5.6, at several speed values for SR2, the predicted torques, measured ones and the percentage error are presented for four different advance angles. The percentage error is calculated by equation 5.1. The results obtained are also presented in figures 5.23 to 5.26.

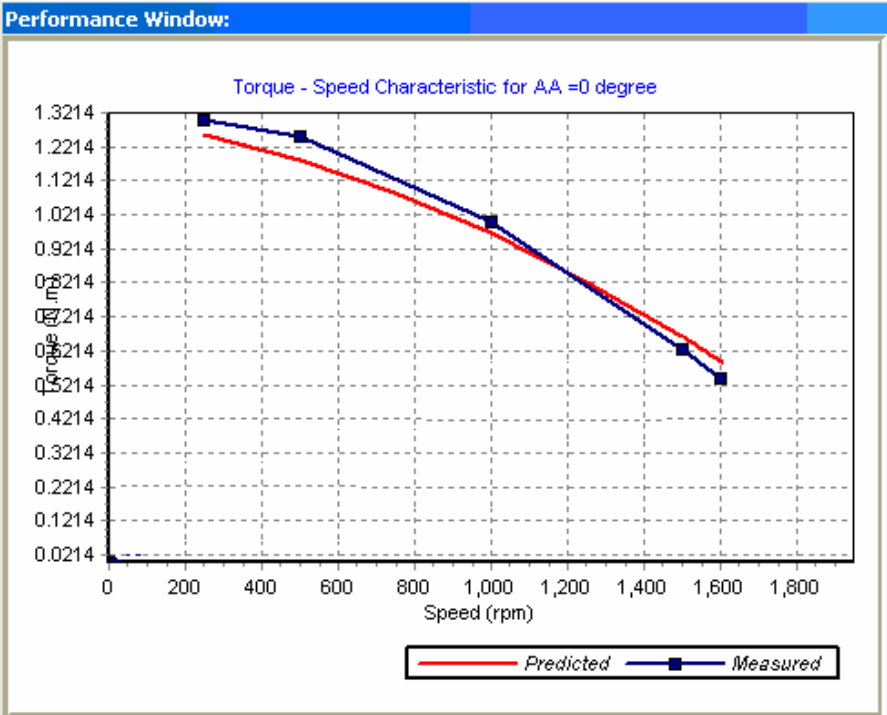


Figure 5. 23 Torque-speed characteristic at 0° advanced angle

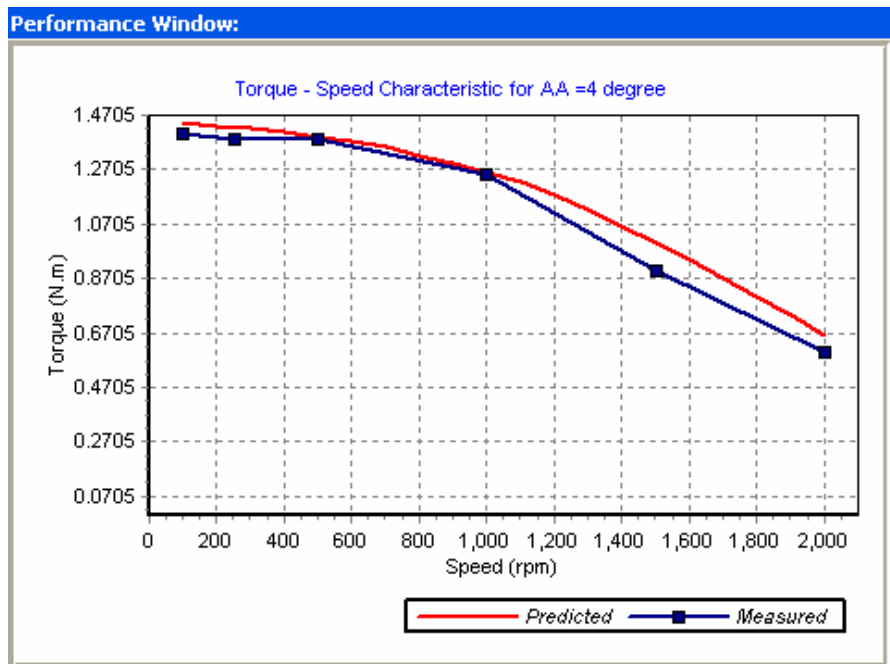


Figure 5. 24 Torque-speed characteristic at 4° advanced angle

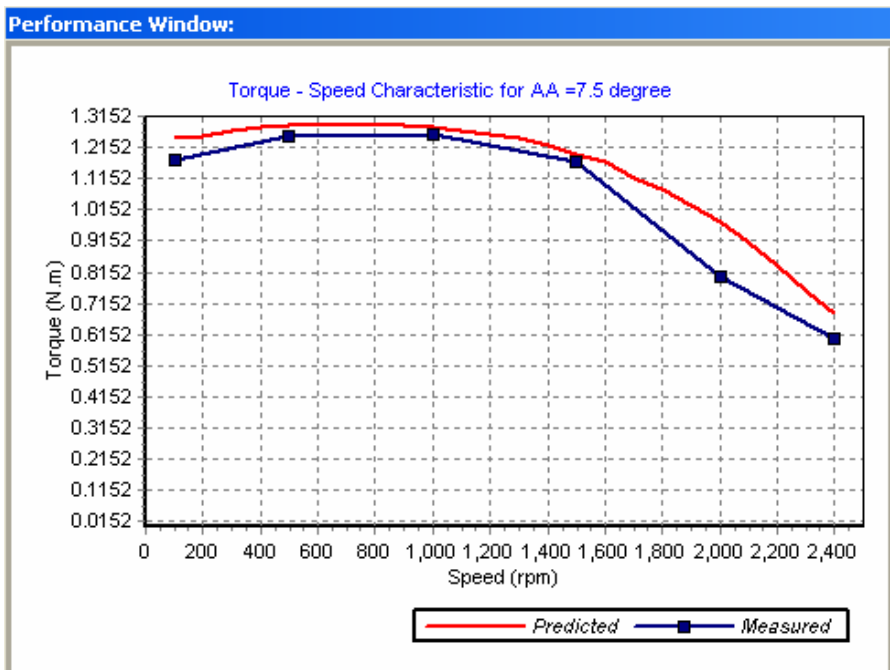


Figure 5. 25 Torque-speed characteristic at 7.5° advanced angle

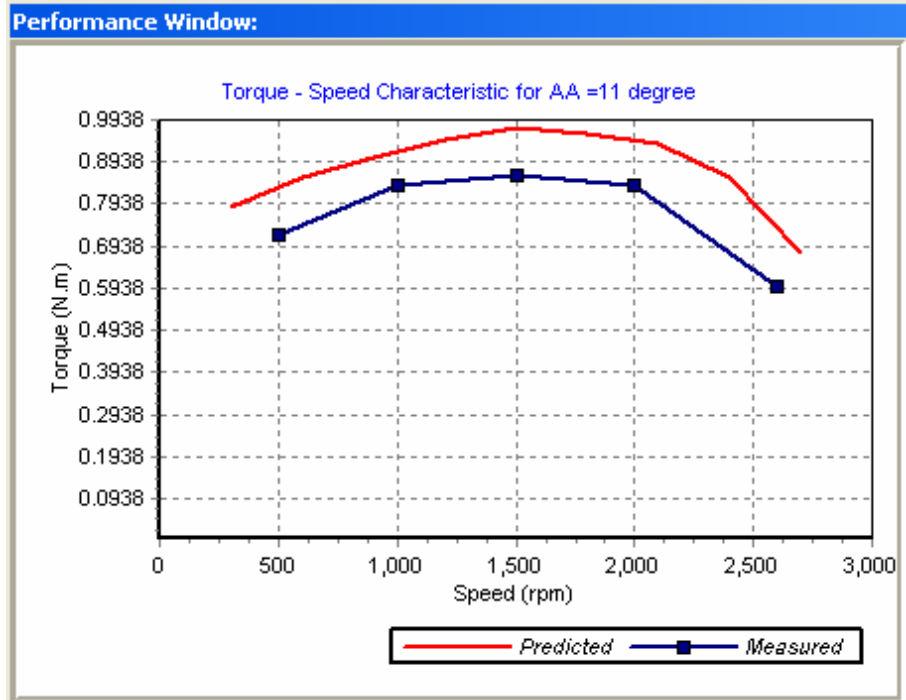


Figure 5. 26 Torque-speed characteristic at 11° advanced angle

Table 5. 6 Predicted-Measured Torques (N.m) and Percentage Errors with End-Leakage Correction for SR2

AA = 0°				AA = 4°			
Rpm	Measured	Predicted	%ERR	rpm	Measured	Predicted	%ERR
250	1.300	1.250	3.8	250	1.380	1.410	-2.2
500	1.250	1.182	5.4	500	1.380	1.387	-0.5
1000	1.000	0.971	2.9	1000	1.250	1.256	-0.48
1500	0.625	0.668	-6.9	1500	0.900	0.990	-10.0
1600	0.540	0.581	-7.6	2000	0.600	0.670	-11.7
AA = 7.5°				AA = 11°			
Rpm	Measured	Predicted	%ERR	rpm	Measured	Predicted	%ERR
500	1.250	1.283	-2.6	500	0.720	0.830	-15.2
1000	1.255	1.273	-1.4	1000	0.840	0.915	-8.9
1500	1.170	1.191	-1.8	1500	0.860	0.967	-12.4
2000	0.800	0.963	-20.0	2000	0.840	0.945	-12.5
2400	0.600	0.685	-14.2	2600	0.600	0.645	-7.5

#### 5.4 Comparison of Numerical Results and Analytical Predictions

Since the normalized data is obtained by finite element method and applied to the software developed by reference [21] to predict the characteristics of the test motors, it is important to compare the results obtained from numerical solutions for the test motors and the analytically predicted results based on the normalized data. Such a comparison will give an idea about how much the results of finite element solutions are reliable. The following tables, 5.7 and 5.8, show the percentage error between the flux linkage numerical results and the analytically predicted ones for both SR1 and SR2. The percentage error is calculated using equation 5.2.

$$\%ERR = \frac{\text{Numerical} - \text{Predicted}}{\text{Numerical}} * 100\% \quad (5.1)$$

Table 5. 7 Comparison of Flux linkage for SR2 with end-leakage correction (in Wb.t)

Xn = 0.0				Xn = 0.2			
I	Numerical	Analytical	%ERR	I	Numerical	Analytical	%ERR
1	0.269	0.268	0.37	1	0.252	0.252	0.0
2	0.398	0.400	-0.50	2	0.388	0.388	0.0
3	0.440	0.435	1.13	3	0.426	0.425	0.23
Xn = 0.4				Xn = 0.6			
I	Numerical	Analytical	%ERR	I	Numerical	Analytical	%ERR
1	0.202	0.203	-0.50	1	0.155	0.154	0.65
2	0.338	0.337	0.30	2	0.267	0.272	-1.87
3	0.392	0.402	-2.55	3	0.344	0.343	0.29
Xn = 0.8				Xn = 1.0			
I	Numerical	Analytical	%ERR	I	Numerical	Analytical	%ERR
1	0.100	0.100	0.0	1	0.089	0.090	-1.12
2	0.198	0.198	0.0	2	0.173	0.172	0.58
3	0.279	0.278	0.36	3	0.255	0.254	0.39

Table 5. 8 Comparison of Flux linkage for SR1 with end-leakage correction (in Wb.t)

Xn = 0.0				Xn = 0.2			
I	Numerical	Analytical	%ERR	I	Numerical	Analytical	%ERR
2	0.822	0.82	0.24	2	0.739	0.74	-0.13
3	0.879	0.884	-0.57	3	0.809	0.817	-1.0
4	0.917	0.91	0.76	4	0.842	0.841	0.12
Xn = 0.4				Xn = 0.6			
I	Numerical	Analytical	%ERR	I	Numerical	Analytical	%ERR
2	0.505	0.52	-2.97	2	0.183	0.188	-2.7
3	0.598	0.593	0.83	3	0.272	0.282	-3.68
4	0.659	0.671	-1.82	4	0.371	0.372	-0.27
Xn = 0.8				Xn = 1.0			
I	Numerical	Analytical	%ERR	I	Numerical	Analytical	%ERR
2	0.116	0.111	4.3	2	0.102	0.098	3.92
3	0.171	0.172	-0.58	3	0.152	0.154	-1.32
4	0.227	0.222	2.2	4	0.181	0.178	1.66

As seen from the tables, the percentage error is acceptable and largest at the smallest exciting current possibly because of rounding the values. Moreover, sometimes the numerical results are higher than the analytically predicted ones and sometimes smaller. This shows that they are varying close to each other, thus, such a comparison ensures that the normalized data is reliable.

## CHAPTER 6

### CONCLUSION

Flux linkage-current-position curves are very important in the design algorithms of switched reluctance motors. However, these curves are normally obtained from measurements for a specific motor and since these curves are highly nonlinear, it is difficult to predict the motor behavior. In this study, a set of normalized data, from which the flux linkage-current-position or torque-current-position can be predicted for a given VR motor, is presented in a normalized form for a range of excitation levels and different geometries by solving a 2D FEM model. The model developed for this purpose is composed of three pairs of teeth and since it is only a section of a VR motor, the solution time is short (about 83 seconds for the longest solution).

For the aim of verifying the developed model and, hence, the normalized data, the author has solved the model for several sets of parameters chosen from reference [20], where the analytically calculated permeance of identically slotted geometries are given for infinitely permeable teeth. As a result, it is found that the percentage error between the analytically calculated permeance and the results of FEM is found to be no more than half a percent. This is an indication that the FEM is a reliable approach to obtain the magnetic field solution and obtain flux distribution and permeance of doubly-salient structures.

Two test switched reluctance motors are also solved by FEM to obtain the static torque and flux linkage curves for the verification of FEM model accuracy. After then, the curves are compared with the corresponding measurements for these motors. It is found that both measurements and results of numerical solutions match each other with an acceptable percentage error.



Following this, normalized permeance, normal and tangential force given in chapter 5 is produced for identically slotted doubly-salient structures. This data covers  $t/\lambda$  and  $\lambda/g$  values and flux density levels that are encountered in practical applications. In section 3.6 the use of FE solution results to calculate tooth flux density or force on a pair of teeth are explained.

As the third step towards verifying finite element solutions, the author used the set of data produced in this work in a software package developed by Goynük [21]. This software package is capable of predicting the torque-position-current, inductance-position-current curves of a given doubly-salient variable reluctance motor. In the prediction of inductance curves the end leakage effect is also taken into consideration. Using this software, static torque-current-position curves, fluxlinkage-current-position curves and torque-speed curves are predicted for two test motors. Then the author compared the results of these predictions with finite element solutions of the actual motors. From the comparison, it is found that the predicted curves from the data give very good results and predictions accuracy is very close to that obtained from FEM solutions.

In conclusion, the data obtained has been well verified. It is shown that this data is reliable and designers may depend on it to design and predict the behavior of a switched reluctance motor. Moreover, it is important to remind that the data of normal force included in this work is new and not available in the literature and may be utilized when studying the phenomenon of the acoustic noise, as done in a recent work by Bizkevelci [12].

However, for future studies it is suggested that this data should be extended to a wider range of excitation levels and different geometries to make it suitable for predicting the behavior of different switched reluctance motors.

## REFERENCES

- [1] Ertan, H.B. et al.(eds.), “Modern Electrical Drives”, Kluwer Academic Publishers, Netherlands, 2000, page-143.
- [2] Levent Burak, “A Software for Analysis and Design Optimization of Switched Reluctance Motor”, M.Sc. Thesis, Middle East Technical University, 2004.
- [3] Corda, J. and Stephenson, J.M., “Analytical Estimation of Minimum and Maximum Inductances of a Doubly-Salient Motor”, Proc. Of the International Conference on Stepping Motors and Systems, University of Leeds, 1979, pp.50-59.
- [4] Miller, T.J.E. and McGilp, M., “Nonlinear Theory of the Switched Reluctance Motor for Rapid Computer Aided Design”, IEE Proc. 137, Pt B, 6, 1990, pp.337-347.
- [5] Hammond, P., “Energy Methods in Electromagnetism”, Oxford University Press, 1981.
- [6] Dawson, G.E, Easthain, A.R and Mizia, J., “Switched-Reluctance Motor Torque Characteristics: Finite Element Analysis and Test Results”, IEEE I A-23, 1987, pp.532-537.
- [7] Fauchez, B.M, “Magnetic Analysis of a Switched Reluctance Motor using a Boundary Finite Element Coupling Method”, IEEE Trans. On Magnetics, 24, 1, 1988, pp.475-478.
- [8] Moghbelli, N.H., Adams, G.E. and Hoft, R.G., “Prediction of the Instantaneous and Steady State Torque of the Switched Reluctance Motor using the Finite Element Method”, Proc. IEEE IA annual Meeting, 1988, pp.59-70.
- [9] Ertan, H.B., “Analytical Prediction of Torque and Inductance Characteristics of Identically Slotted Doubly Salient Reluctance Motors”, Proc. IEE 133, 4, 1986, pp.230-236.
- [10] D. E. Cameron, J. H. Lang, S. D. Umans, “The origin of acoustic noise in doubly salient variable-reluctance motors”, IEEE Trans. Ind. Application, vol.28, no.6, Nov/Dec 1992, pp.1250-1255.
- [11] Ertan, H.B., “Prediction of Static Torque of Step Motor”, PhD Thesis, University of Leeds, department of Electrical and Electronic Engineering, 1977.

- [12] Erdal Bizkevelci, "A Control Algorithm To Minimize Torque Ripple and Acoustic Noise of Switched Reluctance Motors", PhD Thesis, Middle East Technical University, department of Electrical and Electronic Engineering, 2008.
- [13] Cook, R.D., Malkus, D., Plesha, M., "Concepts and Applications of Finite Element Analysis", USA, 1989.
- [14] John R Brauer, "Finite Element Analysis", MARCEL DEKKER, INC, 1988, pp.116.
- [15] Matthew N. O. Sadiku, "Numerical Techniques in Electromagnetics", 2<sup>nd</sup> ed., CRC Press LLC, 2001.
- [16] Ansys manual, "Electromagnetic Tutorial", 2<sup>nd</sup> ed., 1995.
- [17] Jianming Jin, "The Finite Element Method in Electromagnetics", The University of Michigan, A Wiley-Interscience Publication John Willey & Sons, Inc. 1993.
- [18] Flux manual, "Volume 2 : Mathematical Formulations", Cedrat 2000.
- [19] M.V.K. Chari and S.J. Salon, "Numerical Methods in Electromagnetism", Academic Press, 2000.
- [20] Mukherji, K.C., and NEVILLE, S., 'Magnetic Permeance of Identical Double Slotting', *ibid.* 1971, pp. 1257-1268.
- [21] Yilmaz Goynük, "Development of an Electrical Machines Analysis and Optimum Design Software Package", M.Sc Thesis, Middle East Technical University, department of Electrical and Electronic Engineering, 2008.
- [22] Müjdat Tohumcu, "Optimum Design of Switching Reluctance Motors", PhD Thesis, Middle East Technical University, department of Electrical and Electronic Engineering, 1985.